UNIVERSITÀ
DI SIENA
1240

DEPARTMENT OF INFORMATION ENGINEERING

AND MATHEMATICS

Doctor of Philosophy program in

INFORMATION ENGINEERING AND SCIENCE

Ion current and exhaust gas composition measurements for combustion monitoring

Supervisor:

Professor Valerio Vignoli

Candidate:

Lorenzo Parri

Cycle XXXIII

a.a. 2019/2020

LORENZO PARRI

Firmato il 13/05/2021

Table of Contents

1. Introduction

The efficiency of combustion processes is assuming nowadays a huge importance, since the energy production, many industrial processes, as well as building heating systems are still mainly based on the combustion of hydrocarbons. The performance of the combustion process depends on many factors and it is a crucial point for the reliability and the efficiency of a plant or a thermal machine that exploits combustion as a primary source of energy. Moreover, the constant increasing of carbon dioxide concentration in atmosphere makes more and more important reducing the emission of this gas as well as the other pollutant/toxic chemical compounds that are produced during combustion. An optimized combustion process allows reducing dramatically the production of chemical compounds like carbon monoxide or nitrogen oxides, and also to releasing in the atmosphere the minimum amount of carbon dioxide per unit of energy produced. There are many studies related to the optimization of the internal combustion of the engines (see e. g. [1] and the references therein), especially for automotive applications, whereas the literature is less exhaustive for burner combustion optimization.

The focus of this work is the study and the development of measurement systems allowing to get information about the combustion characteristics in gas turbines, with the aim of providing tools for monitoring/controlling the combustion parameters and keeping the combustion efficiency as high as possible over time. This activity has been developed in collaboration with Beker Huges (Nuovo Pignone Tecnologie - Florence), one of the world leaders in the design and development of gas turbines.

Two different sources of information on the state of the combustion process have been considered in this thesis, namely the density of ions produced by the flame in the combustion chamber and the composition of the exhaust gases.

The measurement of the ionic density due to the flame has been used since several years, particularly in the automotive sector, to obtain information about the combustion process [2] [3]: from the postprocessing of the signal obtained using ionization sensors (or ionic current sensors), it is

possible to determine, for example, the onset of the combustion, the air–fuel ratio (and therefore the pollutant concentration at the exhaust), as well as to get information about the flame stability and the occurrence of periodic pressure variations in the combustion chamber [4]. On this basis, even if the relationship between combustion parameters and flame induced ion density is highly dependent on the type of fuel, there is room to exploit the information of the ion sensors also with gas turbines, to optimize the operation of the combustor (e.g. reducing instability) and to monitor the polluting emissions.

Ion or ionization sensors, which are usually used to measure the ion density in a burning gas, are essentially conductive electrodes capable of generating signals for either the charge transferred to/from the ionized gas and/or the charge induced on the electrodes themselves. The challenging issue concerns the choice of the materials for the sensor (electrodes and electrical insulators) which, being placed in the combustion chamber, must operate in extreme conditions, i.e., for example, in presence of very high temperatures. On the other hand, the conditioning front-end electronics for this kind of sensors is not critical.

As far as the measurement of the concentration of toxic/pollutant compounds in exhaust gases is concerned, the most relevant compounds to be considered are carbon monoxide (CO) and nitrogen oxides (NOx). Monitoring CO and NOx in the exhaust gases is important not only from the point of view of environmental pollution, but also because their concentrations are useful and reliable indicators about the combustion efficiency. The drawback is that, due to the measurement procedure, they cannot be used for a timely feedback control of the combustion process, the reason is that the exhaust gases must be sampled from the chimney and pumped to the measurement instrument (gas analyser), and this procedure introduces a significant delay between the instant in which the gases are produced by the combustion and the time at which they are analysed.

From the standpoint of the measurement instruments, exhaust gas analysers with different accuracies and costs (which are usually relevant) are available on the market. These devices can be portable or fixed and can exploit different measurement principles. Besides cost, an issue of these devices is that accurate gas sensors need frequent calibration exploiting reference gas tanks, which can be a problem in specific industrial plants such as power generation or oil and gas plants. The possibility to use a more flexible gas analyser, with a better trade-off among cost, measurement accuracy, the calibration intervals and robustness, is a deeply felt need in the oil & gas sector,

considering also that these instruments are required to operate in environments that can be severely harsh, especially in terms of temperature and humidity.

In this thesis, the development and testing, in laboratory and in actual test rigs, of two measurement instruments, one for ion current measurements and one for exhaust gas composition measurement is discussed. For the first instrument, a theoretical model of the ion sensor used was also developed, which significantly helped in interpreting the experimental data.

In detail, a brief discussion about the relationships linking the different parameters used in gas turbines combustion control, as well as about ion generation and measurement in combustion processes is presented in section 2. In the same section, a tool exploited to model the burner used for the experiments, which allowed to have a preliminary description of the relationships among the quantities of interest for the ion current measurements, is also presented. The developed model for the ion measurement probe is presented in section 3. In section 4 and 5, the experimental setup and the obtained measurements are discussed. In section 6 an overview of the possible exhaust gas measurement techniques is reported, whereas in section 7 the architecture of the designed instrument for exhaust gas analysis is presented. Finally, before the conclusions, in section 8 the tests on the field of the designed gas analyser are presented and discussed.

1.1 Contributions

A) T. Addabbo, A. Fort, M. Mugnaini, **L. Parri**, V. Vignoli, M. Allegorico, M. Ruggiero and S. Cioncolini, "Ion Sensor-Based Measurement Systems:Application to Combustion Monitoring in Gas Turbines," *IEEE Transactions on Instrumentation and Measurement,* vol. 69, no. 4, 2020.

B) Tommaso Addabbo, Ada Fort, Marco Mugnaini, **Lorenzo Parri**, Stefano Parrino, Alessandro Pozzebon, Valerio Vignoli, "A low power IoT architecture for the monitoring of chemical emissions." Published in: *Acta Imeko* 8.2 (2019): 53-61.

C) A. Pozzebon, A. Fort, E. Landi, M. Mugnaini, **L. Parri**, V. Vignoli. "A LoRaWAN Carbon Monoxide Measurement System with Low-Power Sensor-Triggering for the Monitoring of Domestic and Industrial Boilers., *IEEE Transactions on Instrumentation and Measurement*, Ref.: Ms. No. TIM-20-01622R2

D) Addabbo, T., Bardi, F., Cioncolini, S., Fort, A., Mugnaini, M., **Parri, L.**, Vignoli, V. "Multi-sensors exhaust gas emission monitoring system for industrial applications.", (2019) *Lecture Notes in Electrical Engineering*, 512, pp. 49-56.

E) T. Addabbo, A. Fort, M. Mugnaini, **L. Parri**, V. Vignoli, M. Allegorico, M. Ruggero, S. Cioncolini. "Ion sensors: application to combustion monitoring in gas turbines", 2019 *IEEE Sensors Applications Symposium (SAS)*, Sophia Antipolis, France, 2019, pp. 1-6. doi: 10.1109/SAS.2019.8706114

F) Addabbo, T., Fort, A., Mugniani, M., **Parri, L.**, Vignoli, V. "An unconventional type of measurement with chemoresistive gas sensors exploiting a versatile measurement system", (2017) Proceedings - 2017 *1st New Generation of CAS*, *NGCAS 2017*, art. no. 8052282, pp. 113-116.

G) Addabbo, T., Fort, A., Mugnaini, M., **Parri, L.**, Parrino, S., Pozzebon, A., Vignoli, V., "An IoT Framework for the Pervasive Monitoring of Chemical Emissions in Industrial Plants.", (2018) 2018 *Workshop on Metrology for Industry 4.0 and IoT, MetroInd 4.0 and IoT 2018* - Proceedings, art. no. 8428325, pp. 269-273.

H) T. Addabbo, A. Fort, M. Mugnaini, **L. Parri**, A. Pozzebon, V.Vignoli., "Smart Sensing in Mobility: a LoRaWAN Architecture for Pervasive Environmental Monitoring.", 2019 IEEE 5th *International forum on Research and Technology for Society and Industry* (RTSI), Florence, Italy, 2019, pp. 421-426, doi: 10.1109/RTSI.2019.8895563.

I) T. Addabbo, A. Fort, M. Intravaia, M. Mugnaini, **L. Parri**, A. Pozzebon, V. Vignoli., "Pervasive environmental monitoring by means of self-powered Particulate Matter LoRaWAN sensor Nodes.", *Imeko tc4 2020*, Palermo.

2. Combustion Control: the possible role of ion density measurements

Combustion control of gas turbines is a complex topic that is not dealt in this thesis. Just a few considerations are reported to introduce the framework in which the research activity was developed.

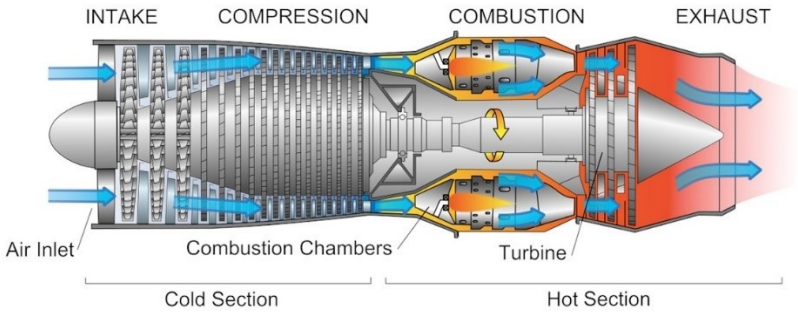

Figure 2.1 . A gas turbine structure

The combustion control strategy for a gas turbine is set up during the machine tuning procedure. Among all the quantities monitored, two are more directly linked to the combustion: the exhaust gases composition and the pressure pulsations in combustion chamber. Pulsation phenomena consist of rapid changes of pressure in combustion chamber caused by a not correct combustion of the fuel. These events must be avoided because they may be dangerous for the machine integrity.

The flame temperature is directly proportional to the output power and it is not directly measured, but is calculated knowing the fuel chemical composition, and the air flow.

Usually, an increase of flame temperature causes an increase of pressure pulsations and NOx concentration in the exhaust gases, and a decrease of flame temperature causes a decrease of NOx concentration as shown in Figure 2.2 [5]. The flame temperature depends on several factors but it is mainly determined by the lambda factor (λ), i.e. the ratio between the mass of air and the mass of fuel used to supply the burners divided by the stoichiometric air to fuel ratio. The ideal lambda factor ($\lambda = 1$) can be calculated knowing the chemical composition of the fuel: a lambda factor $<$

1 indicates that more fuel than required is supplied: in this condition the flame will be more stable but with a larger temperature, so the production of NOx compounds will increase. If the lambda factor is greater than one, more air than required is supplied, and the flame temperature and the production of NOx will decrease. The formation of CO is usually proportional to the presence of not completely combusted elements. In case of very low lambda factors the concentration of CO can dramatically increase whereas for larger lambda values the CO concentration gets lower because almost all the fuel is easily burned. Unfortunately, the CO concentration is very hard to be predicted, the formation causes of this gas during combustion are complex and, in some cases, not completely known. This is the main reason for which it is still very important to measure CO concentration. Operating at high lambda values is a good choice in terms of efficiency and emission of toxic compounds, but the flame becomes less stable and the control of the combustion becomes harder.

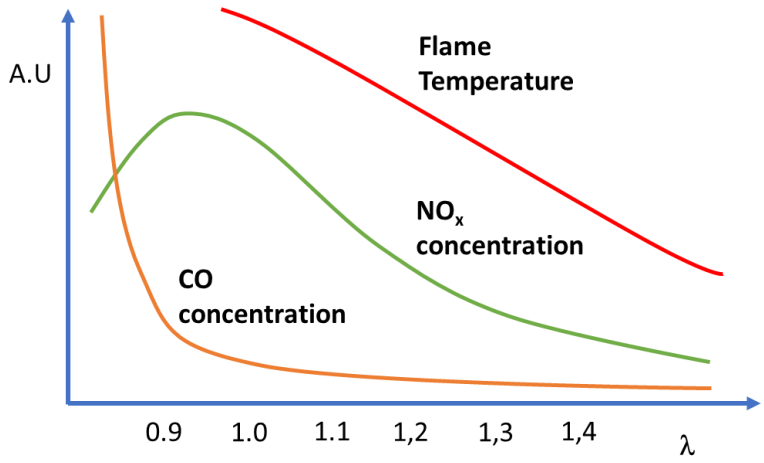

Figure 2.2 – Qualitative plot of flame temperature, CO and NOx emission concentrations as a function of lambda factor. (A.U.: arbitrary units)

From this brief introduction it can be easily understood how much an efficient control of the combustion is important for a gas turbine burner. Nowadays, the demand on the market of low emission machines is increasing, and the combustion control is becoming an even more critical aspect.

The ion current measurement is a promising technique to easily control the conditions of the combustion, and a cheap versatile and portable instrument to monitor the chemical composition of exhaust gases can be of great use and application in the oil and gas sector. An accurate condition monitoring of burners makes easier to program the preventive maintenance, and to keep the combustion process in optimal conditions over the time, reducing maintenance costs and emission of toxic compounds, while increasing the efficiency.

2.1 Ion Current Measurement: State of the art

Measurement of the ionic density in the burning gases have been used for several years, particularly, in the automotive sector, to obtain information about the combustion process [2], [3]. Although the relationship between combustion parameters and ionic density in the flame is strongly dependent on the type of fuel, it is documented in the literature that, from the postprocessing of the signal obtained using ionization sensors (or ionic current sensors), it is possible to determine, for example, the occurrence of pressure dynamics, the onset of combustion, the air–fuel ratio, and the flame stability [4]. Therefore, ion sensor information could be used to optimize the combustor operations (e.g., reducing the instabilities) and to monitor pollutants emission, which is of particular interest today.

Ion sensing is based on immersing one or two metal electrodes in the flame where exothermic chemical reactions release a large amount of ions (chemo-ionization) and sensing their concentration, either biasing the electrodes and measuring the current due to the drift of ions forced by the external applied electrical field, or by using unbiased electrodes and by measuring the charge induced in the electrodes by the ions/electrons freely moving in front of the electrodes themselves [6]. The signal thus obtained depends on the ion concentration in the flame and allows for monitoring many combustion process characteristics, among which pressure pulsations that affect the ion concentration locally, besides simply indicating the presence of the flame.

In general, many different monitoring applications through ion sensors have been proposed for combustors or combustion engines, mainly for endothermic alternative engines, more rarely for rotative ones [7] [8] [9] [10] [11] [12] [13] [14] [15] [16] [17]. The simplest successful application is

flame detection, but recently many studies propose systems with enhanced monitoring capability from crank angle in diesel engines to burning gas characteristics in gas turbines. In these studies, some efforts were devoted to understanding and modeling the sensor behavior, but actually a thorough model still lacks. On the other hand, the same sensor structure and sensing strategy is used, studied and modelled for plasma studies in different application fields (plasma based material processing and aerospace application) and it is called Langmuir probe.

2.2 Ion Current theoretical background

The combustion of hydrocarbons is accompanied by the generation of a large quantity of ions by a process called "chemoionization". The main reactions that allow for the formation of ions are listed in Table 1 [18] [19] [20]. In the table the parameters $\boldsymbol{A}$, $\boldsymbol{\upsilon}$ and $\boldsymbol{E_a}$ define the reaction rate constant $\boldsymbol{k}$ according to the Arrhenius equation (1), $\boldsymbol{R}$ is the universal perfect gas constant and $\boldsymbol{T}$ the absolute temperature, supposing to have second order reactions:

$$k = A\,T^{\upsilon}\,e^{\frac{-Ea}{RT}} \qquad (1)$$

Step	Reaction	A $\left[\frac{cm^3}{mol\ s}\ T^{-\upsilon}\right]$	υ	$E_a\left[\frac{kJ}{mol}\right]$
1	$CH + O \rightarrow CHO^+ + e^-$	$2.31 \cdot 10^{11}$	0.00	7.12
2	$CHO^+ + H_2O \rightarrow H_3O^+ + CO$	$1.00 \cdot 10^{16}$	−0.09	0.00
3	$CHO^+ + CH_2 \rightarrow {CH_3}^+ + CO$	$5.62 \cdot 10^{14}$	0.00	0.00
4	$C_2H_3O^+ + O \rightarrow CHO^+ + CH_2O$	$2.00 \cdot 10^{14}$	0.00	0.00
5	${CH_3}^+ + H_2O \rightarrow C_2H_3O^+ + CH_2$	$7.24 \cdot 10^{14}$	0.00	0.00
6	$C_2H_3O^+ + e^- \rightarrow CH_2CO + H$	$2.29 \cdot 10^{18}$	−0.50	0.00
7	$H_3O^+ + e^- \rightarrow H_2O + H$	$2.29 \cdot 10^{18}$	−0.50	0.00
8	$H_3O^+ + e^- \rightarrow OH + H + H$	$7.95 \cdot 10^{18}$	−1.37	0.00
9	$CHO^+ + e^- \rightarrow CO + H$	$7.40 \cdot 10^{18}$	−0.68	0.00

Table 1 - Main reactions responsible for the formation of ions in the combustion of hydrocarbons [18].

A general reaction scheme for the complete combustion of hydrocarbons is the following:

$$C_xH_y + \left(x + \frac{y}{4}\right) O_2 \rightarrow x\,CO_2 + \frac{y}{2}H_2O \quad (2)$$

The reaction can also be also incomplete, in this case ions species can be formed together with the formation of carbon monoxide:

$$C_xH_y + \left(\frac{x}{2} + \frac{y}{4}\right) O_2 \rightarrow x\,CO + \frac{y}{2}(H_3O^+ + e^-) \quad (3)$$

This situation can be due to a deficit of oxygen or can be an intermediate step of the complete reaction as shown in reaction (4):

$$x\,CO + \left(\frac{x}{2}\right) O_2 \rightarrow x\,CO_2 \quad (4)$$

Among all the possible reactions, the main source of ions comes from the first reaction shown in Table 1.

$$CH + O \xrightarrow{k1} CHO^+ + e^- \quad (5)$$

The CHO^+ species is not the dominant one in the flame because it rapidly reacts with water, that is widely present in exhaust gases, generating H_3O^+ ions as shown in the second reaction of Table 1.

$$CHO^+ + H_2O \xrightarrow{k2} CO + H_3O^+ \quad (6)$$

The reaction rate constant of step 2 in Table 1 (k_2) is much faster than the reaction constant of the step 1 (k_1), therefore the dominant species becomes H_3O^+. From Table 1 there are many other possible other ionic species involved in combustion processes but, according to literature [18], the

predominant species is H_3O^+. There is a limitation to ion density due to the recombination of H_3O^+ with free electrons [21] as shown in equation (7):

$$2H_3O^+ + 2e^- \xrightarrow{k4} 2H_2O + H_2 \qquad (7)$$

This reaction is very fast with respect to the ion formation but the probability of collision of electrons with H_3O^+ is very small [21]. The free electron density is also reduced due to the presence of electronegative species such as O^- or OH^-.

The reactions in a flame are not instantaneous and they take place in different areas. The probability of presence of different chemical species in different areas of the flame can be significantly different.

Considering the reactions (5) and (6), it is possible to write the concentration of ions $[CHO^+]$[1] at the equilibrium as a function of the reaction rates k_x and:

$$[CHO^+] = \frac{k_1[CH][O]}{k_2[H_2O]} \qquad (8)$$

Where:

$$k_1 = (2.31 * 10^{11})\, e^{\frac{-7.12}{RT}}\, \frac{cm^3}{mol\ s}$$

$$k_2 = (10^{16})\, T^{-0.09}\, \frac{cm^3}{mol\ s}$$

As described before, CHO^+ ions lifetime is relatively short so, by using equation (6) and (7), it is possible to write the concentration of $[H_3O^+]$ at the equilibrium as:

[1] The concentrations of chemical species are intended as a *Molar Concentration* [mol/cm^3]

$$[H_3O^+] = \frac{k_2[CHO^+][H_2O]}{k_4[e^-]} \quad (9)$$

Where:

$$k_4 = (2.29 * 10^{18})T^{-0.5} \frac{cm^3}{mol\ s}$$

If we consider a neutrality condition, the concentration of electrons and $[H_3O^+]$ can be considered the same. Using this consideration and combining equations (8) and (9) it is possible to obtain:

$$[H_3O^+] = \sqrt{\frac{k_1}{k_4}[CH][O]} \quad (10)$$

In a combustion process it is important to maintain the control of the Air-Fuel equivalence ratio that is has already seen is defined as the ratio between the air to fuel ratio of the combustible mixture and the stoichiometric air to fuel ratio [21].

$$\lambda = \frac{AFR}{AFR_{Stech}} \propto \frac{\frac{[O]}{[CH]}}{AFR_{Stech}} \quad (11)$$

Comparing equations (10) and (11) it is evident the correlation between $[H_3O^+]$ and λ [21] [22]; with a dependence witch is qualitatively shown in Figure 2.3.

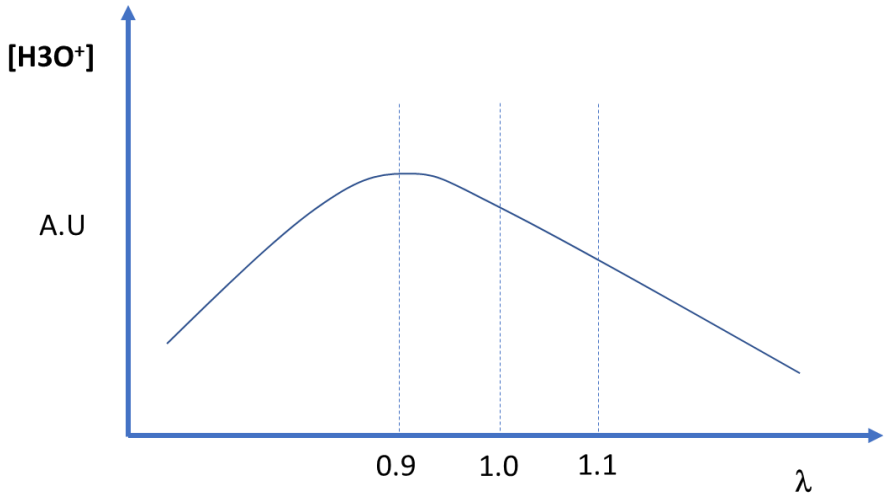

Figure 2.3 - Ion Concentration expected behaviour with lambda. (A.U.: arbitrary units). In general, as lambda increases, [CH] *decreases whereas more oxygen then required for the combustion is present, so* $[H_3O^+]$ *decreases. For low values of lambda, the oxygen is not sufficient for a complete combustion, causing a decreasing of* $[H_3O^+]$.

In the last equations we considered a dependence on monoatomic oxygen (O). The monoatomic oxygen is not present at environmental conditions, but this is not true inside the flame. As shown in Figure 2.4 at around 2000 Kelvin the diatomic oxygen can dissociate making possible the presence of monoatomic oxygen.

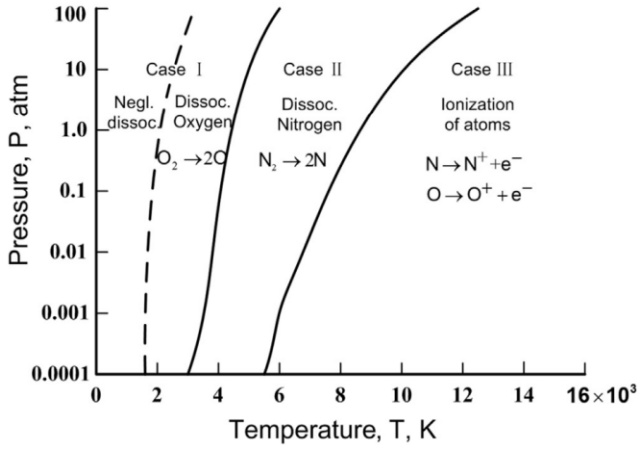

Figure 2.4 - Dissociation of composes in pressure and temperature domain [23].

2.3 Ion Channel

To measure the ion density, it is necessary to transform the presence of charge in the flame in an electrical signal. The classical solution is to apply an electric field across two electrodes and to measure the current flowing between them. This current is due to the ionic channel, between the electrodes, originated by the flame. As a first approximation the ion density is higher in high temperature regions [24].

The current is due both: 1) to charged species moving between the electrodes and 2) to the charge transferred from the gas to the electrodes. If a parallel planar electrodes structure is adopted, as in Figure 2.5, it is possible to give a simple description of the measured current assuming that no chemical reactions occur at the electrode interfaces.

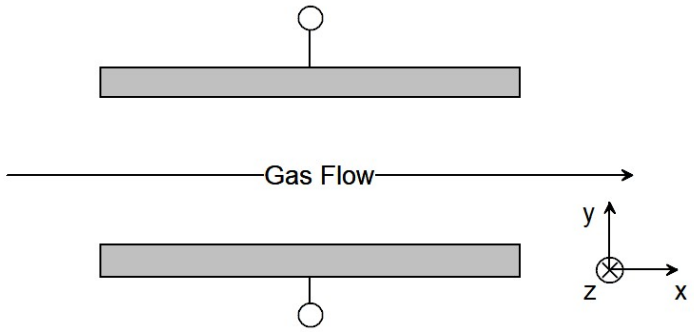

Figure 2.5 – Electrodes Geometry

In Figure 2.5 the planar plates are parallel to the xz-plane, we consider an ionized gas flow containing only H_3O^+ ions moving along the x-axis. Under these assumptions, the following equations can be considered [19] :

$$\frac{\partial p_i}{\partial t} + \frac{\partial \Gamma_{i,x}}{\partial x} + \frac{\partial \Gamma_{i,y}}{\partial x} = -\beta p_i n + k_{chem} \qquad (12)$$

$$\frac{\partial n}{\partial t} + \frac{\partial \Gamma_{e,x}}{\partial x} + \frac{\partial \Gamma_{e,y}}{\partial x} = -\beta p_i n + k_{chem} \quad (13)$$

$$\frac{\partial^2 \phi}{\partial x^2} + \frac{\partial^2 \phi}{\partial y^2} = -\frac{q}{\varepsilon}(p_i - n) \quad (14)$$

Where: $\boldsymbol{p_i}$ is the cations volume density, $\boldsymbol{n}$ is the electrons volume density, $\boldsymbol{\beta}$ is the electron-cations recombination factor, $\boldsymbol{K_{chem}}$ is the generation rate due to Chemo-Ionization, $\boldsymbol{\Gamma_{m,k}}$ is the flow along k of the species m, $\boldsymbol{\phi}$ is the external applied potential, $\boldsymbol{\varepsilon}$ is the medium dielectric constant, $\boldsymbol{q}$ is the electron charge.

Equations (12) and (13) represent the charge flow balance between the electrodes considering having moving ions. The equation (14) considers the application of an external electric potential $\boldsymbol{\phi}$. For K_{chem}, the generation rate of ions, we consider H_3O^+ ions according to the previous discussion, whereas β, the rate of recombination of cations with electrons, is the rate constant $k4$ in reaction (7). The variation with time of ions and electrons is the rate of generation K_{chem} minus the recombination rate and the charge species flow. The charge species flow is a composition of different effects. One is the mechanical transportation due to exhaust gas flow. In addition, there is a drift component due to the external electric field, and a diffusion component due to different ion concentrations, as described by the following equations:

$$\Gamma_{i,x} = -D_i \frac{\partial p_i}{\partial x} + \mu_p p_i E_x + p_i v_{flow}(y)$$
$$\Gamma_{i,y} = -D_i \frac{\partial p_i}{\partial y} + \mu_p p_i E_y \quad (15)$$

$$\Gamma_{e,x} = -D_e \frac{\partial n}{\partial x} + \mu_e n E_x + n v_{flow}(y) \quad (16)$$

$$\Gamma_{e,y} = -D_e \frac{\partial n}{\partial y} + \mu_e n E_y$$

Where: $\boldsymbol{\mu_x}$ is the mobility of species *x*, $\boldsymbol{E_k}$ is the electric filed along *k*, $\mathbf{D_x}$ is the diffusion coefficient of species *x*, $\boldsymbol{V_{flow}}$ is the gas flow speed.

In equations (15) and (16), D_x can be expressed by the Einstein relationship:

$$D_x = \mu_x \frac{KT}{q} \qquad (17)$$

2.3.1 Small External Electric Field Assumption

To simplify the model described by equations (12)(13)(14)(15)(16), some assumption can be considered:

- The chemical reactions are at the equilibrium so:

$$k_{chem} - \beta p_i n = 0 \qquad (18)$$

- The effect of the external electric field in removing electrons or ions from the area of measurement is negligible. This means that the gap between the electrodes can be considered occupied by a neutral plasma ($n = p_i$) and the electric field in reactions (15) and (16) coincides with the external field applied by the electrodes. This field can be considered constant, having only the *y* component different from zero (i.e., $E_x = 0$).
- $\boldsymbol{V_{flow}}$, that represents the transportation velocity of charges by the gas flow[2], is negligible with respect to the speed of charges accelerated by the electric field.

[2] The gas flow in a burner has usually a turbulent behaviour: in the proposed model $\boldsymbol{V_{flow}}$ is an average approximation of the actual transportation velocity.

Under these assumptions, the charges flow can be approximated by the following equations:

$$\Gamma_{i,x} = 0$$
$$\Gamma_{i,y} = \mu_p p_i E_y = \frac{J_i}{q} \quad (19)$$

$$\Gamma_{e,x} = 0$$
$$\Gamma_{e,y} = \mu_e n E_y = \frac{J_e}{q} \quad (20)$$

Where $\boldsymbol{J_x}$ is the density of current of species $\boldsymbol{x}$. The total current, considering a neutral plasma ($n = p_i$) is so given by:

$$J = J_i + J_e = q(\mu_e + \mu_p)\, n\, E_y \quad (21)$$

And we can express the equivalent conductivity of the ionized gas as:

$$\sigma = \frac{J}{E_y} = q(\mu_e + \mu_p)\, n \quad (22)$$

The density of charges ($n=p_i$) is determined using (18):

$$n = p_i = \sqrt{\frac{k_{chem}}{\beta}} \quad (23)$$

The ion channel has, under this assumption, a resistive behaviour since the current is linearly dependent on the applied electric field.

2.3.2 Strong External Electric Field Assumption (Saturation)

Another simplification of the model can be obtained in the limit case in which the external electric field $\boldsymbol{E_y}$ is strong enough that the drift velocity becomes much faster than the electron-ion pair generation rate. The flows in reactions (15) and (16) is mainly determined in this case by drift component along *y*. Charges are immediately attracted on the electrodes making impossible the recombination:

$$\frac{\partial n}{\partial t} = \frac{\partial p_i}{\partial t} = k_{chem} \qquad (24)$$

In this situation there is a saturation effect, all the ions pairs generated are attracted by the electrodes and the current becomes independent from the electric field:

$$J \propto q\, k_{chem} \qquad (25)$$

Since our target is to measure the ions density it is necessary avoiding to reach the saturation condition, which sets a saturation upper limit to the applied external electric field.

2.4 A Numerical Model for the Burner

The ion distribution density as a function of the lambda parameter can be estimated using a more complete physical model: for this purpose we used *Cantera,* an open-source suite of tools for problems involving chemical kinetics, thermodynamics, and transport processes [25]. In detail, we exploited the *one-dimension model flame* to simulate a burner premixed[3] flame: the flames are modelled in 1 dimension, by a set of ordinary differential equations (ODE), which is solved in the axial coordinate. The gas flow is physically bidimensional, but a similarity transformation allows to

[3] A premixed flame is a combustion reaction supplied by a homogeneous mixture of fuel and air that have been previously mixed.

consider a 1D problem. The burner is modelled by a stack of domains. The domains can be gas flows, inlets, outlets, surfaces, or others. Each domain is described by a set of variables and governing equations. The domains are spatially connected by boundary conditions. The solution of the problem is the solution of all the coupled domains. The domain stack used for this work is shown in Figure 2.6.

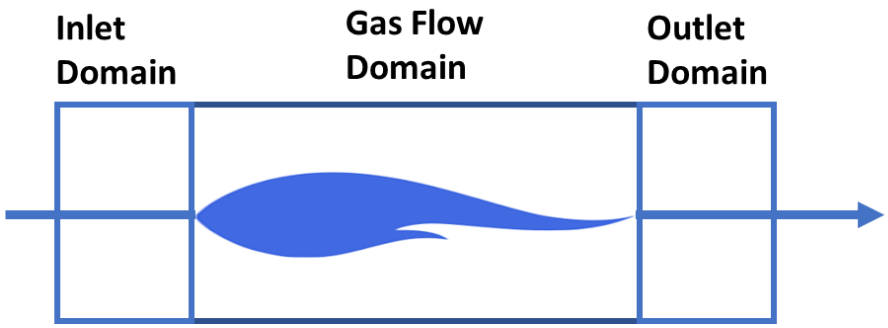

Figure 2.6 - Bruner Model

The inlet condition is a mixture of air and propane (C_3H_8). Considering the reaction (2) the stoichiometric ratio between fuel (propane) and Oxygen is 1:5. Considering that air contains 20.8% of oxygen the AFR_{Stech} in (11) is approximately 25. Simulations using different values of AFR, corresponding to values of λ factor from 0.7 to 1.3, were performed. The results in terms of $[H_3O^+]$ and flame temperature as a function of lambda are shown in Figure 2.7 and Figure 2.8.

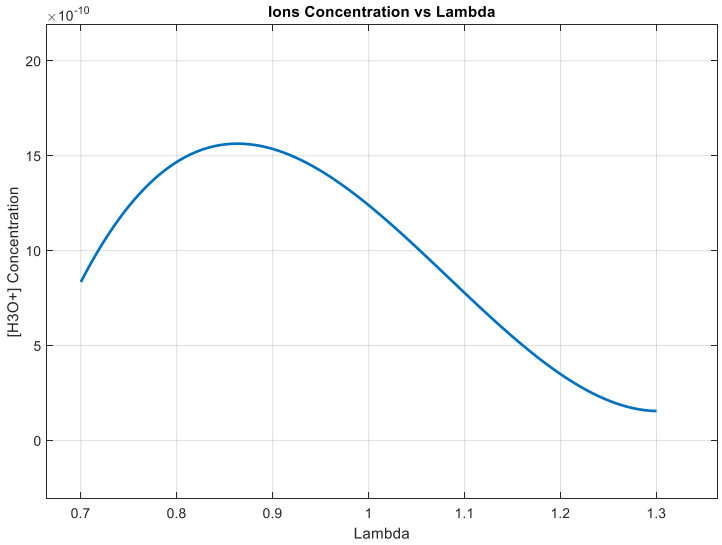

Figure 2.7 - Ion concentration vs lambda. The concentration is in mole fraction.

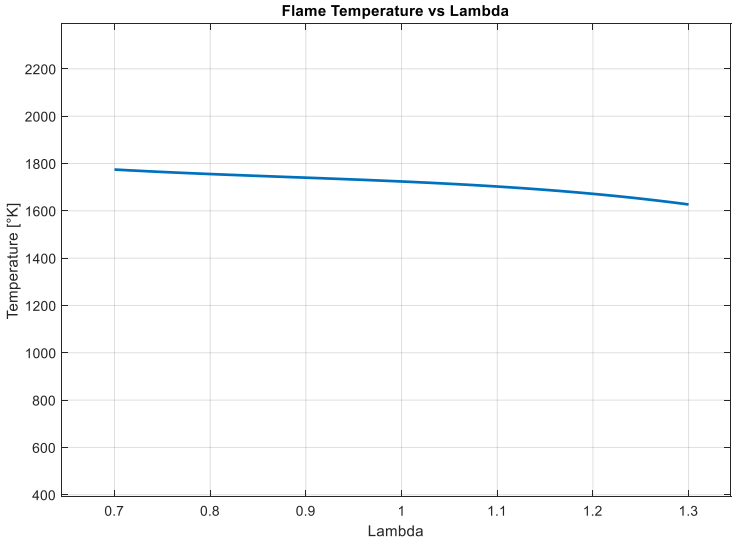

Figure 2.8 - Flame temperature vs lambda

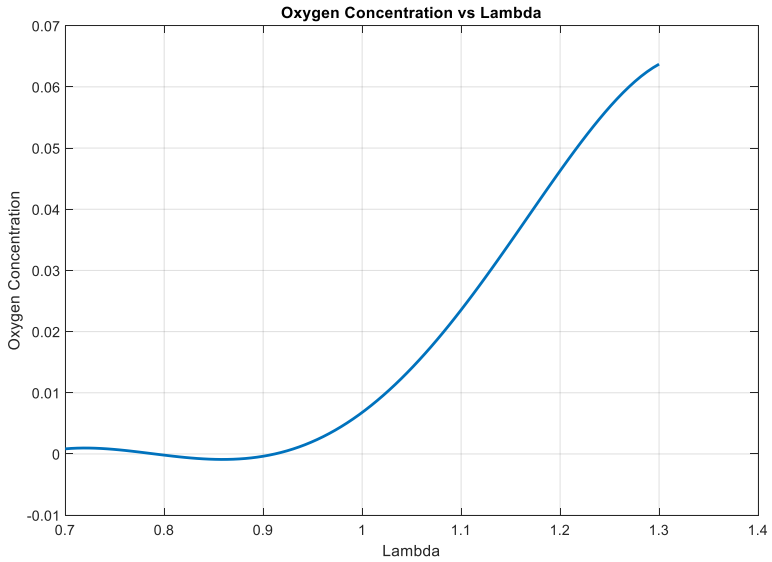

Figure 2.9 - Oxygen concentration in mole fraction vs lambda

The model considers only the premixed part of a burner and was useful to verify the expected behaviour of ion concentration with λ. The plots reported in Figure 2.7 and in Figure 2.3, have a similar behaviour. The flame temperature has been considered to check the dependence of ion concentration with local temperature. Higher temperature areas usually correspond to higher ion densities. If lambda increases, the temperature of the flame decreases and therefore also the ion density decreases. This effect was not considered in the theoretical discussion. Obviously, it is impossible to remove this dependence but when lambda is lower than 0.9 the ion density decreases even if the flame temperature does not decrease. This is due to the oxygen concentration, shown in Figure 2.9, that decreases dramatically for lambda ≤ 0.9. The results, even if obtained from a simplified model, confirm the theoretical analysis according to which the lack of oxygen causes a decrease of ion density.

3 Current Probe Model

In this thesis, based on the Langmuir probe theory, a complete model for the ion sensor is developed and compared with the simpler ion sensor models used in the literature, with reference to the gas turbine field, and considering to exploit as ion-sensor the electrode of the built-in spare spark-plug (even if this approach was already proposed in the literature [26] [27] and the reference therein), a complete modelling of the sensor and of the measuring system specifically aimed at understanding the measurement performance, still lacks). The model refines previous studies by taking into account also the physical effect of the gas/electrode interfaces. Note that chemical or electrochemical effects at this boundary are not accounted for in detail. The model accounts also for the loading effect of the front-end circuit and the overall dynamic behaviour.

The current probe used for ion current measurement in this work is a standard spark plug used to ignite the fuel/air mixture. This is a typical spark plug used for gas turbines or aircraft engines. The electrodes of the probe are shielded by a Pt/30%Rh coating. The spark plug electrodes experience temperatures which are typically between 600 °C and 800 °C. The probe, as shown in Figure 3.1, is asymmetric. One electrode (the smaller one) is in the inner part whereas the other one is in the external part and is usually in contact with the metallic case of the burner.

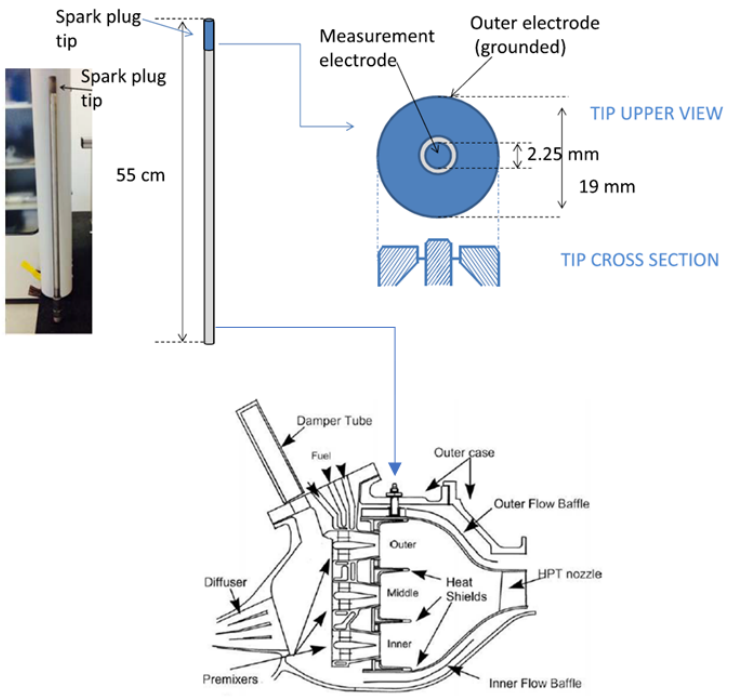

Figure 3.1 – The spark plug used for ion current measurement. Photograph of the used spark plug (up left). Tip upper view and cross section highlighting the electrode geometry (up-right). The area of the measuring electrode is approximately 4 mm^2.On the bottom the structure of a typical gas turbine burner that exploit this spark plug is shown.

A simplified equivalent circuit for the current probe sensor and the ion channel is shown in Figure 3.2. The resistance (R_{ion}) describes the gas conductance as discussed in (22). The capacitance (C) represents the double layer capacitances effect, mainly due to the ionic species at the electrode/gas interface. This capacitance can also have a large value.

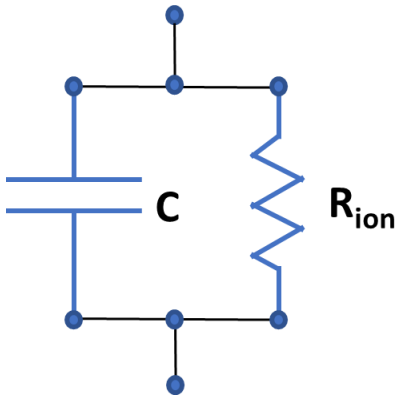

Figure 3.2 - Current probe simplified equivalent circuit.

Unfortunately, the simplified model of Figure 3.2 is effective to describe the measurement results only in specific circumstances, whereas in general a more complex model to describe the probe behaviour is necessary.

3.1 Ions probe physical background [23] [28]

To have an idea of the expected I-V characteristic of ions probes, we need to consider that the electrodes of the probe are close to the flame, where we can consider the presence of a plasma as shown in Figure 3.3. A plasma is an ionized gas that contains free charges (*electrons* and *positive ions or cations*) in which the total charge can be considered neutral. In this condition, being the electrodes of the probe made of conductive material, in the plasma, they can be considered a *Langmuir probe*. The Langmuir probe behaviour is based on the *Debye sheath* effect. If a metal is put in a plasma, on its external surface a layer of a greater density of positive charges is generated as shown in Figure 3.4. To explain this effect, we need to consider that electrons can be exchanged between metal and plasma, whereas cations cannot enter the metal. For simplicity we suppose that no chemical reactions occur at the metal-plasma interface. This last hypothesis can be considered almost true if a platinum coated probe is used as in our case. Chemical reactions at the interface, like oxidation reactions, can easily take place if a metal like iron is used for the external surface of the probe, making the ion current measurement impossible.

At the onset of the flame, the movement of electrons and cations can be modelled by a diffusion current if no external electric field is applied.

$$J_e = -e\, D_e \frac{d\rho_e(x)}{dx} \quad J_i = e\, D_i \frac{d\rho_i(x)}{dx} \tag{26}$$

Where $\boldsymbol{D_e}$ and $\boldsymbol{D_i}$ are the diffusion coefficients of electrons and cations, respectively, whereas $\boldsymbol{\rho_e(x)}$ and $\boldsymbol{\rho_i(x)}$ are the densities of electrons and cations. The diffusion coefficient of electrons is greater than the diffusion coefficient of cations. This results in a negative charge at the electrode site, that

at the end of a transient phase is balanced by a "*sheath*" of positive charges around the electrode (Figure 3.4), which generates a voltage drop at the electrode/plasma interface inhibiting the current (*diffusion current + drift current = 0*).

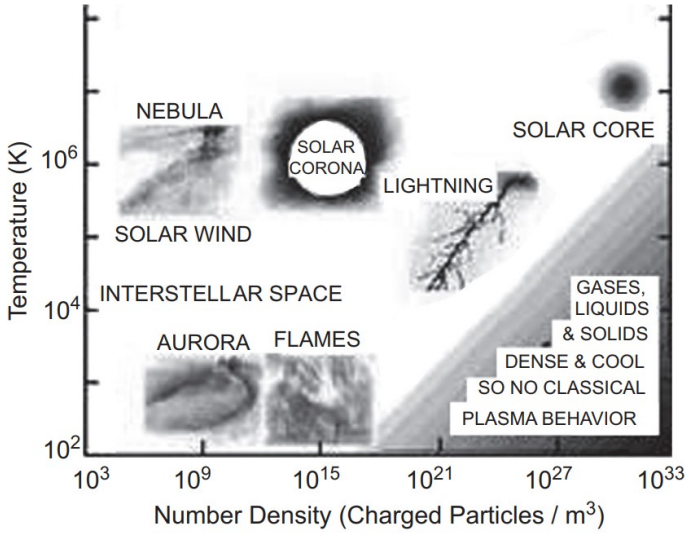

Figure 3.3 - Different plasma types as a function of charge density and temperature [23].

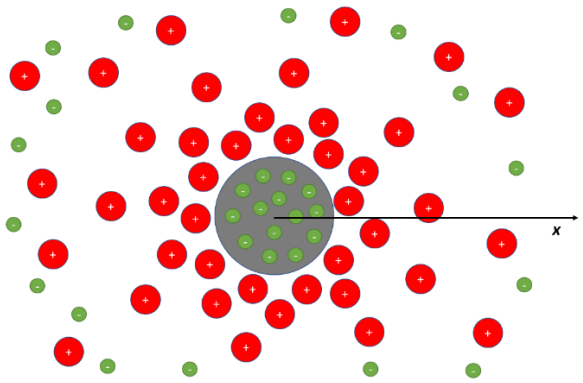

Figure 3.4 - Debye sheath: a sphere of conductive material is put inside a plasma.

To understand the behaviour of a Langmuir probe we need to consider some aspects of the plasma physics. For simplicity we will study a mono dimensional case in which the x coordinate is along the direction orthogonal to the probe surface that is set at $x=0$ (wall), as shown in Figure 3.5.

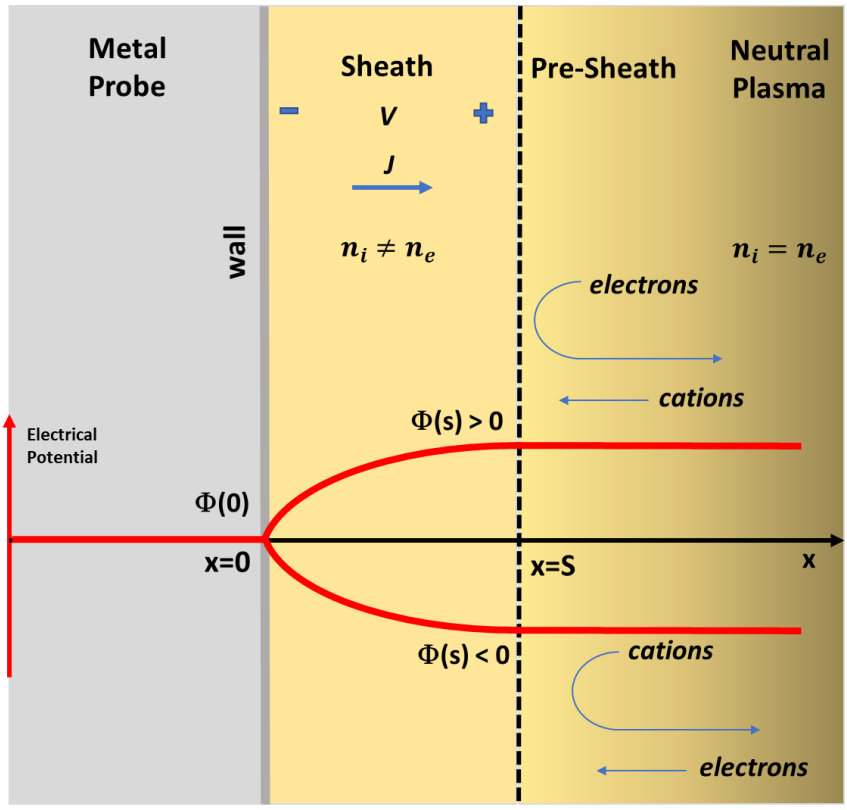

Figure 3.5 - Langmuir probe with shown two possible polarizations of the wall with respect to the plasma.

For this study, a *collision less Maxwellian plasma* is considered in which positive ions or cations (***i***) and electrons (***n***) are present with the same electrical charge ***e***. Let be m_i the mass of the positive ions, m_e the mass of the electrons, n_i the density per unit of length of ions, n_e the density per unit of length of electrons. V_i is the speed of ions while V_e represents the speed of electrons and, finally, $\Phi(x)$ is the electric potential at x. Let also be the *electron temperature* and the *cation temperature* T_e and T_i respectively, which are related to the average kinetic energy of electrons and ions. These temperatures are defined as the variation of the internal energy (U), given a volume containing a given number of particles, with respect to the particles entropy (S).

$$T = \frac{\partial U(S)}{\partial S} \qquad (27)$$

T_e and T_i multiplied by the *Boltzmann constant* (k_B)[4], are usually expressed in electron-volt (*eV*).

From now on we consider the electron/ion temperature in K.

In what follows an analytical expression for the current flowing in the sheath as a function of the voltage between probe and plasma is derived. The total current is the sum of the cations and the electron current contributions. We need to consider both the cases in which the potential of the probe, due to an externally applied voltage, is positive or negative[5] with respect to the plasma potential. The sheath edge is defined at $x=S$ but, obviously, this is an approximation because there is not a steep discontinuity between plasma and sheath. We consider, as a first approximation, that the plasma potential is equal to the potential ($\Phi(S)$) in $x=S$.

3.1.1 Electron current

Let us start with the component of the current given by electrons. We consider first a potential such that $\Phi(S) - \Phi(0) > 0$ (positive potential):

The electrons at $x=S$ are rejected by the potential inside the sheath region. Only electrons with a sufficient kinetic energy can enter in the sheath region. The energy conservation for these particles is:

$$\frac{1}{2} m_e {V_e}^2(S) - \frac{1}{2} m_e {V_e}^2(0) = e|\Phi(S) - \Phi(0)| \qquad (28)$$

[4] 1 eV corresponds to a temperature 11.605 Kelvin.

[5] Positive or Negative polarization is referred to the Figure 3.5 that is used as a reference. We considered a positive polarization the condition in which the plasma potential is greater than the probe potential.

So, the minimum kinetic energy required for the electrons at x=S to enter in the sheath region is:

$$\frac{1}{2} m_e {V_e}^2(S) > e|(\Phi(S) - \Phi(0)| \qquad (29)$$

The minimum speed is therefore given by:

$${V_{em}}^2(S) = \frac{2|\Phi(S) - \Phi(0)|}{m_e} \qquad (30)$$

The plasma is neutral ($n_i = n_e = n_p$), but in the sheath region this is not true $(n_i \neq n_e)$. To maintain the continuity of the electron charge species flow it is necessary to have that:

$$\begin{gathered} J_e = e\, n_e(0)|V_e(0)| = e\, n_e(S)\left|\overline{V_e(S)}\right| = e\, n_e(x)|V_e(x)| \\ n_e(S) \simeq n_p \\ x \in [0, S] \end{gathered} \qquad (31)$$

Where $\boldsymbol{J_e}$ is the electron current density, the electron density at the edge of the sheath can be considered equal to the plasma density.

The electron speed at the sheath edge can be found considering a *Maxwellian distribution*. The speed probability density function for a mono dimensional (x) *Maxwell-Boltzmann* distribution is:

$$f_{ve}(v_{ex}) = \sqrt{\frac{m_e}{2\pi k_B T_e}}\, e^{\frac{-m_e {v_{ex}}^2}{2k_B T_e}} \qquad (32)$$

The average speed of electrons at x=S, $\left|\overline{V_e^+(S)}\right|$, can be found considering the probability density function in (32) and velocities greater than V_{em}(S):

$$\left|\overline{V_e^+(S)}\right| = E[v_{ex}] = \int_{|V_{em}(S)|}^{+inf} \sqrt{\frac{m_e}{2\pi k_B T_e}}\, e^{\frac{-m_e v_{ex}^2}{2k_B T_e}}\; v_x\; dv_x$$

$$\left|\overline{V_e^+(S)}\right| = \sqrt{\frac{k_B T_e}{2\pi m_e}}\, e^{\frac{-e\,|\Phi(S)-\Phi(0)|}{k_B T_e}} \qquad (33)$$

So, using the equation (31), the current density when a positive potential is present, J_e^+, is given by:

$$J_e^+ = e\sqrt{\frac{k_B T_e}{2\pi m_e}}\, n_e(S)\, e^{\frac{-e\,|\Phi(S)-\Phi(0)|}{k_B T_e}} \qquad (34)$$

Let us now suppose to apply an external potential such that $\Phi(S) - \Phi(0) < 0$ (negative potential).

In this case, electrons are attracted into the sheath. Considering again a Maxwellian distribution for the electrons we can write that the average electron speed is[6]:

$$\left|\overline{V_e^-(S)}\right| = E[v_{ex}] = \int_0^{inf} \sqrt{\frac{m_e}{2\pi k_B T_e}}\, e^{\frac{-m_e v_{ex}^2}{2k_B T_e}}\; v_x\; dv_x = \sqrt{\frac{k_B T_e}{2\pi m_e}} \qquad (35)$$

The negative potential attracts electrons into the sheath: supposing that electrons move at X=S at $\overline{V_e^-(S)}$, the speed at *x=0* due to the potential acceleration of the electrons can be derived from equation (28):

$$\left|\overline{V_e^-(0)}\right|^2 = \frac{2e|\Phi(S)-\Phi(0)|}{m_e} + \left|\overline{V_e^-(S)}\right|^2 \qquad (36)$$

[6] This result does not take into account the effect of the presheath region and the Bohm's inequality.

Supposing constant, as a first approximation (small values of $\Phi(S) - \Phi(0)$), the electron's density in the sheath in case of negative polarization [29], the current density, J_e^-, can be expressed as:

$$J_e^- = e\, n_p |V_e^-(0)| = e\, n_p \sqrt{\frac{k_B T_e}{2\pi m_e} + \left|\frac{2e\big(\Phi(S) - \Phi(0)\big)}{m_e}\right|} \qquad (37)$$

3.1.2 Ion current

When a positive potential ($\Phi(S) - \Phi(0) > 0$) is considered, the cations at the edge of the sheath are attracted to the wall since the wall is negatively biased with respect to the plasma. We can write the same energy conservation equation as electrons:

$$\frac{1}{2} m_i V_i(S)^2 - \frac{1}{2} m_i V_i(0)^2 = -e|\Phi(S) - \Phi(0)| \qquad (38)$$

The speed of cations at the sheath interface can be obtained as for electrons exploiting the *Maxwell-Boltzmann distribution*. The speed probability density function of a monodirectional *Maxwell-Boltzmann* distribution (x), is for cations:

$$f_{vi}(v_{ix}) = \sqrt{\frac{m_i}{2\pi k_B T_i}}\, e^{\frac{-m_i {v_{ix}}^2}{2k_B T_i}} \qquad (39)$$

The average speed of cations, analogously to what seen for the electrons, is given by[7]:

$$\left|\overline{V_i^+(S)}\right| = E[v_{ix}] = \int_0^{inf} \sqrt{\frac{m_i}{2\pi k_B T_i}}\, e^{\frac{-m_i {v_{ix}}^2}{2k_B T_i}}\, v_x\, dv_x = \sqrt{\frac{k_B T_i}{2\pi m_i}} \qquad (40)$$

[7] This result does not take into account the effect of the presheath region and the Bohm's inequality.

The effect of $\Phi(S) > \Phi(0)$ is that the ion's velocity at the electrode edge is not only due to the average Maxwell Boltzmann speed but also to the potential itself that accelerates ions significantly. From the equation (38) we can derive the ion speed considering that the potential accelerates them from $\left|\overline{V_i^+(S)}\right|$ so:

$$|V_i^+(0)|^2 = \frac{2e|\Phi(S) - \Phi(0)|}{m_i} + \left|\overline{V_i^+(S)}\right|^2 \qquad (41)$$

Supposing the ions density constant in the sheath [29] and exploiting the (41) we can write:

$$J_i^+ = -e\, n_p\, |V_i(0)| = -e\, n_p \sqrt{\frac{k_B T_i}{2\pi m_i} + \left|\frac{2e(\Phi(S) - \Phi(0))}{m_i}\right|} \qquad (42)$$

When a negative potential ($\Phi(S) - \Phi(0) < 0$) is considered, the ions are repelled by the sheath. To calculate the ion current density the solution is the same used for electrons. Only cations with a sufficient kinetic energy can enter the sheath so we obtain:

$$J_i^- = -e\, n_p \sqrt{\frac{k_B T_i}{2\pi m_i}}\; e^{\frac{-e\,|\Phi(S) - \Phi(0)|}{k_B T_i}} \qquad (43)$$

3.1.3 I-V Model

Finally, we can sum up the current densities of cations and electrons. For a positive polarization such that $\Phi(S) - \Phi(0) > 0$, we can sum up the ions and electrons current densities contributions [28] :

$$J_{tot}^{+} = e\sqrt{\frac{k_B T_e}{2\pi m_e}}\, n_p e^{\frac{-e\,|\Phi(S)-\Phi(0)|}{k_B T_e}} - e\, n_p \sqrt{\frac{k_B T_i}{2\pi m_i} + \left|\frac{2e(\Phi(S)-\Phi(0))}{m_i}\right|} \qquad (44)$$

Instead, for a negative polarization such that $\Phi(S) - \Phi(0) < 0$, we have that:

$$J_{tot}^{-} = -e\sqrt{\frac{k_B T_i}{2\pi m_i}}\, n_p\, e^{\frac{-e\,|\Phi(S)-\Phi(0)|}{k_B T_i}} + e\, n_p \sqrt{\frac{k_B T_e}{2\pi m_e} + \left|\frac{2e(\Phi(S)-\Phi(0)}{m_e}\right|} \qquad (45)$$

To write a current-voltage relationship we define the potential $\boldsymbol{V = \Phi(S) - \Phi(0)}$, whereas the current is given by ***I=JA***, where ***A*** is the area of the probe. The current of the probe, for the two polarization cases, is given by:

$$I^{-}(V) = -e\,A\,n_p\sqrt{\frac{k_B T_e}{2\pi m_e}}\; e^{\frac{-e\,|V|}{k_B T_e}} + e\,A\,n_p\sqrt{\frac{k_B T_i}{2\pi m_i} + \left|\frac{2eV}{m_i}\right|}\;, V < 0 \qquad (46)$$

$$I^{+}(V) = +e\,A\,n_p\sqrt{\frac{k_B T_i}{2\pi m_i}}\; e^{\frac{-e\,|V|}{k_B T_i}} - e\,A\,n_p\sqrt{\frac{k_B T_e}{2\pi m_e} + \left|\frac{2eV}{m_e}\right|}\;, V > 0 \qquad (47)$$

We can check that if the $V = 0$ the current density for the two polarizations is continuous and equal to:

$$I^{+}(0) = I^{-}(0) = e\,A\,n_p\left[\sqrt{\frac{k_B T_i}{2\pi m_i}} - \sqrt{\frac{k_B T_e}{2\pi m_e}}\right] \qquad (48)$$

Whereas for $V \Rightarrow \pm\infty$ we have that the current is determined by:

$$I^{-}(-\infty) \cong e\,An_p\sqrt{\left|\frac{2eV}{m_i}\right|}\,, \qquad I^{+}(\infty) \cong -e\,An_p\sqrt{\left|\frac{2eV}{m_e}\right|} \tag{49}$$

In Figure 3.6 it is shown the plot of the equations (46) and (47) considering:

$A = 10^{-6}$ *Area of the probe in* m^2

$n_p = 10^{14}$ *Plasma density in number of particles/*m^3

$e = 1.6*10^{-19}$ *Electron charge in Coulomb*

$k_B = 1.38*10^{-23}$ *Boltzmann constant in J/K*

$m_i = 3.15*10^{-26}$ *Mass of* $H3O^+$ *cations in kg*

$m_e = 9.1*10^{-31}$ *Mass of electrons in kg*

$T_e = 1000 = T_i$ *Electron temperature in K*

The curve in Figure 3.6 represents $-I^{-}(V)$ for V<0 and $-I^{+}(V)$ for V>0.

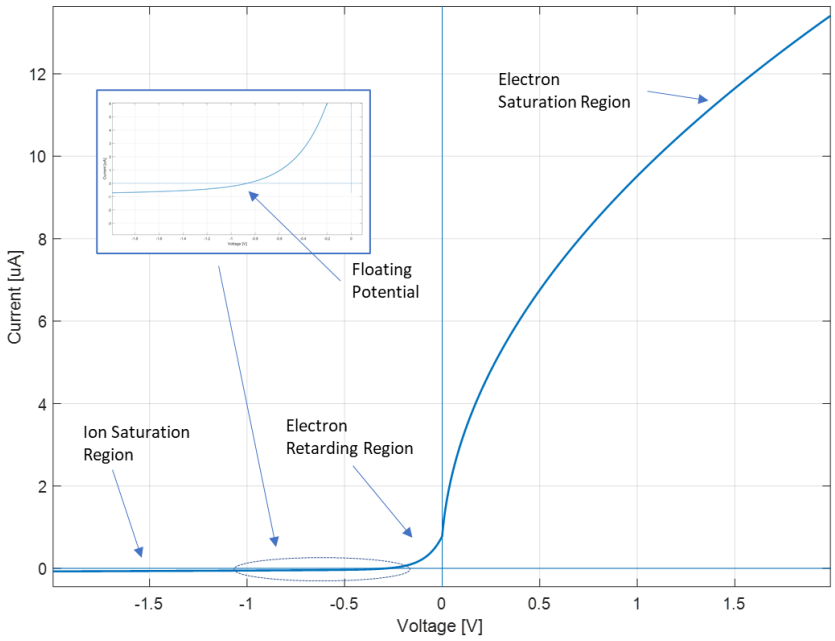

Figure 3.6 - I-V Plot of the model for the Langmuir probe. The strong asymmetry of the curve for values V>0 and V<0 is due to the strongly difference between the masses of electrons and ions.

3.1.4 Debye length

There is another aspect to be discussed when we talk about a plasma. Let us derive the density of electrons and cations as a function of x. Let us assume that $\Phi(S) - \Phi(0) > 0$.

For Ions, for small applied external potentials, we assumed a constant speed as shown in (40) so we can assume a constant density (n_p) in the sheath.

For electrons, we can find as a function of *x,* the mean velocity in the sheath from (33). Applying the continuity condition described in (31) we obtain:

$$n_e(x) = n_p e^{\frac{-e\,(\Phi(S)-\Phi(x))}{k_B T_e}} \qquad (50)$$

Exploiting the Poisson equation and defining $\varphi(x) = \Phi(S) - \Phi(x) > 0\,, x \in [0, S]$, it is possible to write:

$$\epsilon_0 \frac{d\varphi^2(x)}{dx^2} = e\,(n_e(x) - n_i(x)) \tag{51}$$

Using the equations (50) and (51) we get:

$$\epsilon_0 \frac{d\varphi(x)^2}{dx^2} = e\,n_p \left\{ e^{\frac{-\mathrm{e}\,(\varphi(x))}{k_B T_e}} - 1 \right\} \tag{52}$$

Assuming now that the argument of the exponential is smaller than one, the exponential can be replaced by the first order Taylor expansion:

$$\frac{d\varphi(x)^2}{dx^2} = e^2 n_p \frac{(\varphi(x))}{\epsilon_0 k_B T_e} \tag{53}$$

Let us now define the parameter λ_d as:

$$\lambda_d = \sqrt{\frac{\epsilon_0\, k_B T_e}{e^2\, n_p}} \tag{54}$$

We get:

$$\frac{d\varphi(x)^2}{dx^2} - \frac{\varphi(x)}{{\lambda_d}^2} = 0 \tag{55}$$

A general solution for this equation is:

$$\varphi(x) = c1\, e^{\frac{x}{\lambda_d}} + c2\, e^{-\frac{x}{\lambda_d}} \tag{56}$$

The equation can be solved imposing the boundary conditions, (we consider $\Phi(0) = 0$):

- $\varphi(0) = \Phi(S)$;
- $\varphi(S) = 0$

$$\varphi(x) = \frac{\Phi(S)\, e^{\left(-\frac{x}{\lambda_d}\right)} \left(e^{\left(\frac{2S}{\lambda_d}\right)} - e^{\left(\frac{2x}{\lambda_d}\right)} \right)}{\left(e^{\left(\frac{2S}{\lambda_d}\right)} - 1 \right)}$$

$$\Phi(x) = \Phi(S) \left[1 - \frac{e^{\left(-\frac{x}{\lambda_d}\right)} \left(e^{\left(\frac{2S}{\lambda_d}\right)} - e^{\left(\frac{2x}{\lambda_d}\right)} \right)}{\left(e^{\left(\frac{2S}{\lambda_d}\right)} - 1 \right)} \right] \qquad (57)$$

The plot of the equation (57), as a function of *x,* shown in Figure 3.7, represents the potential in the sheath region as $\Phi(x)$. The behaviour, as expected, is the same of the qualitative scheme in Figure 3.5.

The λ_d parameter is the so-called *Debye Length*. It is an important parameter for plasmas, and it gives us an indication of how the potential changes with the distance from the wall. For distances from the wall equal to λ_d, considering that $S >> \lambda_d$, the potential is attenuated by a factor $1/e$ with respect to $\Phi(S)$.

In practice, for distances from the wall smaller than the *Debye Length,* the neutrality, or better the quasi-neutrality, condition of the plasma is not true anymore. The potential exponentially changes with x and $n_e(x)$ gradually approaches n_p (as shown in equation (50)).

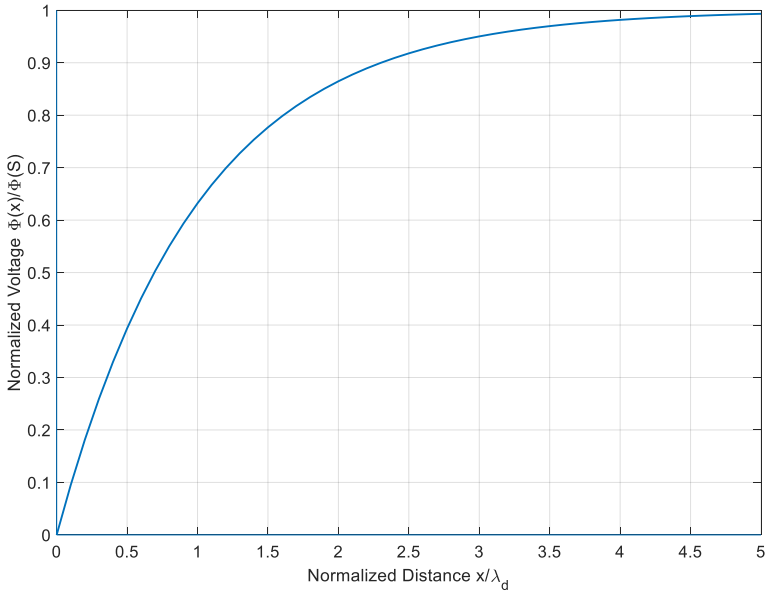

Figure 3.7 : Potential plot in the sheath region with $S>>\lambda_d$.

The *Debye Length* is useful to be compared with the dimensions of the probe used to measure the ion current. Only a probe with a distance between the electrodes much greater than the *Debye Length* can be modelled with the equations (46) and (47).

3.2 Ions probe equivalent circuit.

From the electrical point of view, the behaviour of the probe is very similar to a pn junction. The spark plug probe structure presented in Figure 3.1 is asymmetric because it is composed by two electrodes of different dimension (different area *A*). In Figure 3.8 it is proposed a model for the spark plug based on two Langmuir probes.

The junctions D1 and D2 represent the two Langmuir probes and are in series with the channel (neutral plasma) that has been considered resistive. The "n-type doped" part of the junction is the sheath side, whereas the "p-type doped" part is the metal side. The two capacitances C1 and C2 represent the parasitic effect of the interfaces. The formation of these two capacitances is due to

the Langmuir effect described before. When the plasma is generated there is an initial transient phase, during which these two capacitances, and the two junctions, are created by the diffusion of electrons and cations. During this transient phase, the proposed model is not valid.

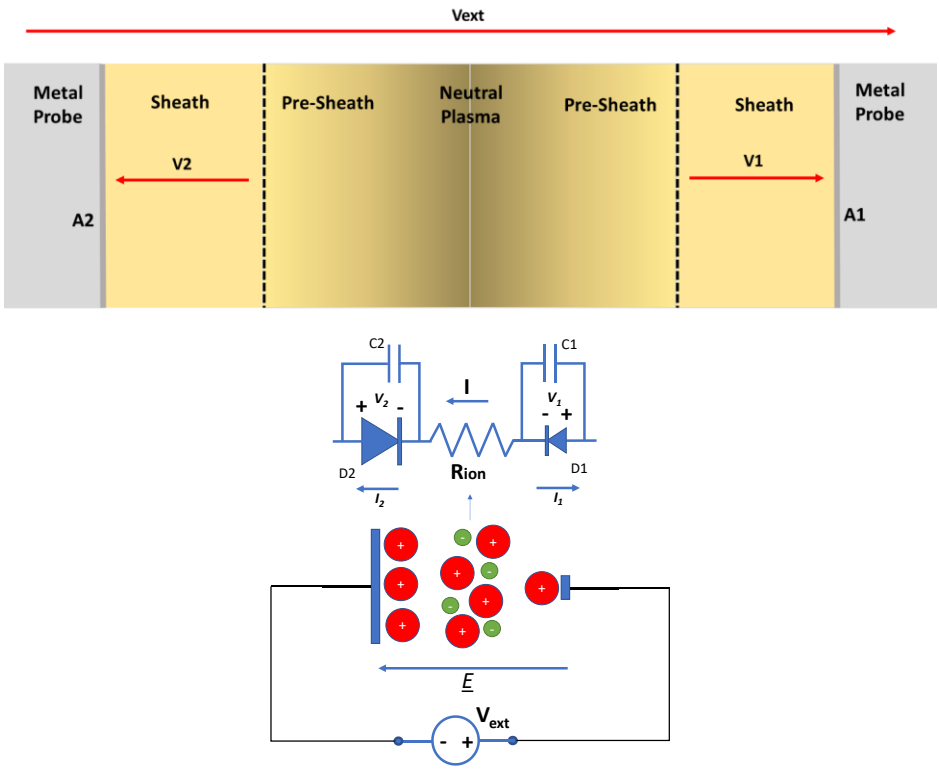

Figure 3.8 - Equivalent circuit of ionic channel and electrodes. The I-V relationship of D1 and D2 (that represents the two plasma- electrode junctions) are reported in equations (59).

The solution for the equivalent circuit in Figure 3.8 (without considering the capacitances effect) is:

$$V_{ext} = V_1(I) + R_{ion}I - V_2(I) \qquad (58)$$

where $V_1(I)$ and $V_2(I)$ that are the voltages across the junctions can be found inverting equations (46) and (47), whereas V_{ext} is the external applied voltage.

$$I_1(V_1 \geq 0) = A_1\,\alpha_p\left(\beta_p e^{-\gamma_p V_1} - \sqrt{\tau_p + 4\pi\gamma_p V_1}\right)$$
$$I_1(V_1 < 0) = A_1\,\alpha_n\left(-\beta_n e^{\gamma_n V_1} + \sqrt{\tau_n - 4\pi\gamma_n V_1}\right)$$

$$I_2(V_2 \geq 0) = A_2\,\alpha_p\left(\beta_p e^{-\gamma_p V_2} - \sqrt{\tau_p + 4\pi\gamma_p V_2}\right) \qquad (59)$$
$$I_2(V_2 < 0) = A_2\,\alpha_n\left(-\beta_n e^{\gamma_n V_2} + \sqrt{\tau_n - 4\pi\gamma_n V_2}\right)$$

$$I = I_2(V_2) = -I_1(V_1)$$

Where A_1 and A_2 are the area of the junction 1 and 2 respectively, and the quantities $\alpha_p, \alpha_n, \beta_p, \beta_n, \gamma_p, \gamma_n, \tau_p, \tau_n$ are given by:

$$\alpha_p = en_p\sqrt{\frac{k_B T_i}{2\pi m_e}}, \alpha_n = en_p\sqrt{\frac{k_B T_e}{2\pi m_i}}$$
$$\beta_p = \sqrt{\frac{m_e}{m_i}}, \beta_n = \sqrt{\frac{m_i}{m_e}}$$
$$\gamma_p = \frac{e}{k_B T_i}, \gamma_n = \frac{e}{k_B T_e} \qquad (60)$$
$$\tau_p = \sqrt{\frac{T_e}{T_i}}, \tau_n = \sqrt{\frac{T_i}{T_e}}$$

The channel equivalent resistance can be calculated according to equation (22). The equivalent conductance of the channel depends on the plasma ion density n_p. To calculate the resistance from the conductivity we consider the channel as a 'pipe' of length L_{ch} and average area A_{ch} in the plane orthogonal to the current direction.

$$R_{ion} = \frac{L_{ch}}{A_{ch}\,q(\mu_e + \mu_p)\,n_p} \qquad (61)$$

The plot of equation (58), using different plasma ion density (n_p) is shown in Figure 3.9. The parameters used are the same of Figure 3.6 except for the length of the channel, the area of the junctions and the cross-section of the conductive channel (A_{ch}):

$A_1 = 10^{-5}$ *Area of the D1 junction in* m^2

$A_2 = 10^{-3}$ *Area of the D2 junction in* m^2

$A_{ch} = 10^{-5}$ *Area of the ion channel in* m^2

$L_{ch} = 2*10^{-3}$ *Length of the ion channel in* m

$\mu_e = 100, (\mu_e > \mu_p)$ *Electron's mobility in plasma in* $m^2/(V\,s)$.

In Figure 3.10, it is evident that the different area of the two junctions creates a rectification effect on the applied voltage. In Figure 3.9 is shown a plot, in the same condition of the previous one, but simulating different plasma temperatures (*Ti=Te*). The temperature variation of ions does not significantly affect the saturation regions of the probe.

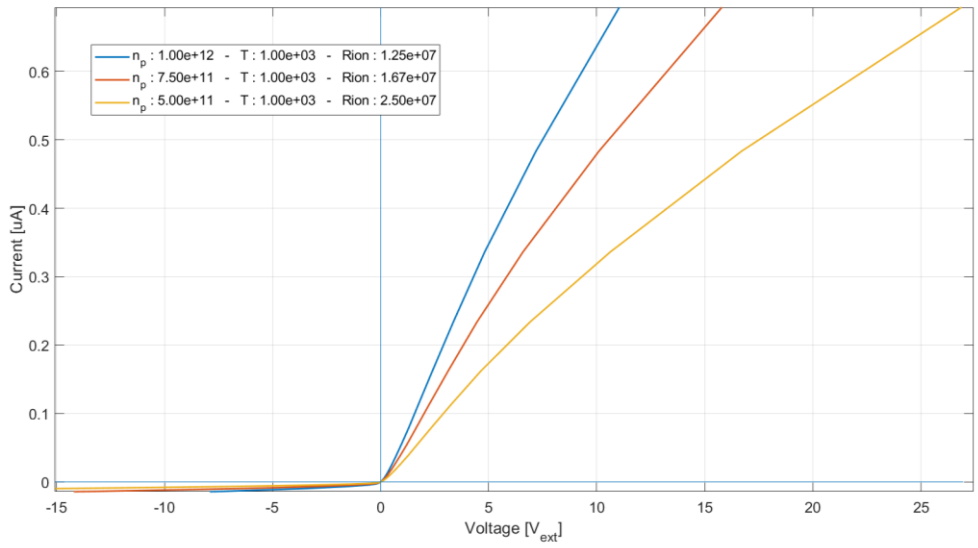

Figure 3.9 - I-V Plot for the circuit in Figure 3.8. In this simulation $A_1 = 10^{-5}$ m^2, $A_2 = 10^{-3}$ m^2, $A_{ch} = 10^{-5}$ m^2, $L_{ch} = 2*10^{-3}$ m, the other parameters are the same used in Figure 3.6. The different curves correspond to different plasma ion densities at the same temperature $T=T_i=T_e$.

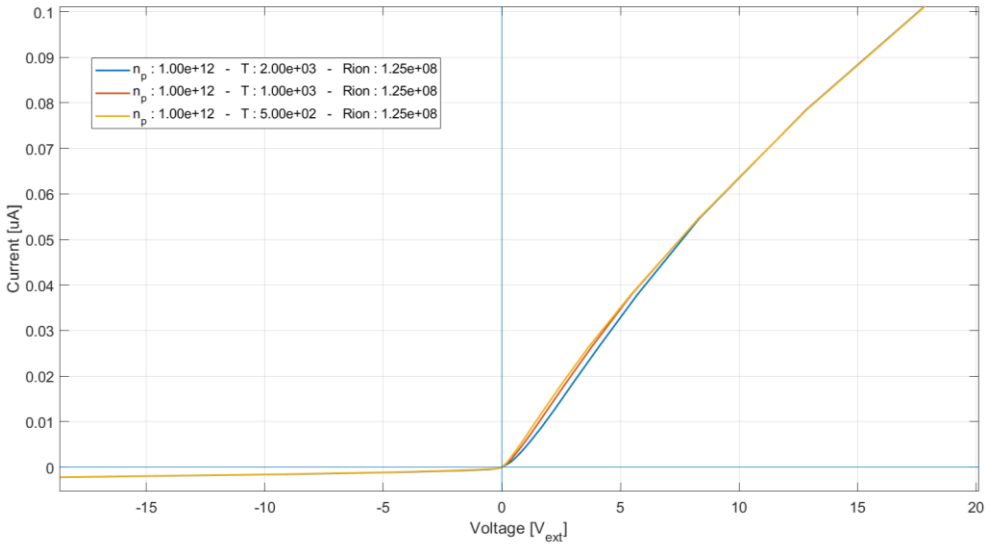

Figure 3.10 - I-V Plot for the circuit in Figure 3.8. In this simulation $A_1 = 10^{-5}$ m^2, $A_2 = 10^{-3}$ m^2, $A_{ch} = 10^{-5}$ m^2, $L_{ch} = 2*10^{-3}$ m, the other parameters are the same used in Figure 3.6. The different curves correspond to different plasma temperatures.

4 Ion Current Measurement Setup

A burner test bench was used to verify the model previously presented, and to evaluate the flame ion current in different combustion conditions. The combustible mixture with defined air to fuel ratios is obtained exploiting two controlled flows of air and propane (C_3H_8); ϕ_{Air} and ϕ_{Gas}, respectively. The mixture flow passes through a nozzle that impresses a rotation to the fluid to increase the flame stability (Figure 4.1). The combustion occurs after this nozzle, and the distance between the nozzle and the current probe (*d*) can be modified. To keep under control the temperature and avoid the overheating of the mechanical structure of the burner, a flow of cooling air around the burner is used. The probe is positioned before the mixing point of the cooling air to measure only the premixed contribution to the combustion. The exhaust gases produced by the combustion are tapped from the chimney, cooled, partially dehumidified and pumped to an exhaust gas analyser (this operation is usually referred to as 'exhaust gas sampling') to determine their composition in terms of Carbon Monoxide (CO), Nitric Oxides (NO_x) and Oxygen (O_2). This measure will be used to be correlated with the ion density measured by the current probe.

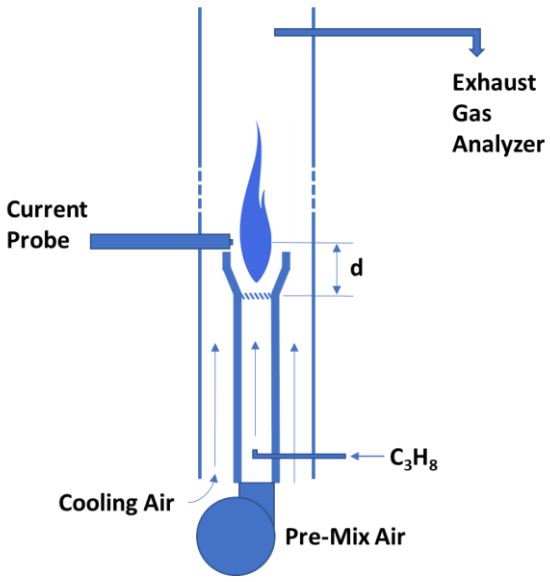

Figure 4.1 – Burner test bench structure.

As previously discussed, the quantity to be measured is the ion density in the gap between the two electrodes of the probe. From the electrical point of view, it is necessary to measure the current that flows in the probe through the ionic channel. This current, as discussed above, is due both to the ion channel characteristics and to the effect introduced by the Langmuir probe consisting of the two electrodes.

The characteristics of the signal to be measured, used for the design of the ion-current measurement instrument described hereafter, were obtained both from data reported in the literature and from preliminary tests on test burners, which made it possible to estimate both the dynamics and the frequency band of the expected signal in different operating conditions, and its statistical properties. These aspects are discussed in detail in the remainder of the paragraph.

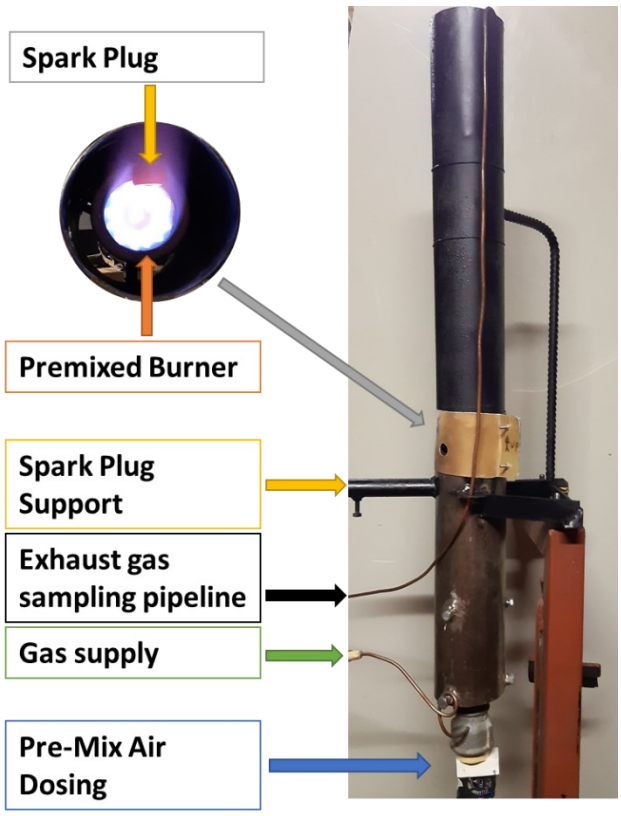

Figure 4.2 – A picture of the burner test bench.

Let us discuss about two possible measurement solutions that take advantage of a constant voltage (DC) or an alternate voltage (AC) excitation.

The instrument realized to measure the ion current generates the excitation signal and measures the current that flows through the electrodes. The structure of the instrument is shown in Figure 4.3, and two pictures of the instrument are shown in Figure 4.4 and Figure 4.5. The device is based on a microcontroller (STM32L432) embedding a 12-bit digital to analog converter (DAC), that is used to generate the waveform signals used to excite the current probe. The excitation signal can be a DC, a sinusoidal, a rectangular, or a triangular waveform. The signal shape, together with its amplitude and frequency, can be set by a serial interface and a Modbus® protocol. The signal generated by the DAC is amplified[8] up to a maximum of $\pm 19V$ and, by a shunt resistor, is applied to the current probe. The shunt resistor is used to measure the current due to the presence of the ion channel. The voltage across the resistor is amplified by a differential stage[9] and adapted to the microcontroller 12-bit ADC dynamics by an analog front end. The acquired signal is processed, and the root mean square value in the period of the excitation waveform is calculated and made available on the serial Modbus® present on the STM32L432 module.

[8] The amplifier is based on an OPA454 operational amplifier used to drive a class B amplifier stage based on TIP2955 and TIP3055 transistors.

[9] The differential amplifier has been realized using a standard instrumentation amplifier layout exploiting three OPA454 high voltage operational amplifiers.

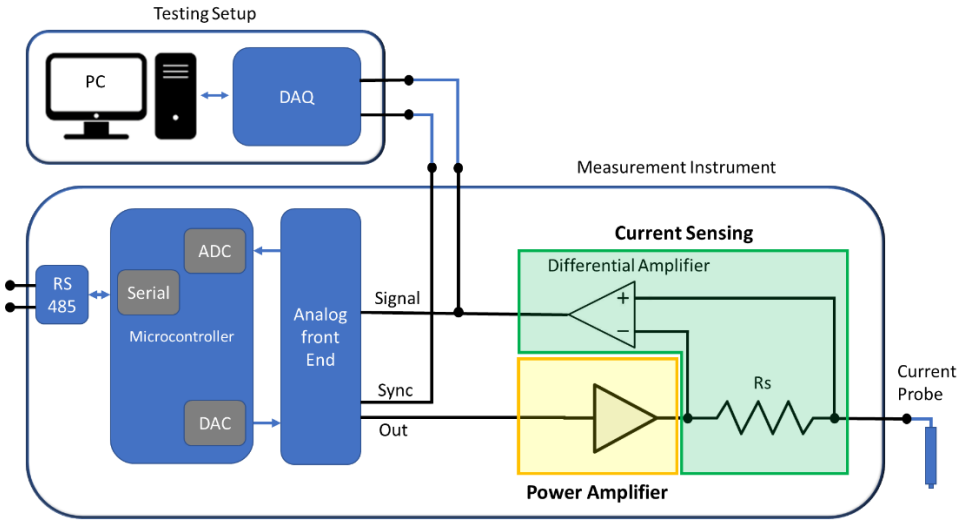

Figure 4.3 - Measurement instrumentation block diagram.

Figure 4.4 – A picture of the measurement instrument prototype.

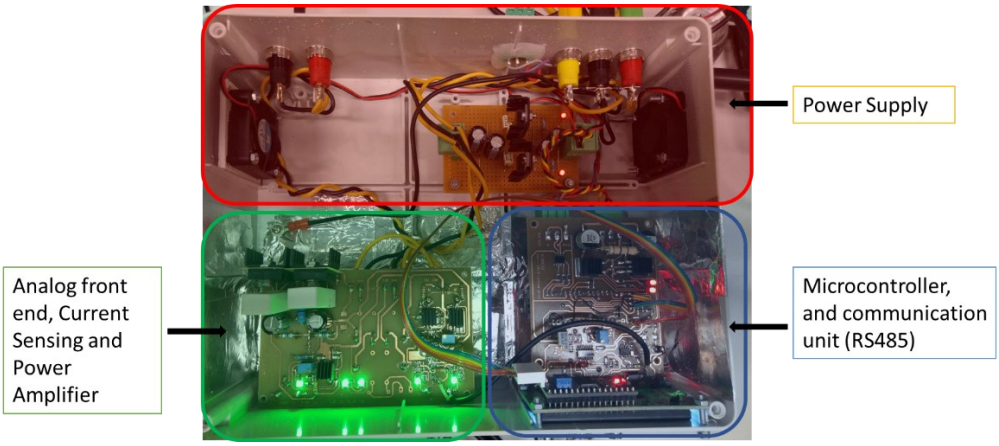

Figure 4.5 - A picture of the internal structure of the instrument prototype.

To debug the system, and to perform other more accurate measurements, the signal coming from the ion current probe can be also acquired using an external acquisition board, connected to a PC, which allows to perform more accurate and larger-bandwidth signal acquisitions.

The external acquisition board (NI-DAQ-6251) was used to sample the large bandwidth signal using a sampling frequency up to 1.25 MS/s. Using this setup, a preliminary analysis on the ion current signal has been performed to verify the expected signal bandwidth. From this analysis, the ion current signal is expected [30] to be limited in the bandwidth from 0 to 1kHz. The microcontroller ADC sampling frequency and the anti-aliasing filter in the analog front end have been designed to correctly acquire this signal bandwidth.

The probe electrical connection setup is shown in Figure 4.6: the inner part of the spark plug, that is the electrode with the smaller area, is connected to the positive side of the excitation voltage generator.

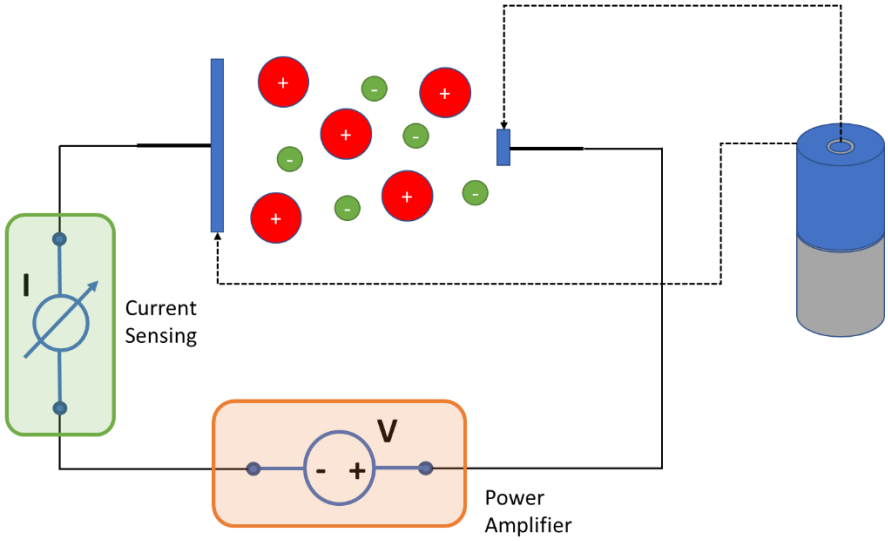

Figure 4.6 . Probe electrical connection: The voltage generator V and the current meter I represent the power amplifier and the current sensing reported in Figure 4.3, respectively.

Let us now introduce some considerations about the selection of the probe excitation signal. For this purpose, we assume, as a first approximation, that the measured ion current is determined only by the resistance of the channel (Figure 4.7)[10] . In Figure 4.7, V represents the excitation voltage whereas the capacitance C includes the parasitic capacitance of the conditioning electronics, mainly due to the cable capacitance (the coaxial cable used to limit interferences introduces a capacitance of approximately 100 pF/m).

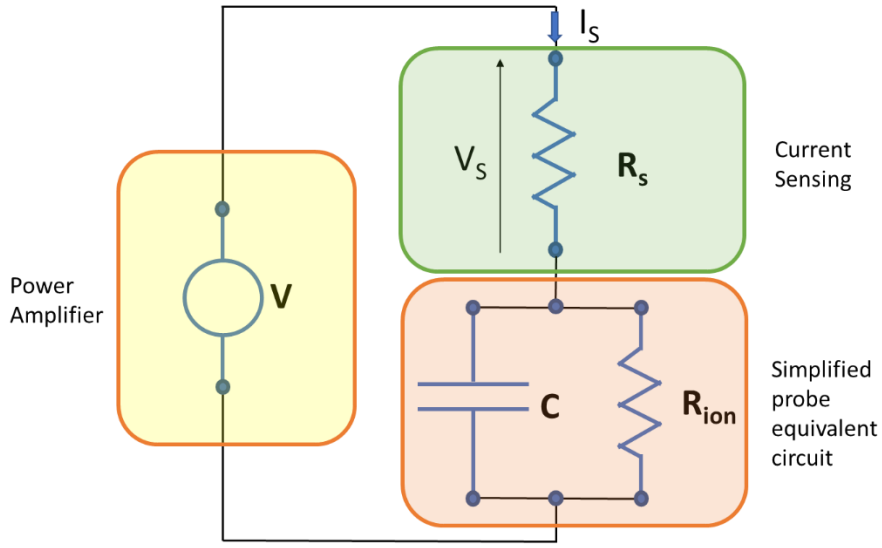

Figure 4.7 - Equivalent simplified circuit of the current probe connected to the conditioning electronics. Rs is the current sensing resistor shown in Figure 4.3.

Considering Figure 4.7 it is possible to derive the expression of the current measured by the instrument (I_s):

$$I_s = \frac{V_s}{R_s} = \frac{V}{Z_{eq} + R_s} \qquad (62)$$

[10] This assumption is not generally valid, as it will be cleared in what follows, but allows for a significant comparison of AC and DC excitations for the measurement of the ion current.

Where Z_{eq} is the equivalent impedance due to R_{ion} and C, and R_s is the shunt resistor of Figure 4.3.

$$Z_{eq} = \frac{R_{Ion}}{1 + j\omega R_{Ion} C} \tag{63}$$

The equation (62) can be written as:

$$I_s = \frac{V}{\frac{R_{Ion}}{1 + j\omega R_{Ion} C} + R_s} \tag{64}$$

From equation (64) it is evident that increasing the excitation frequency, the parasitic capacitance of the cable reduces the sensitivity of the current to ion resistance variations.

4.1 DC Measurements

DC measurements are performed by applying a constant voltage to the probe, which is proportional to the electric field applied between the electrodes. The optimal choice set up is to maximise the electric field applied across the channel without reaching the saturation electric field, as discussed in section 2.3.2.

From equation (64), if a DC excitation is considered ($\omega = 0$), the expression of the current becomes:

$$I_s = V \frac{1}{R_{Ion} + R_s} \quad if \quad \omega = 0 \tag{65}$$

and a good sensitivity to the resistance of the ionic channel can be achieved. Unfortunately, DC measurements have a drawback that is experimentally verified: when using the spark plug, or any other electrode, the ion sensor output under DC polarization, in general after a few hours of

operation, shows a decreasing of the signal amplitude. This attenuation could be explained by the modification of interface between the electrode surface and plasma (including the deposition of residues, oxidation reactions, etc.).

The problem of oxidation can be attenuated, as already discussed, by the use of Pt/Rh shielded electrodes, where chemical reactions are strongly reduced. Nevertheless, DC measurements are not suitable for continuous monitoring applications.

4.2 AC Measurements

On the basis of the considerations reported in previous section, the measurements with zero-offset AC excitation signals are more robust and suitable for continuous monitoring applications. Periodically changing the sign of the applied voltage, on the electrode surface there is a reduced accumulation of residues as well as a slowdown of the oxidation processes and a reduction of the double layer capacitance effect, which result in a better stability with time. The drawback, as already discussed, is that with this kind of measurements, from eq. (64), the dependence on the ion resistance gets lower if the frequency increases. As an example, considering a cable 10m long and an ion channel equivalent resistance of $10M\Omega$, we are in the conditions described by equation (65) if:

$$\omega \ll \frac{1}{2\pi R_{Ion} C} \cong 16\ Hz \qquad (66)$$

4.3 Low Frequency Square Wave Measurements

On the basis of the above discussion, a good solution for this kind of measurements is to use a square wave excitation signal at very low frequency. Using a square wave at some Hz it is possible, continuously inverting the polarity of the electric field applied to the electrodes, to avoid the signal degradation over time. The measurements must be taken in the two semi periods when we have a

DC excitation. Obviously, the square wave signal must be with zero average value otherwise there are no benefits, and the signal degradation will occur anyway. The limit of this approach is that we have not a complete real time monitoring of the ion channel. During the transients of the excitation signal from negative to positive values and vice versa, there is a perturbation of the measurement with a consequent stabilization time during which the measurement is not significant. This time increases as the parasitic capacitances increase. Moreover, as previously discussed, using asymmetric electrodes geometries the signal is rectified and so the measurements can be taken only during one semi period. This aspect implies that the ion current can be monitored only for about 50% of the time, assuming a 50% duty cycle. A signal acquired using this technique is shown in Figure 4.8.

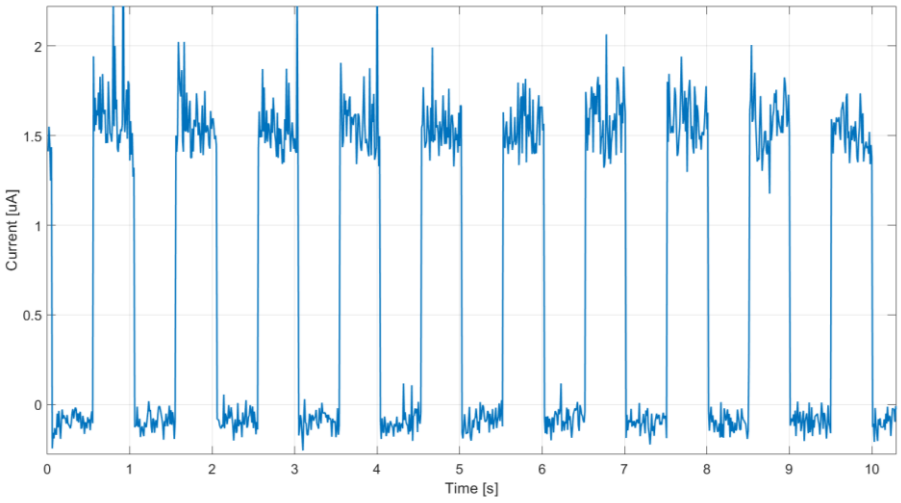

Figure 4.8 – A plot of the measured current in presence of flame using a zero-average square wave voltage excitation.

Even if this measurement technique allows to perform a monitoring only for the 50% of time, it compensates the relevant parasitic effects, avoiding the signal degradation over time, and allowing for a continuous monitoring. The typical ion current signal has a mean value related to the average combustion conditions, characterized by a stationarity time greater than the square wave excitation period (1s), superimposed to random and large-bandwidth fluctuations related to the fluid dynamical turbulence intrinsic in the observed combustion process, characterized by a stationarity time that is much faster than the execution period. The statistical characteristics (probability density function) of these fluctuations are related to the combustion conditions. Despite the simple set-up

needed for ion current measurement, this measurement technique is in principle particularly rich in information: in fact, the concentration of the ions depends on all the combustion process conditions, such as fuel composition, air to fuel ratio, temperature and so on. The ion current signal average magnitude and power allow for monitoring the combustion working conditions, whereas the dynamic behaviour in time or frequency domain allows for monitoring the dynamic behaviour as well as the turbulent characteristics.

The measurements reported in the following sections were obtained with 0-offset square-wave excitation signals with 50% duty cycle and peak-to-peak amplitude in the range (0 – 38 V).

In summary, in the first part of this thesis a complete model for ion sensors based on the electrode of the spare spark plugs already present on was developed was developed starting from the theory of Langmuir probes. A model of this type, specifically aimed at understanding the measurement performance, is missing in the literature, instead simplified models are used which, however, have limited value to the chosen working point. The proposed model, which also takes into account the physical effect of the gas/electrode interfaces, has also made it possible to develop an original measurement technique exploiting a low frequency AC square wave biasing of the electrodes, which allows to compensate for some relevant parasitic effects maintaining, at the same time, the possibility to simultaneously measure the DC component (a function of the air to fuel ratio) and the AC component (a function of the flame pulsations) of the ion current signal.

5 Ion Current Tests

The measurement setup and the ion probe have been tested in the burner test bench changing the combustion conditions and measuring simultaneously the exhaust gas composition in terms of CO, NOx and O_2 as well as the I-V characteristic of the ion probe.

The targets of the tests can be divided in:

1. Verify the proposed model for the ion probe in presence of flame.

2. Verify the dependence of the ion current on the equivalent ratio (lambda factor) of the combustible mixture.

3. Verify the possibility to detect flame instabilities by ion current measurements.

To this aim, the flame of the burner in Figure 4.1 is supplied by an air flow and a gas flow whose values can be adjusted to fix the mixture composition.

5.1 Test 1: I-V Model Verification

The first aim was to experimentally verify if the developed model for the ion probe can be experimentally verified. During measurements, the amplitude of the square wave excitation was varied from 0 Vpp up to 38 Vpp[11], and the positive and the negative semi periods of the waveform were used to measure the negative and the positive current at the given excitation. In the graph in Figure 5.1, two I-V curves are reported, the first one in absence of flame and the second one in presence of a flame supplied by a gas mixture with a fixed lambda factor and constant power. What can be immediately seen is that the spark plug used as a probe has a parasitic resistance (due to

[11] Vpp: Peak to peak voltage.

insulation losses) that allows a significant current flowing also in absence of the ion channel. From this observation, it was necessary to introduce in the probe model a parasitic resistance to consider this loss (R_{loss}). The equivalent circuit that includes the ion channel, the probe effect, and the parasitic resistance is reported in Figure 5.2. The total current measured by the instrument, affected by the parasitic resistance can be written as:

$$I_{measured} = I + \frac{V_{ext}}{R_{loss}} \tag{67}$$

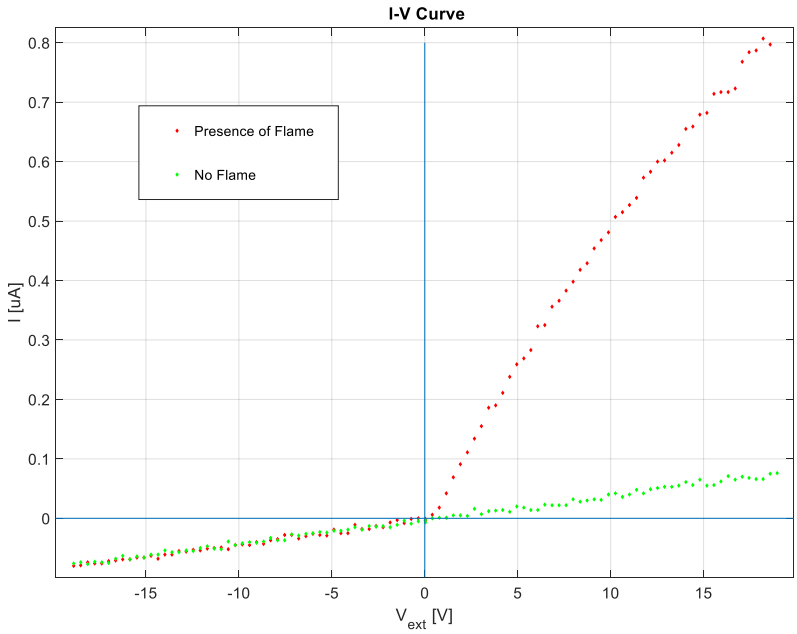

Figure 5.1 – I-V characteristics of the probe in presence and in absence of flame.

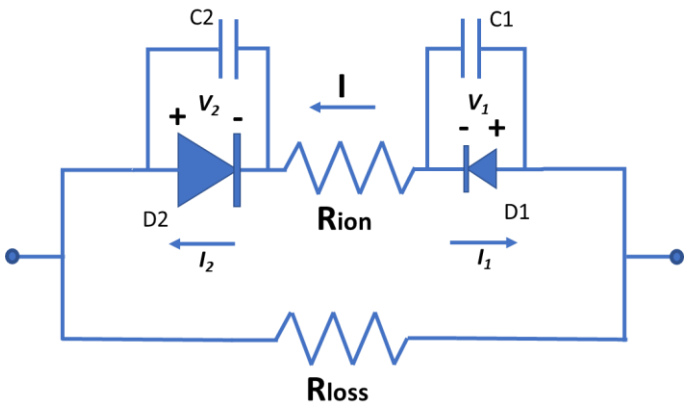

Figure 5.2 - Ion current probe model considering the loss resistance.

From the Figure 5.1, it is evident that the ion channel and the electrodes exhibit, as expected, a rectification effect. When the positive voltage is applied to the outer electrode of the probe the current flowing through the channel and the electrodes is much lower than with the opposite polarization. This effect is due to the asymmetric structure of the probe, as discussed in the probe model section and shown in Figure 3.9. The surface of the inner electrode is much smaller than the outer electrode surface, that is also connected to the burner metal structure. The theoretical discussion previously presented explains the asymmetry of the I-V characteristic that brings to an effect known as flame rectification. Flame rectification sensors are currently employed as flame detectors.

A nonlinear fitting of the data reported in Figure 5.1 was performed, selecting free parameters the plasma density (n_p), the electron mobility in the plasma (μ_e), and the plasma temperature ($T=T_i=T_e$), whereas R_{loss} was estimated from the no-flame measurement. The same value for the temperature of ions and electrons was considered, assuming to be in presence of a thermal plasmas[12]. In the following table, the parameters obtained from the fitting procedure are reported. It is necessary to remark that the model has a physical consistence only if the Debye length is smaller than the distance between the electrodes that is approximately 3mm.

[12] A non-thermal plasma, or cold plasma, is a plasma in which electrons and ions are not at the thermodynamic equilibrium (Ti is different from Te).

Lambda (λ)	$\mathbf{n_p}$ [ions/m^3]	μ_e [m^2/ (V s)]	**T** [K]	λ_d [mm]	$\mathbf{R_{loss}}$ [MΩ]
0.81	*0.72 * 10^{13}*	*100*	*1000*	*0.81*	*300*
No flame	*0*	-	-	-	*300*

Table 2 – Model parameters to fit experimental data in Test 1.

In Figure 5.3, the fitted model (solid line) is reported together with the experimental data (dots).

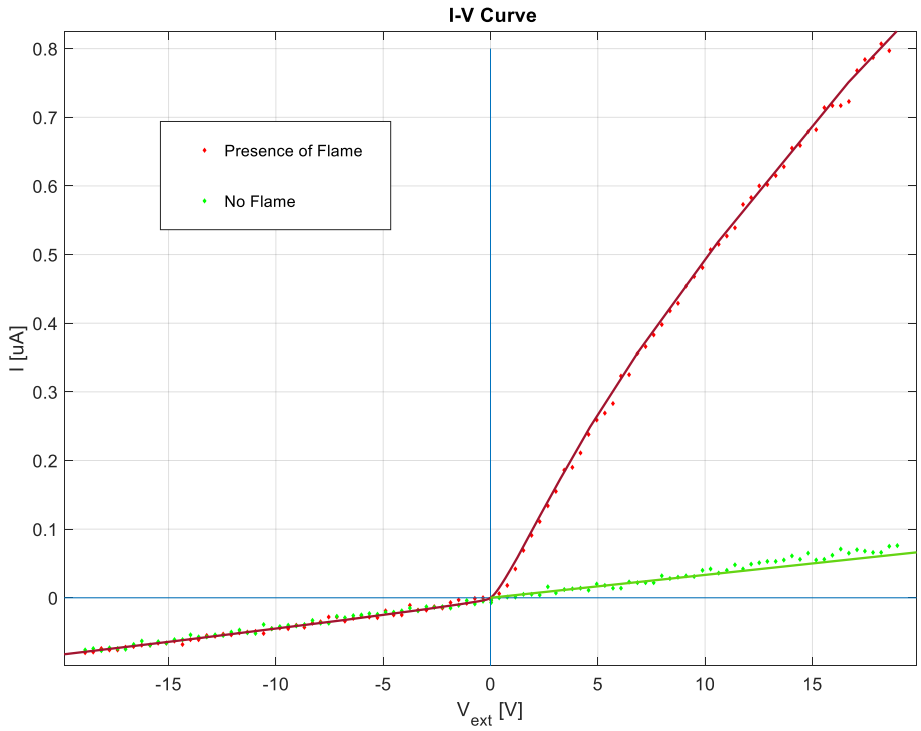

Figure 5.3 – Model fitting on the data of Figure 5.1.

During the tests, we noticed an apparently strange behaviour of the current probe when the burner is turned on with the probe at environmental temperature (the data used for the model fitting have been acquired when the burner and the probe were at the thermal regime). In detail, when the

burner is turned on, some seconds after the flame ignition, the amplitude of the output signal gradually increases losing the asymmetry characteristics (rectification effect) and returns to its normal behaviour after some tens of seconds. This effect, shown in Figure 5.4, was observed in both the laboratory burner tests and during the test with a gas turbine burner in a BH test rig.

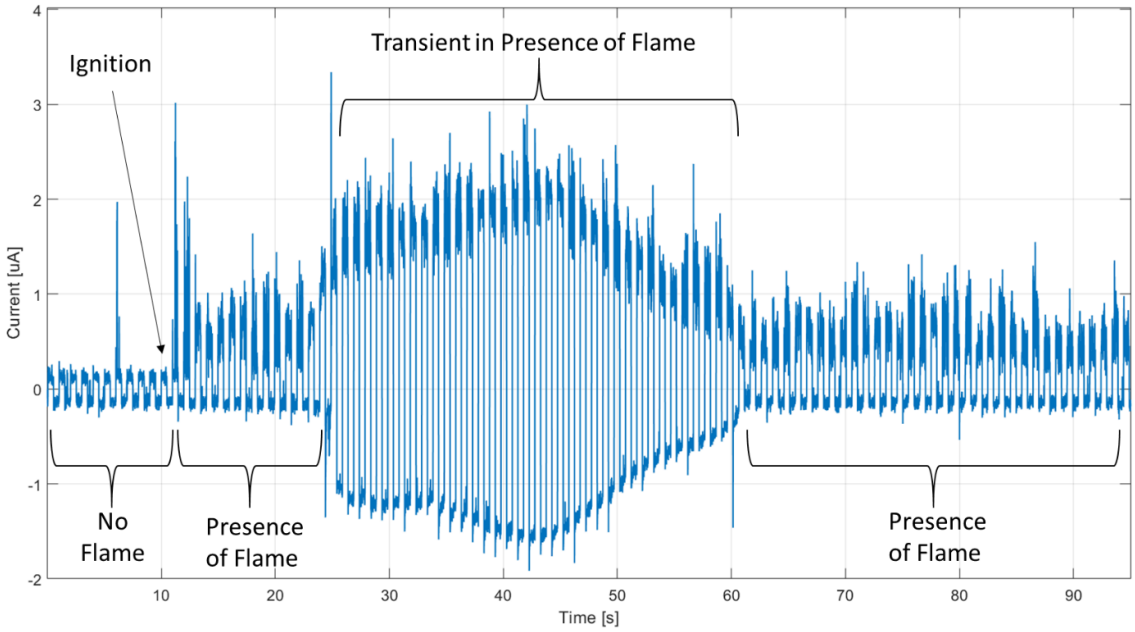

Figure 5.4 - Start-up behaviour of the ion current signal.

A possible explanation of this phenomenon is the condensation of water. At the burner start up the spark plug is relatively cold with respect to the gases of the flame, that contain a relevant quantity of water vapor. The vapor, in contact with the spark plug, condenses generating liquid water. When the quantity of water on the spark plug is sufficient to short the electrodes, we observe the unexpected effect. The liquid water introduces an additional loss resistance in the probe, a part of the current flows through the water, strongly reducing the rectifying effect. When the temperature of the probe is sufficiently high, the liquid water evaporates, and no other water vapor can condense on the electrode surfaces. After this thermal transient, the behaviour of the probe in presence of flame returns at the nominal one. Since this effect dies out in a few seconds after the start-up, it does not represent a problem for the measurements, but must be taken into account in case of cold start-up.

5.2 Test 2: Ion Current behaviour as a function of Lambda

In this section the results obtained changing the equivalent ratio of the combustible mixture are presented and discussed. The tests on the burner were performed using the measurement setup previously described using propane (C_3H_8) as fuel. The lambda factor of the mixture was changed according to what sown in Table 3.

C_3H_8 Flow [LPM]	Air Flow [LPM]	C_3H_8 [%]	O_2 [%]	N_2 [%]	Lambda (λ)	Power [W]
3.09	68.01	4.35	20.09	75.56	**0.88**	4714.82
2.78	68.01	3.93	20.17	75.89	**0.98**	4243.34
2.47	68.01	3.51	20.26	76.23	**1.10**	3771.86
2.16	68.01	3.08	20.35	76.56	**1.26**	3300.38
1.86	68.01	2.66	20.44	76.90	**1.47**	2828.89

Table 3 - Premixed flow composition and burner power during Test 2. The gas flows are reported in litres per minutes.

In Figure 5.5 the I-V curves for the different values of lambda are reported (dots), together with the fittings (solid lines). The model parameters obtained from the fitting on the experimental data are shown in Table 4.

Lambda (λ)	n_p [ions/m³]	μ_e [m²/ (V s)]	T_e [K]	T_i [K]	λ_d [mm]	R_{loss} [MΩ]
0.88	*$1.15 * 10^{13}$*	*80*	*2000*	*2000*	*0.91*	*300*
0.98	*$1.35 * 10^{13}$*	*80*	*1500*	*1500*	*0.72*	*300*
1.10	*$1.78 * 10^{13}$*	*80*	*1000*	*1000*	*0.52*	*300*
1.26	*$1.55 * 10^{13}$*	*80*	*1000*	*1000*	*0.55*	*300*
1.47	*$0.80 * 10^{13}$*	*80*	*25000*	*1000*	*3.9*	*300*

Table 4 – Model parameters obtained from the fitting of the experimental data in Test 2.

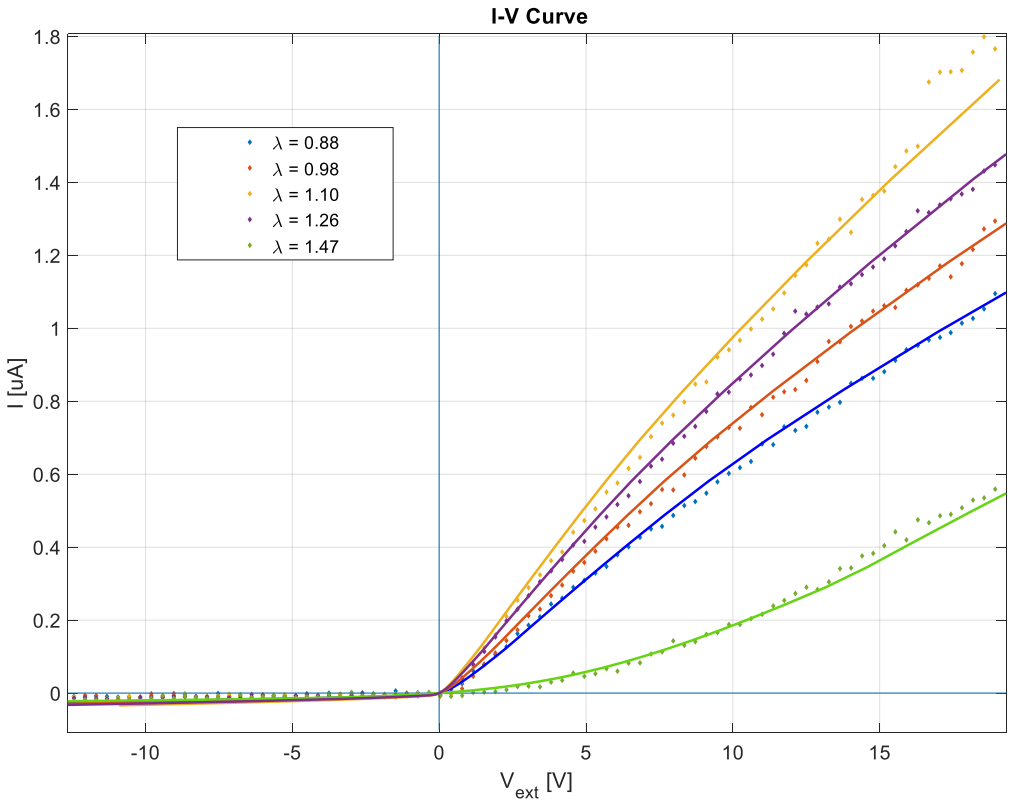

Figure 5.5 – Ionic current experimental data (dots) and fitting (solid lines) as a function of lambda.

A first comment about the results obtained is relative to the Debye length. Only the data which imply a Debye length smaller than the electrode distance can be fully described by the model. In these measurements this hypothesis is always verified except for the lowest plasma density (last row of Table 3): in this case the model can fit the I-V curves only increasing the temperature of the electrons, which causes an increasing of the Debye length as described in (54). This probably means that the plasma density in this case is too low to be measured with this probe.

In Figure 5.6 the plasma density as a function of the lambda parameter is plotted: the dots represent the n_p values reported in Table 4 whereas the solid line is a cubic interpolation of data. The behaviour of the curve in Figure 5.6 closely resembles the qualitative behaviour in Figure 2.3, the numerical simulation in Figure 2.7 and results from the literature [31]. The main difference is that the peak of the curve is shifted towards lager lambda values with respect to what expected

from the theory. This difference can be explained considering that, in practice, even if we exploit a premixed burner, not all the air is used for the combustion: a fraction of the air flows between the metal structure of the burner and the flame allowing the cooling of the burner. A more accurate measurement setup should be used to have a precise dosing of the premixed air. In any case, also in a real application we can expect a similar behaviour that can be compensated by calibration.

In any case, the results confirm the possibility to exploit the ion current measurements to monitor the equivalent ratio changes of the combustible mixture.

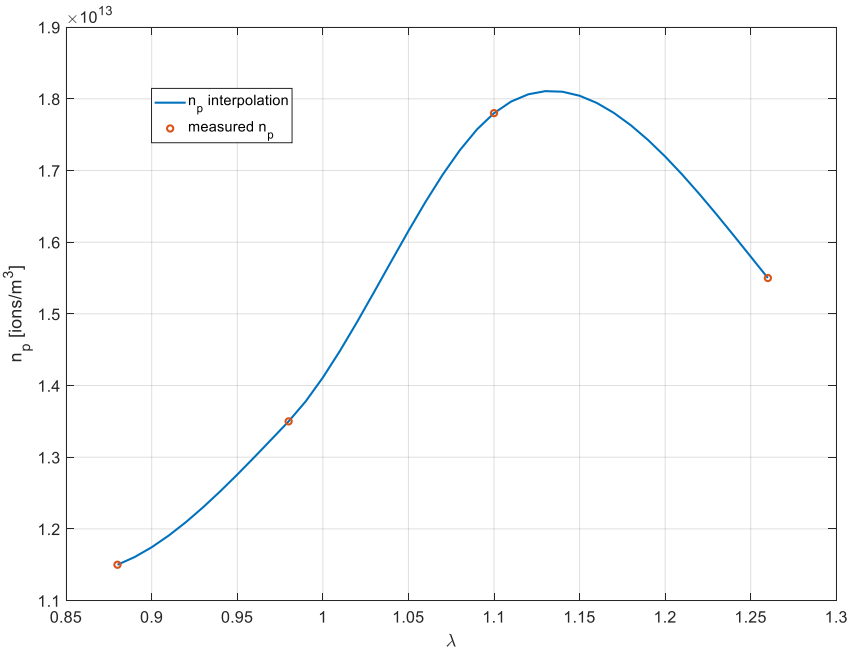

Figure 5.6 – Plasma density as a function of lambda in Test 2.

A second comment concerns the concentrations of carbon monoxide and nitric oxides in exhaust gases at different lambda values, which were measured using the instrument designed in section 6. The measured concentrations of CO and NOx are reported as a function of λ in Figure 5.7, together with O_2 concentration, after a correction performed on the basis of equation (68), where O_2Ref = 15%.

$$[Gas]_{corr} = [Gas] * \frac{21\% - O_2 Ref}{21\% - [O_2]} \tag{68}$$

The reason for the correction is the air present in the exhaust pipe not coming from the combustion (cooling air of the burner): the exhaust gases are diluted, and the measure of CO or NOx concentrations result therefore smaller than they actually are. Using an oxygen sensor, the measurement of these toxic components can be corrected to account for the dilution with air. The value of 15% of O_2 is usually used as a reference for combustion exhaust gases, whereas 21% represents the oxygen fraction present in air, that is assumed to be constant.

From Figure 5.7, as expected, increasing the lambda factor the concentration of nitric oxides is strongly reduced [32] due to a lower flame temperature. The behavior of the NOx with lambda is widely reproducible, whereas the CO concentration appears to be very hard to be correlated with lambda: especially for low values of this parameter, [CO] presents strong variations in different nominally equal measurements, confirming, as already discussed, that several variables contribute to determining it.

Moreover, the combustion process decreases the oxygen concentration according to the lambda value: the exhaust gases contain less oxygen when the premixed mixture is reach in fuel (lower lambda).

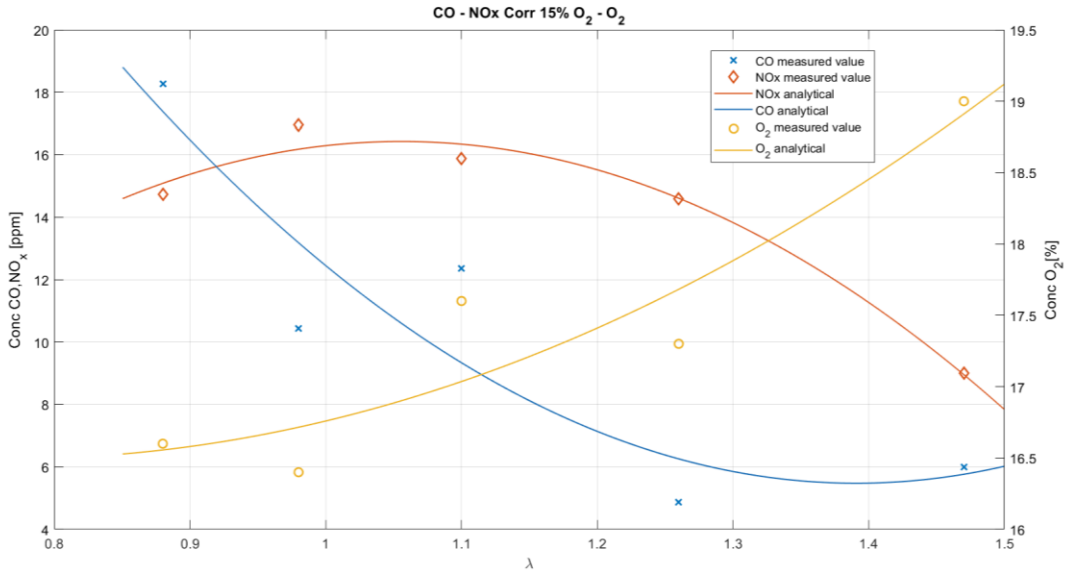

Figure 5.7 – Exhaust gas composition for different lambda values in Test 2. Oxygen is expressed as percentage in volume and CO and NOx are expressed as part per million (ppm) in volume. Markers: average value on 2 measurements; Solid lines: cubic fitting.

The repeatability of the ion current measurement presented in this section was also preliminary tested. The test bench used for the measurements is not optimal from this point of view due to the low accuracy in the fuel and air dosing, and due to the absence of a control for temperature and humidity control of the supplied air. In any case, the repeatability test gave encouraging results as it can be seen in Figure 5.8. The same set of air to fuel ratios were used in two different burner runs (preheated burner) performed in different days. The I-V curves in the two runs are still well distinguishable for different lambda values.

These results, to be confirmed with further tests in industrial test rigs, suggest a significant correlation, as expected, among ion current, the equivalence ratio of the combustible mixture, and the exhaust gases composition.

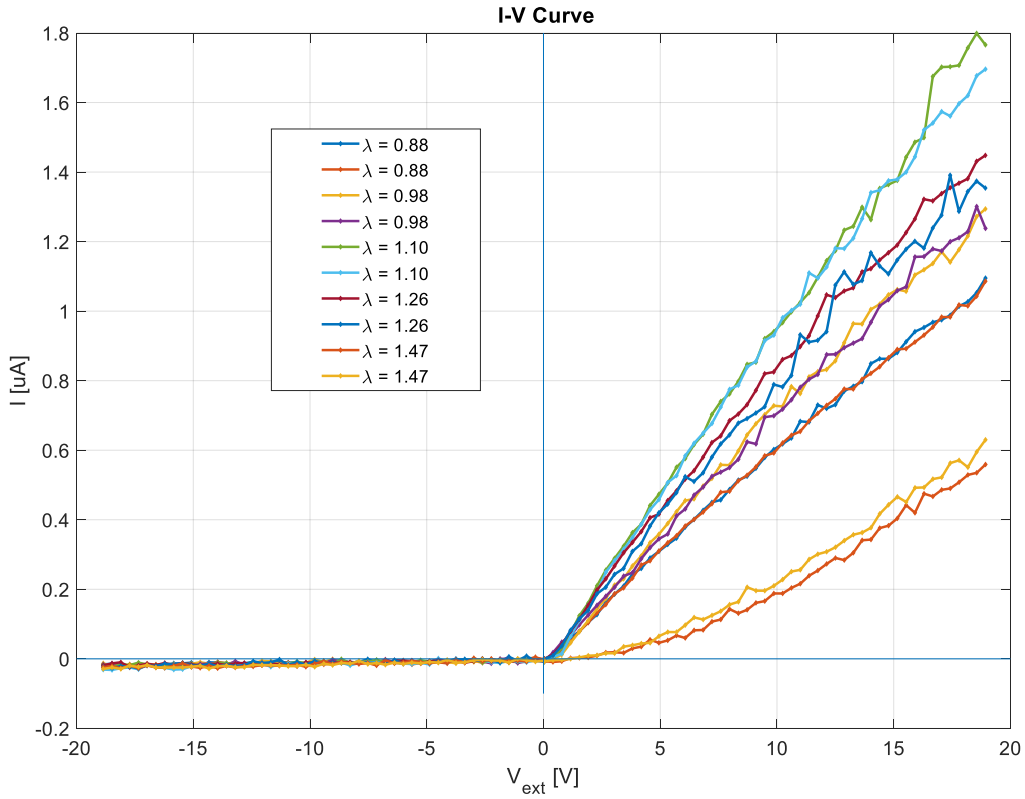

Figure 5.8 – I-V curves for different λ values repeatability test.

5.3 Ion Sensor to detect flame instabilities.

Another interesting application of the ion current measurements is the monitoring of the dynamic behaviour of the flame. Flame fluctuations, instabilities or other fluid dynamics behaviours cause a changing over time of the ion density distribution. These changes can be detected by the ion probe as an AC component superimposed on the DC signal that is mainly dependent, as previously discussed, on the average ion density and, therefore, to the combustible mixture composition. In Figure 5.9 it is shown an example of time domain current signal measured by the probe during a test consisting in the start-up of the burner, followed by a gradual leaning of the combustible mixture. The leaning of the mixture, at a certain point, triggers a flame instability condition that is

followed by a flame loss[13] event. This is a typical situation that is important to detect in a burner, especially for those burners that operate with a very lean combustible mixture. A fast detection of flame instabilities can be very useful to avoid flame losses.

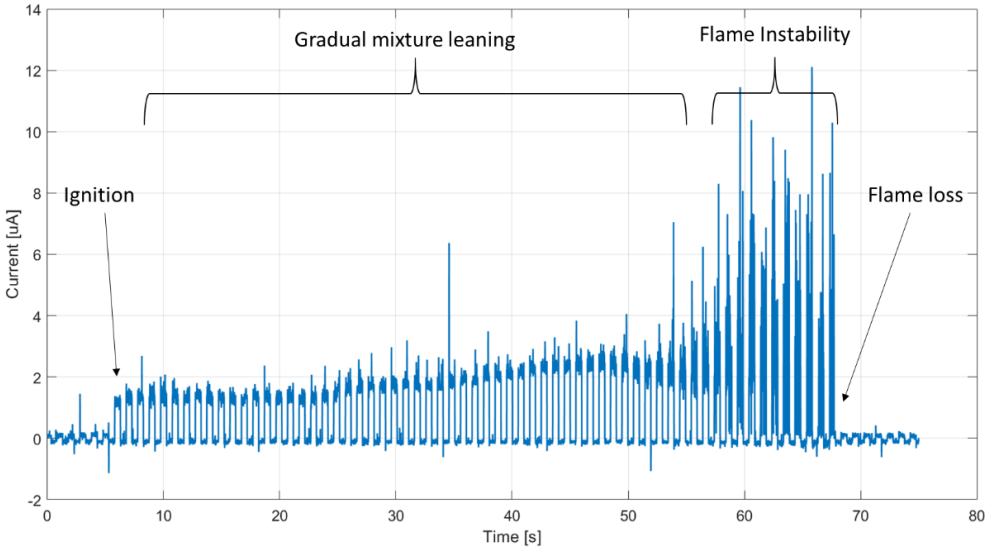

Figure 5.9 - Experimental signal obtained from the ion sensor during the transition from a rich to a lean mixture. At the end of the transition phase, a flame instability with a consequent flame shutdown occurs.

In Figure 5.10, the standard deviation and the mean value of the ion current signal in Figure 5.9, evaluated during the positive semi period of the square wave excitation, is reported. The average value of the ion current, after approximately *30s,* starts to increase up to a maximum at approximately *t=50s* when it starts to decrease. This is the behavior of ion density explained in Figure 5.6, when the lambda factor is increased. However, in this test, the interesting result is the standard deviation of the ion current signal. The value of the standard deviation dramatically increases when the instability of the flame becomes relevant. This parameter can be a very useful indicator of the flame instability, that can be easily obtained without increasing the complexity of the measurement instrument [30].

[13] A "flame loss" is intended as an unexpected flame extinguishing event.

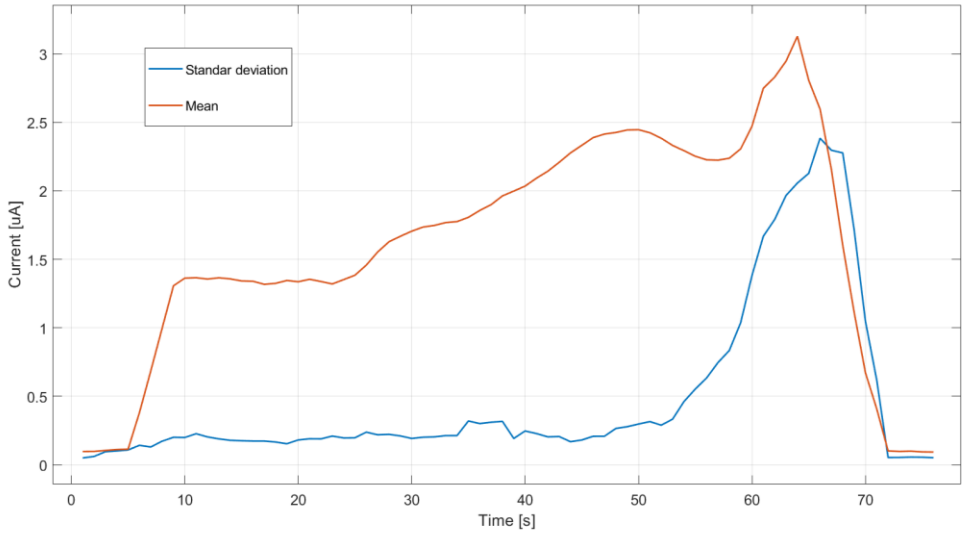

Figure 5.10 – Mean and Standard deviation of the ion current signal in the positive semi period during the transition from a rich to a lean mixture reported in Figure 5.9.

If a gas turbine burner is considered, exploiting the same technique it is possible to also measure the pressure peaks that may occur in the combustion chamber due to flame instability or other causes. The detection of these events is usually performed exploiting pressure sensors. In Figure 5.11 it is shown the comparison of a dynamic pressure piezoelectric sensor output with the spectrum of the measured ion current. The measurement was performed on a gas turbine burner using a spare spark plug as ion sensor. The 180 Hz harmonic corresponds to a flame instability condition. The study of this type of application will be object of future developments of this work.

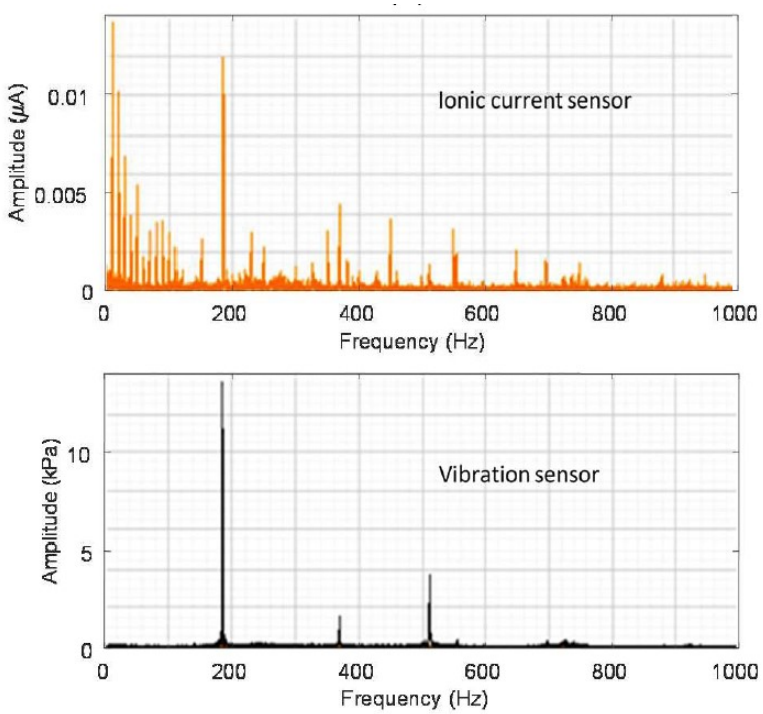

Figure 5.11 - Experimental results obtained from ion sensor compared to a pressure sensor under flame instability condition (pressure pulsations at 180 Hz) in a gas turbine rig [24].

5.4 Ion current measurement optimizations

In this section the possibility of improving the versatility of the ion current measurements is briefly discussed. Up to now, we characterized the ion channel and probe behaviour measuring the current voltage (I-V) curve. This task can be easily performed in a laboratory where the conditions of the probe over time are constant and controlled, with the flame maintained stable during the measurement time. On the fields, these conditions cannot be guaranteed, and it is necessary to make the measurement procedure faster and more robust.

5.4.1 Single current measurement approximation

The measurement of the I-V curve is performed, as previously explained in section 5.1, by exciting the probe with a 1 Hz square wave with different amplitudes, while measuring the current. In practice, this procedure is time consuming since the current is measured, for a single voltage excitation, averaging over one period (1 second). To increase the resolution (number of points in the I-V curve) we need a larger acquisition time. Supposing to acquire *n* points we need at least *n* seconds to obtain the curve. This is an enormous amount of time that completely cancels one of the main advantages of the ion current sensor, i.e. the fast response time. In practice, once the measurement system has been characterized, a good approximation to get an estimation of the plasma density is to excite the probe at the maximum voltage and acquire only one period. In Figure 5.12 different plasma densities are reported, calculated by the fitting procedure exploiting the physical model previously presented, from measurements at different lambda values. From the same measurements, the current mean value at the maximum positive voltage excitation (+19V) was obtained: the values are reported in Figure 5.13 as a function of lambda.

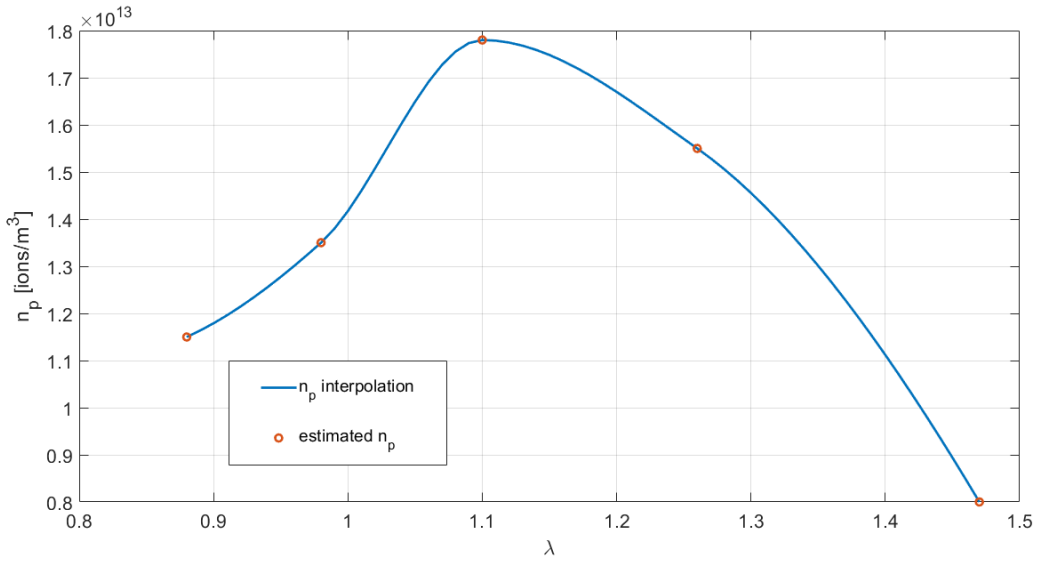

Figure 5.12 – Estimated plasma density as a function of λ obtained using the proposed model.

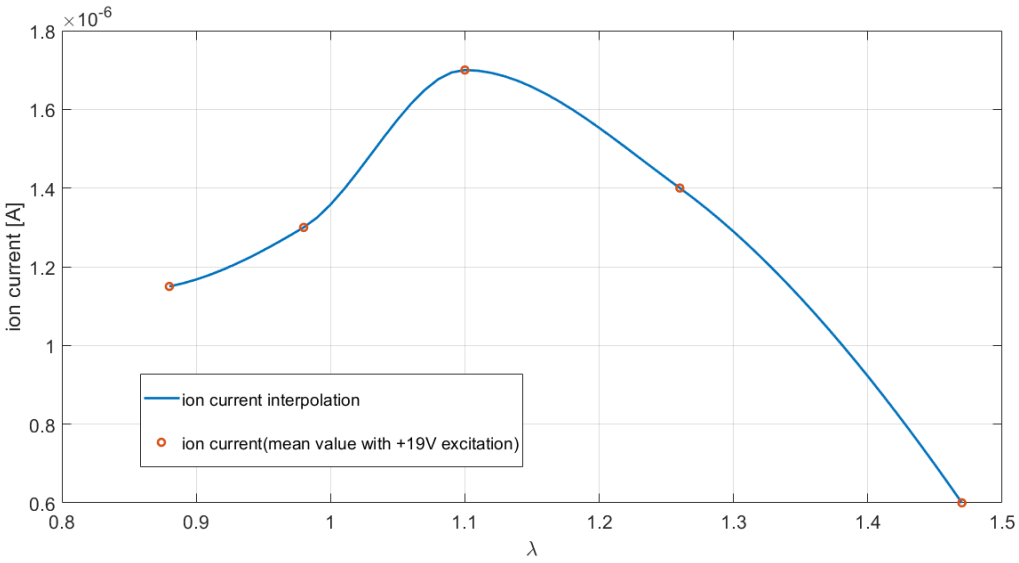

Figure 5.13 – Ion current mean value with a voltage excitation of +19V as a function of λ.

The measurements and the data fitting used are the same of Table 4. The data reported in the previous figures were obtained from the measurements discussed in section 5.2. In Figure 5.14 the maximum positive currents (mean values) shown in Figure 5.13 are plotted as a function of the ion densities calculated by the model fitting as shown in Figure 5.12.

As it can be immediately noticed, for high excitation voltages there is a quasi-linear relationship between ion density estimated by fitting the model on a complete set of I-V data and the mean value of the current measured at the maximum voltage excitation. Using this linear calibration, for a practical implementation, it is possible to get the ion density information by measuring only one current value with a constant voltage excitation, significantly reducing the measurement time.

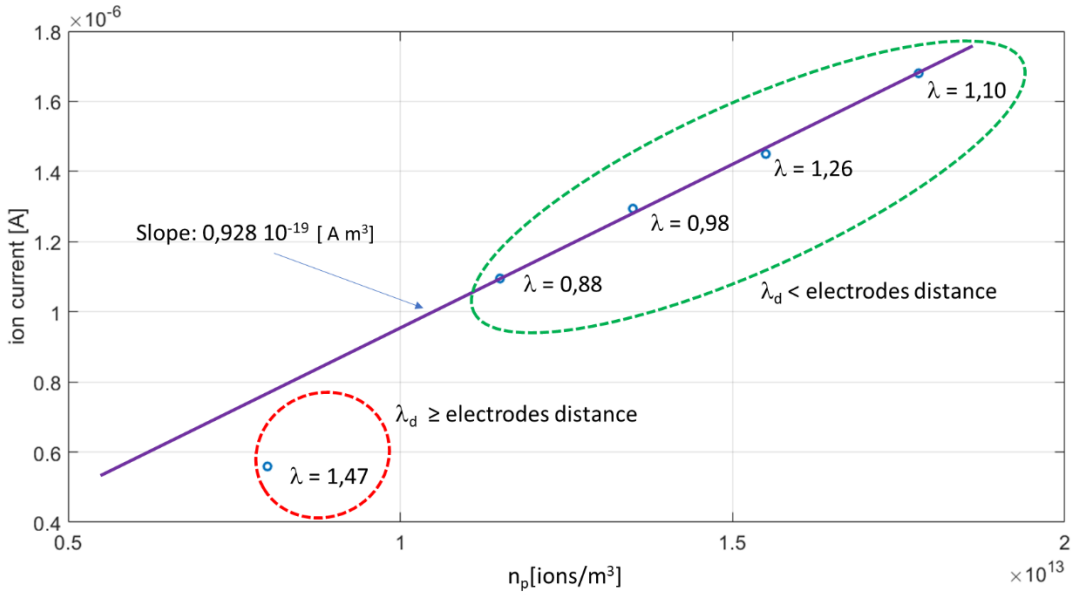

Figure 5.14 – Ion current mean value measured with an excitation of 19V as a function of the model estimated plasma density n_p.

As a last comment, in Figure 5.14 there is one measurement, that is not compatible with the linear relationship ion current – n_p: this measurement, according to the model fitting results, is associated with a lower plasma density with a Debye length that is comparable with the electrode distance. In other words, this measurement cannot be interpreted, as already discussed, with the proposed model. Given the probe, and in particular its dimensions, an admissible range of plasma densities is also given in which the measurements are meaningful.

5.4.2 Negative Current Compensation

In section 5.1 the problem of the parasitic resistance due to the reduced insulation of the spark plug was discussed. Considering that the measured currents are of the order of 10^{-6}A with an excitation amplitude of 19 V, the measured equivalent channel resistance is of the order of $20M\Omega$. The parasitic resistance should be at least an order of magnitude greater to be neglected. For lower values of the parasitic resistance a compensation needs to be performed estimating its value exploiting the signal in absence of flame. A further possibility to find the parasitic resistance is to consider the negative part of the ion current signal, where the rectification effect makes the ion

signal negligible. In this way, we can compensate the parasitic resistance in each sampling period, solving the problem of possible drifts of the parasitic resistance value with time, temperature, or other uncontrolled parameters.

In detail, a simple method to remove the parasitic resistance and others parasitic effects that affect both negative and positive parts of the ion current signal is to subtract the negative part of the signal from the positive one. In this way, the parasitic resistance effect can be cancelled. This method is very easy to be implemented (also directly in hardware by a specific electronics). The positive part of the I-V characteristic, that is the one interesting for the ion density estimation, can be compensated as follow:

$$I_{comp}(V > 0) = I(V) - I(-V) \tag{69}$$

The result of this compensation is shown in Figure 5.15 for a subset of measurements reported in Figure 5.3 and Figure 5.5.

In Figure 5.15, the light blue line represents the measurement performed in absence of the flame (current due to the parasitic effects of the probe). Subtracting the negative part of the signal, this line becomes flat and the other measurements become independent on probe losses.

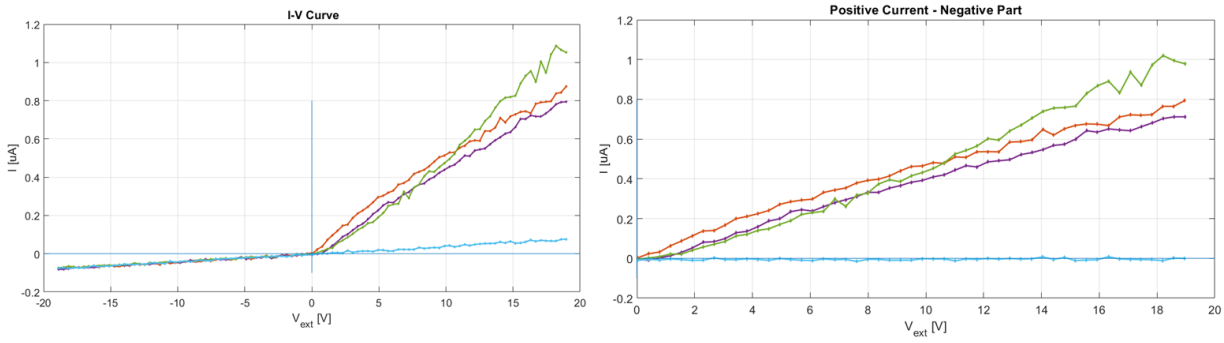

Figure 5.15 – Measurement compensation on the basis of equation (69). On the left: uncompensated measurements, on the right: compensated measurements.

5.5 Gas turbine burner test

The proposed measurement system was tested, exploiting the same spark plug, on a gas turbine burner in a BH plant in Florence. The burner was tested in special test bench to monitor the combustion with different type of fuels and different working conditions. The burners used in gas turbines have usually a structure like the one showed in Figure 5.16. The fuel that supplies the flame is provided by two lines. One line supplies the so-called *pilot burner stage*, usually positioned in the middle of the burner. The pilot burner combustible mixture has usually a lambda value close to one and it is used to turn on the burner more easily. A second gas line supplies the so-called *split or main burner stage* with a combustible mixture, which is usually characterized by a lambda value < 1 (lean combustible mixture). After the burner start up, gradually decreasing the fraction of gas that supplies the pilot stage and increasing the fraction of gas that supplies the split stage, the burner is set to operate with a leaner mixture. The idea behind the use of lean combustible mixtures is to maintain as high as possible the burner efficiency and to reduce the production of NOx compounds. The drawback in operating with a lean mixture is that the combustion is more instable, and a more accurate combustion control is required.

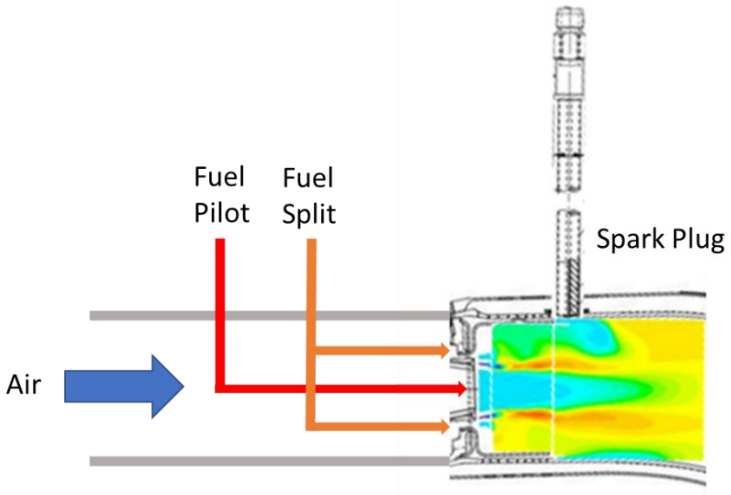

Figure 5.16 – A typical gas turbine burner structure.

5.5.1 Burner start-up

As observed in section 5.1, at the burner start-up there is a transient phase in which the ion current signal becomes symmetric and very large in amplitude. During the test at the BH plant the same behaviour was observed. The initial transient of the ion current after the flame ignition is shown in Figure 5.17.

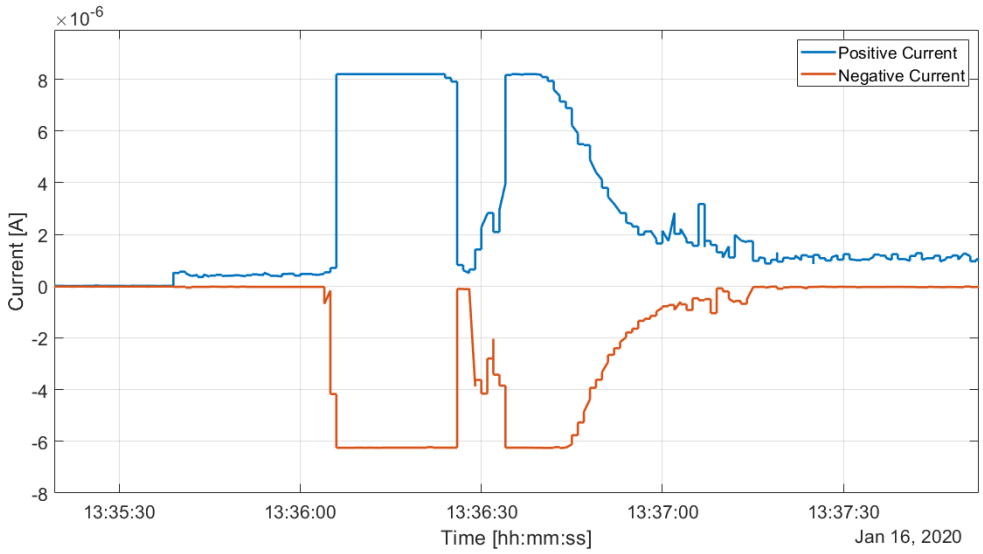

Figure 5.17 – Ion current mean value initial transient during a gas turbine test.

The explanation can be, as already discussed, the condensation of water between the two electrodes due to the lower temperature of the spark plug with respect to the flame. When the temperature of the probe increases, this effect disappears. As observed in the laboratory tests, if the flame is turned off and re-ignited without leaving time to the probe to cool down, this effect is not observed.

5.5.2 Pilot-Split fuel dosing

In Figure 5.18 an example of the ion current signal as a function of time together with the pilot-split gas supply percentage is shown. The data were acquired during a measurement in a BH test rig in Florence. With reference to the pilot-split signal, a value of 100% means that all the fuel is injected in the pilot stage and no fuel is supplied to the split stage. A value of 0% means, on the other hand, that all the fuel is supplied to the split stage. As explained before, during this test, the

equivalent ratio of the combustible mixture of the burner is changed since the split stage mixture is leaner than the pilot stage mixture. Gradually decreasing the pilot-split percentage, the global mixture gets leaner.

As it can be seen, the ion current signal decreases as the mixture becomes leaner, as expected from the theoretical analysis and from laboratory tests. In Figure 5.19, for the same test of Figure 5.18, the exhaust gas composition in terms of CO and NOx is reported. As expected, the leaning of the mixture, detectable by the ion current probe, brings to a reduction of NOx in the exhaust gases.

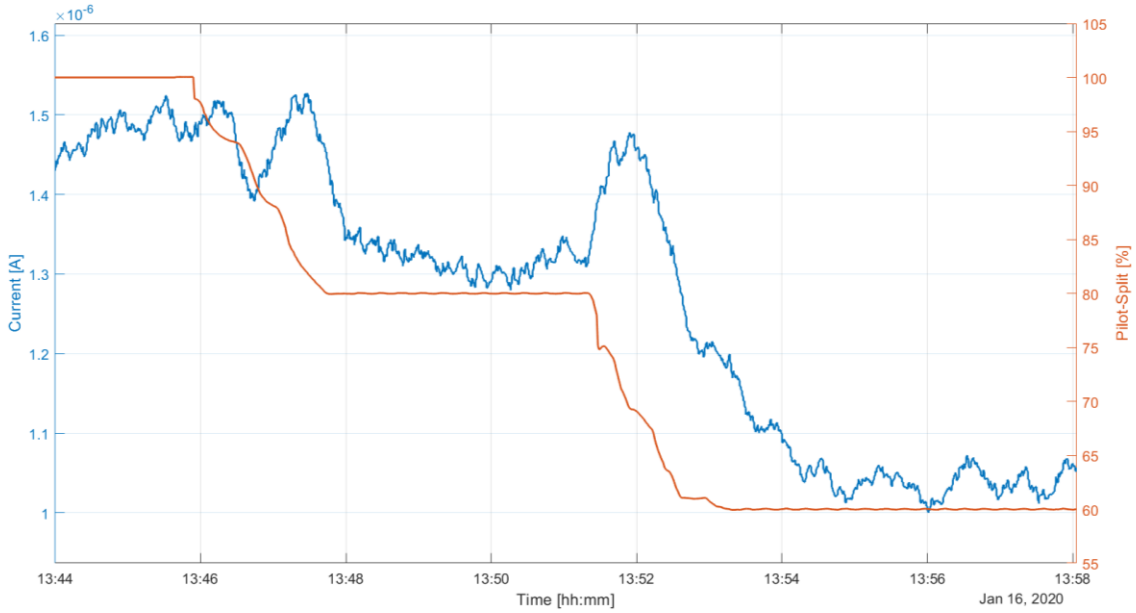

Figure 5.18 – Example of ion current signal and pilot-split % signal as a function of time during a BH gas turbine test.

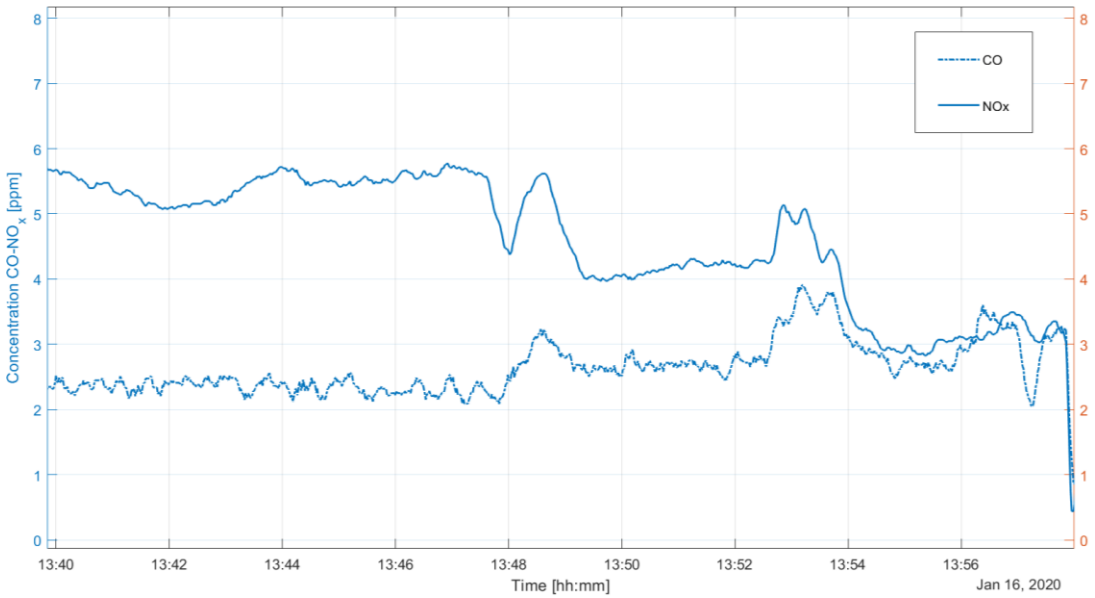

Figure 5.19 – Exhaust gas composition in terms of CO, NOx in the gas turbine test of Figure 5.18.

5.6 Ion current measurement considerations

Summarizing, in this section, preliminary ion current measurements performed on industrial turbine burners were presented. For the tests, a spark plug probe with asymmetric electrodes, that are the most common solutions both in boilers burners and in gas turbine or aircraft engines, was used. The measurement of the DC component of the ion current, and so of the average ion density in the combustion area, was verified to give useful information about the mixture composition in terms of fuel and air. A variation of the mixing ratio theoretically changes the ion density, and this effect can be measured also in practical tests with a good repeatability, using the ion current data. The measurement of the AC components of the ion current signal, in the other hand, can give useful information about the flame stability and/or the presence of pressure pulsation in the combustion chamber. There is an evident correlation of the ion current values with the concentration of NOx compounds in the exhaust gases. The NOx concentration is mainly a function of the flame temperature, and the flame temperature decreases as the combustible mixture

becomes leaner. The main advantage of the ion current measurements is the fast sensor response time, while exhaust gas measurements are inevitably slower. A deviation from the expected behaviour of the ion current can immediately trigger the control system to stabilize the flame, avoiding flame loss events and drastically reducing toxic compound emissions.

The spark plug used as ion current sensor can immediately find application as flame detector but the information coming from the signal can be also used to detect flame instabilities or pulsations. The use of the ion sensor to detect the air to fuel ratio needs a more accurate analysis and more tests on burners, but the results are very encouraging. The important aspect of this type of measurements is that all the information come from a single non-invasive sensor (the ignition spark plug is present in almost all type of burners, independently on the application) connected to a simple and inexpensive electronics.

.

6 Exhaust gas analysis techniques

In the previous sections of this thesis, it was shown that information about exhaust gas can be indirectly obtained by ion sensor measurements. For example, limiting the considerations to nitric oxides (NOx) and carbon monoxide (CO), which are relevant indicators of the state of the combustion process and also toxic/pollutant compounds, it was shown that NOx concentration in the exhaust gases can be correlated with the flame temperature and, therefore, with the lambda parameter of the combustible mixture and with the flame ion density. It was also shown that for at least CO concentration a direct measurement should be desirable. Indeed, even if, in principle, a lean combustible mixture will produce a minor quantity of CO with respect to a rich one, there are situations in which this does not happen.

There exist many different techniques to analyse the composition of combustion exhaust gases. Each measurement technology can be classified in terms of accuracy, calibration requirements, cost, portability and working conditions. Obviously, each application has different constraints and there not exists the perfect gas analyser for every circumstance. Usually, the most important trade-off is between the cost of the instrument and the required accuracy of the measurement. Moreover, when an instrument for industrial applications is considered, also the environmental conditions in which the apparatus is required to operate, must be carefully taken into account. Talking about gas analysers another aspect to be considered is how often the calibration is needed. Almost all gas sensors are affected by an inevitable loss of accuracy over time caused by different factors that depend on the detection technology, and therefore a calibration procedure must be periodically performed to maintain the required accuracy. The calibration procedure requires reference gas samples, the availability of which in situ can be problematic. From this brief discussion is evident that nowadays, the challenge in the design of gas analysers is to find in the best trade-off among all these constrains, depending on the specific application.

In this section the typical composition of burner exhaust gases and the most used detection technologies in industrial gas analysers will be briefly introduced.

6.1 Exhaust gas composition

In this section a brief discussion about the principal chemical compounds present in the combustion exhaust gases is reported. The main combustion products are essentially carbon dioxide (CO_2), water (H_2O), nitrogen (N_2) and oxygen (O_2). We discussed before that the relevant presence of oxygen is mainly due to the surplus of air injected to cool the burner itself. Moreover, there are also minor components (but relevant for toxicity and pollution) in the order of part per million (ppm), which include carbon monoxide (CO), nitric oxides (NOx), sulphur oxides (SOx), particles, and unburned hydrocarbons (UHC). A table containing typical quantities of these components in gas turbine exhaust gases is shown in Figure 6.1.

NOx is mainly the sum of nitrogen dioxide (NO_2) and nitric oxide (NO). NOx originated during combustion can be divided in three classes. The first class comprises *thermal NOx*: these compounds origin from the oxidation of atmospheric N_2. Factors that influence thermal NOx formation are the high flame temperature, usually due to a low air to fuel ratio, the pressure in combustion chamber, and the persistence of air in the combustion zone. The second class is given by *prompt NOx*, i.e. oxides formed by reactions between oxygen and nitrogen intermediate combustion products. The third class comprises the so-called *Organic NOx*, that are oxides originated by the oxidation of organic components contained into the fuel. Organic NOx is usually present in less quantity than NOx.

CO is an intermediate product of combustion; in normal conditions CO rapidly oxidizes to CO_2 but, in some cases, the oxidation does not occur and a relevant quantity of CO can be measured in the exhaust gases. Conditions that facilitate CO formation are low combustion temperature, lack of oxygen or a too short combustion chamber. It is not easy to understand a priori in which conditions CO is present at high concentrations, so it necessary to measure it. In any case, a high quantity of CO is an index of a very bad combustion and of low efficiency.

UHC are, like CO, an intermediate product of combustion; also the presence of UHC is an index of an inefficient combustion. Usually, when the machine is normally running, the UHC quantity in the exhaust gas is negligible.

SOx are products of combustion that depend on the fuel composition. Usually, the presence of sulphur in fuel gives origin to SO_2 or SO_3.

The term *Particles* refers to a mix of solid particles usually composed by smoke, ash, unburned atmospheric elements, and solids that come from erosion or corrosion of turbine materials.

Major Species	**Typical Concentration (% Volume)**	**Source**
Nitrogen (N_2)	66 - 72	Inlet Air
Oxygen (O_2)	12 - 18	Inlet Air
Carbon Dioxide (CO_2)	1 - 5	Oxidation of Fuel Carbon
Water Vapor (H_2O)	1 - 5	Oxidation of Fuel Hydrogen
Minor Species Pollutants	**Typical Concentration (PPMV)**	**Source**
Nitric Oxide (NO)	20 - 220	Oxidation of Atmosphere Nitrogen
Nitrogen Dioxide (NO_2)	2 - 20	Oxidation of Fuel-Bound Organic Nitrogen
Carbon Monoxide (CO)	5 - 330	Incomplete Oxidation of Fuel Carbon
Sulfur Dioxide (SO_2)	Trace - 100	Oxidation of Fuel-Bound Organic Sulfur
Sulfur Trioxide (SO_3)	Trace - 4	Oxidation of Fuel-Bound Organic Sulfur
Unburned Hydrocarbons (UHC)	5 - 300	Incomplete Oxidation of Fuel or Intermediates
Particulate Matter Smoke	Trace - 25	Inlet Ingestion, Fuel Ash, Hot-Gas-Path Attrition, Incomplete Oxidation of Fuel or Intermediates

Figure 6.1 – Typical gas turbine exhaust gas composition (PPMV stands for part per million in volume) [33].

The most important components that can be useful indicators of the status of combustion are, as explained before, CO and NOx. The concentration of oxygen is an important parameter too; differently from internal combustion engines, as already discussed, in burner exhaust gases there is a relevant quantity of oxygen due to the air used to cool the inner burner structures. This air dilutes the exhaust gases altering the measurement of CO and NOx. For this reason, the value of CO and NOx is usually corrected to a fixed oxygen quantity according to the equation (68) in section 5.2.

6.2 Exhaust gas measurement technologies

In this section a short introduction to the most employed gas detection technologies is reported, highlighting pros and cons.

6.2.1 Chemiluminescence

Chemiluminescence effect [34] is the emission of light as a consequence of a chemical reaction. It is a phenomenon usually used for the measurement of nitric oxide exploiting the chemical reaction between NO and ozone (O_3):

$$NO + O_3 \Rightarrow NO_2^* + O_2 \Rightarrow NO_2 + O_2 + h\nu \qquad (70)$$

which, by the intermediate excited product NO_2^*, brings to the emission of a photon with energy $h\nu$ that can be detected using a photodiode. The ozone necessary for this reaction can be stored in a tank or also produced from the atmospheric oxygen by an ozone generator. This reaction is possible only in presence of NO and it cannot take place in presence of NO_2. To measure NO_2 together with NO, chemiluminescence analysers also includes a NOx converter which is a device that transforms the NO_2 in NO, allowing the measurement of total NOx. The main advantage of this technique is the very good accuracy (less than 1ppm), the good selectivity and the fast response time. The main problem comes from the needs of the NOx converter and of the ozone generator: these devices increase the cost and decrease the reliability of the instrument.

6.2.2 Optical detectors

These sensors exploit the measurement of the absorbance spectrum of a gas mixture to detect the presence of a target element. The absorbance (A) is defined by the *Beer-Lambert law* that describes how the light is attenuated travelling through a material for a given optical path (the following

expression holds for a single attenuating species of uniform concentration within the optical path) [34].

$$A = \epsilon\, l\, c \tag{71}$$

Where $\boldsymbol{A}$ is the absorbance [*dimensionless*], $\boldsymbol{l}$ is the length of the path [*m*], $\boldsymbol{\varepsilon}$ is the molar attenuation coefficient [m^2/mol], and $\boldsymbol{c}$ is the concentration of the attenuating species [$mol/\ m^3$]. In practice, the value of the absorbance can be calculated using an alternative definition:

$$T = \frac{\Phi_e^t}{\Phi_e^i} = 10^A \tag{72}$$

Where $\boldsymbol{T}$ is the transmittance of the material sample [*dimensionless*], Φ_e^i is the radiant flux [*watt*] incident on the sample and Φ_e^t is the radiant flux transmitted through the sample [*watt*]. Measuring the transmitted power, and knowing the incident power, it is possible from equation (72) to derive the absorbance and, using equation (71) it is possible to derive the concentration of the target species. The sensors which exploit this phenomenon are provided with two identical optical paths for the light, one (reference channel) that does not contain the attenuating species, and the other one containing the attenuating species (measurement channel). The first one is used to measure (with a pyroelectric or a thermopile detector) Φ_e^i, the second one to measure Φ_e^t. The target species usually have a verry narrow absorbance peak at a given wavelength. Usually, a large bandwidth source is used in this kind of sensors, and the detector is calibrated, exploiting optical filters, at the absorbance peak wavelength. These sensors can have optical source and detector in the infrared spectrum (IR sensors) or in the ultraviolet spectrum (UV sensors), depending on the target species.

Optical detectors-based gas analysers are very accurate (accuracy < 1 ppm), fast, and selective, but they are usually very expensive. To achieve a very good accuracy, the optical parts need to be very precisely mounted and calibrated. A small displacement in the sensor structure may affect the calibration.

6.2.3 Paramagnetic detectors

Paramagnetic detectors, exploiting the paramagnetic propriety of oxygen, are used to monitor the oxygen concentration in a mixture of gases. Paramagnetic materials have a small, positive susceptibility to magnetic fields. These materials are slightly attracted by magnetic fields, but do not retain the magnetic properties when the external field is removed. In a typical exhaust gases mixture, the only paramagnetic component is oxygen. There are two main paramagnetic technologies for oxygen detection: the *paramagnetic* technology and the *thermoparamagnetic* one. In both of them the movement of oxygen due to a magnetic field is exploited. In the thermoparamagnetic technology oxygen movement is detected using 4 thermistors, two are power supplied and used to heat the gas, the other two are used to sense the "wind" caused by the oxygen molecules that move due to the paramagnetic effect. These thermistors are arranged in a Wheatstone bridge allowing to measure the wind effect. In the paramagnetic technology, the movement of oxygen creates a gradient in the density of the sample gas in a chamber, that can be detected measuring the displacement of a floating sphere. The paramagnetic technology is currently used to detect oxygen in many analysers with a good accuracy. However, the presence of precise mechanical parts makes the detector very cumbersome, delicate, and expensive.

6.2.4 Electrochemical gas sensors

Electrochemical sensors, or electrochemical cells, can be divided in two principal classes: *voltammetric* cells and *amperometric* cells. The main difference between these classes is the output signal that in one case is a voltage (voltammetric cells), and in the other case is a current (amperometric cells). The most used sensors for gas detection are the amperometric cells, in which the potential is kept constant and the current is measured. The electrochemical sensors consist in general of two, three or more electrodes, of an ionic conductor called electrolyte[14] and of a gas membrane. The electrodes are porous conductive structures that allow gas compounds to pass through. The current

[14] The electrolyte can be a liquid solution or a polymer. In commercial sensors polymers, e. g. Nafion, are usually preferred.

that is generated by the sensor is amplified and acquired by specific front-end electronics that also guarantees the correct biasing of the sensor.

A drawing of an electrochemical sensor is shown in Figure 6.2: the gas enters the sensor through the gas membrane, which limits the gas flow to avoid the sensor saturation. The gas diffuses through the membrane and reaches the working electrode (WE) where a chemical reaction occurs. This reaction can be either an oxidation (loss of electrons), or a reduction (gain of electrons) reaction, depending on the target gas.

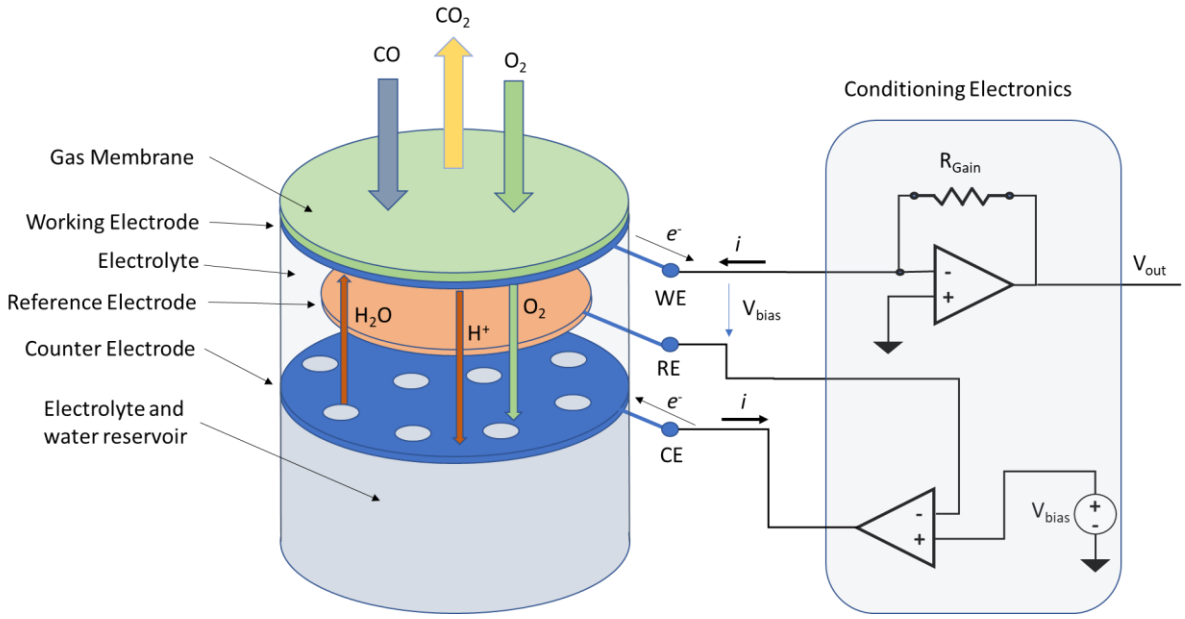

Figure 6.2 – Electrochemical sensor structure with external conditioning electronics.

If an oxidation reaction occurs at the *WE*, the complimentary reaction (reduction) occurs at the counter electrode (*CE*) an vice versa. For example, as shown in Figure 6.2, in the case of a CO sensor, an oxidation reaction occurs at the WE:

$$CO + H_2O \Rightarrow CO_2 + 2H^+ + 2e^- \qquad (73)$$

At the CE, we have a reduction:

$$\frac{1}{2}\,O_2 + 2H^+ + 2e^- \;\Rightarrow\; H_2O \qquad (74)$$

Considering the total balance of the reactions (73) and (74), there is a consumption of oxygen, so these sensors cannot operate in environments without O_2 (a few ppm of oxygen are usually required). Electrochemical sensors host frequently a reservoir where water is accumulated in case of temporary operation in extremely dry environments. In fact, even if water is not consumed in the reactions, a very low partial pressure of water outside the sensor can dry it. For this reason, these electrochemical sensors cannot operate for long periods at relative humidity <10%. Due to the reactions (73) and (74), the electrical positive charges travel through the electrolyte (H^+ ions) toward the CE, whereas electrons flow to the CE through the external circuitry. Effectively, the sensor generates a current flowing through the external circuitry from the CE to the WE, (amperometric sensor). The current generated by these chemical reactions is a function of the gas concentration, with a relationship that can be very complex. As shown in Figure 6.2, the sensor is equipped with a membrane that limits the flow of gas that can enter inside the sensor to a rate $\mathbf{r_d}$. Supposing that the reaction at the electrode interface has a rate $\mathbf{r_r}$ we can have two different situations named limiting current conditions [35]. In the first condition, the diffusion through the membrane is faster than the reaction rate ($r_r << r_d$) and the overall rate of the process is limited by the reaction rate. Considering a redox reaction in the form of (75):

$$O + ne^- \;\underset{K_O}{\overset{K_R}{\rightleftharpoons}}\; R \qquad (75)$$

the generated current can be described by the Butler–Volmer equation [36]:

$$i = nFA\left(K_R\, C_{R,rp} e^{-\frac{\alpha_R nF\eta}{RT}} - K_O C_{O,rp} e^{-\frac{\alpha_O nF\eta}{RT}}\right) \qquad (76)$$

where $\boldsymbol{K_R}$ and $\boldsymbol{K_O}$ represent the reaction rate constants in case of oxidizing or reducing species, $\boldsymbol{F}$ is the faraday constant [$(A\,s)/mol$], $\boldsymbol{A}$ is the electrode area [m^2], $\boldsymbol{R}$ is the universal gas constant [$J/(mol$

K] , $\boldsymbol{T}$ is the absolute temperature [*K*], $\boldsymbol{C_{R,tp}}$ and $\boldsymbol{C_{O,tp}}$ are the concentration of oxidizing or reducing species at the reaction plane [mol/m^2] (we can suppose that they are equal to the gas concentration since the membrane diffusion process is fast), $\boldsymbol{n}$ represents the number of reacting electrons per molecule, $\boldsymbol{\eta}$ is the activation overpotential, $\boldsymbol{\alpha_R}$ and $\boldsymbol{\alpha_O}$ are the transfer coefficient ($\alpha_R + \alpha_O = 1$). In this case the current is proportional to the gas concentration but there is an exponential dependence on temperature and η, which can be attenuated maintaining the potential η as close as possible to 0. Using this strategy, a quasi-linear relationship between current $\boldsymbol{i}$ and $\boldsymbol{\eta}$ can be obtained as show in Figure 6.3.

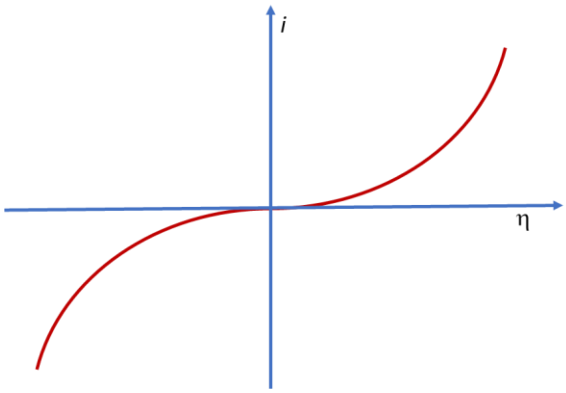

Figure 6.3 – Qualitative plot of the Butler-Volmer equation.

Usually, amperometric sensors operate in the second limiting condition where the membrane diffusion rate is smaller than the reaction rate ($r_r >> r_d$). The diffusion rate is described by the *Fick's diffusion law* and the limiting current is now determined by the rate at which the gas reaches the electrode surface ($\boldsymbol{K_D}$), where it reacts immediately. Supposing to have a $\boldsymbol{\eta = 0}$[15] and defining ($\boldsymbol{C_{Gas}}$) the gas concentration over the membrane [mol/m^2], the current is usually written as [36] :

[15] To obtain this condition, sensors can be provided with a third electrode called *reference electrode* (*RE*) in which no current flows. Since in RE does not flow any current it can be considered at the same potential of the electrolyte. The driving voltage (V_{bias} in Figure 6.2) is applied between WE and RE)

$$i = nFAK_D C_{Gas} \tag{77}$$

This last case is preferred because, as discussed, the exponential dependence on temperature is in principle cancelled.

The discussed behaviour can be described by the lumped parameters electric model in Figure 6.4 [37].

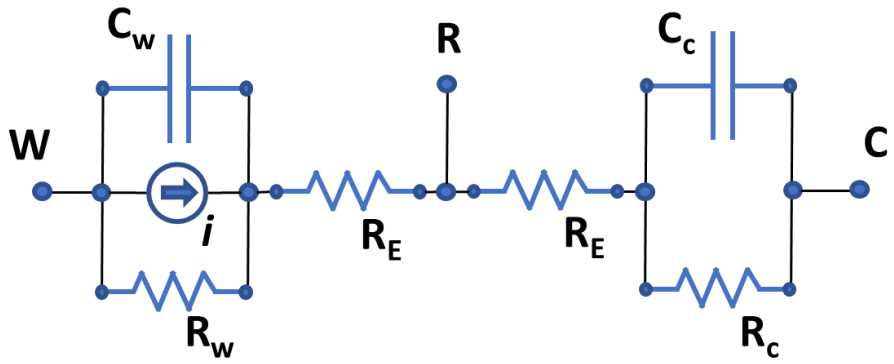

Figure 6.4 – Electric model for an amperometric electrochemical sensor.

C_w and the C_C are the working and counter electrode double-layer capacitances, respectively. The resistances R_w and R_C represent the charge transfer resistances between the electrolyte and the electrodes. R_E represents the electrolyte resistance. The reference electrode is assumed to be at the electrolyte potential and no current is flowing across it. The resistance of the electrolyte is usually negligible, whereas the charge transfer resistances can assume values from 1 $k\Omega$ up to 100 $k\Omega$ [38]. The electrode capacitances, due to the double layer effect, can assume relatively high values. Typical values are some hundreds of mF. Due to this very high value, a small potential variation of the electrode potential, can be converted in a very high current flowing through the electrode. For this reason, a very stable and low noise conditioning electronics is required for this application. Some electrochemical sensors are provided with a fourth electrode called Auxiliary electrode (AE). The

AE can be considered equivalent to the WE in terms of electrochemical reactions, but its area is a fraction α_s of the WE area, with $\alpha_s < 1$, and it is not exposed to the gas. AE is used to correct the zero current, that means the current flowing in the WE in absence of gas. This current, except for the area scale factor, is assumed to be the same both for WE and AE, and can be used to correct the current at WE according to the following relationship:

$$i_{W\,Corrected} = i_W - \frac{i_A}{\alpha_s} \qquad (78)$$

Where i_W and i_A are the working electrode and the auxiliary electrode current, respectively.

Electrochemical sensors have usually a limited cost, are available for almost all gases of interest in combustion and are produced by many suppliers. The main drawback of electrochemical sensors is the limited lifetime, usually of 2/3 years, which implies a periodical sensor substitution. Another practical issue is that an exposition to extra-range gas concentration or working with extreme environmental conditions (in terms of temperature and humidity) can damage or poisoning these sensors.

6.2.5 Gas measurement techniques performance comparison

In the following table it is reported a synthetic comparison, for the application of interest, of electrochemical sensors and optical sensors (included chemiluminescence sensors) in terms of performances. It is important to remark that an electrochemical gas analyser is based on limited lifetime replaceable sensors, whereas optical analyser sensors are long life (usually instrument lifetime) sensors. Optical technologies offer a better accuracy and selectivity but requires frequent calibrations (mainly due to the delicate mechanical mounting of the source and the detector). Electrochemical sensors are less accurate and selective, but they are characterized by a lower drift over time that allows to significantly increase the calibration intervals. Moreover, electrochemical sensor can be easily calibrated in a laboratory environment and delivered on the site where they can be mounted on the analyser.

Characteristic	Electrochemical	Optical-chemiluminescence
Cost (per instrument)	low (<5k€)	high (>20k€)
Lifetime (per sensor)	Reduced, sensors must be periodically replaced (1-2 years)	Instrument lifetime (many years)
Average accuracy	2-4 ppm	< 1ppm
Selectivity	good	excellent
Response Time	tens of seconds	some seconds
Typical drift (sensitivity % variation)	some % per months	some % per week
Portability	Sensors can be pre calibrated and eventually replaced on the site.	Calibration required on the site.

Table 5 – Gas sensor technologies performances comparison

7 Architecture of the developed gas analyser

On the bases of what discussed in the previous sections, one of the aims of this thesis was to develop portable fume analyzer for the detection of CO, NO, NO_2 and O_2 which did not require an external fume pre-treatment unit (i.e. which was equipped with a cooling / dehumidification system for the gases to be analyzed), did not require complex and frequent calibration procedures, and that at the same time had performances in terms of accuracy and response / recovery times and stability suitable for an online monitoring activity. With regard to the latter aspects, the commercial instruments mentioned, based on optical/chemiluminescenc sensors, must be considered as reference values that are justified in a context of certification of the performance of the machine, but which may be partially relax in a monitoring context. This aspect has allowed the use of electrochemical sensors, which are adequate to the specifications in terms of accuracy, stability and response / recovery times when subjected to target gas concentrations in the operating ranges provided by the manufacturer. The problem of avoiding exposure to too high concentrations of target gases, increasing in this way the sensor recovery time, has been solved, as it will be discussed in what follows, at the system level.

Hereafter the main constrains considered for the design are summarized:

- Use of standard commercial low-cost gas sensors.
- Measurement accuracy for CO and NOx concentrations lower than 50ppm better than ±4ppm, and for O_2 better than 1%.
- Sensor response/recovery time ≤ 1 minute.
- Simplified sensor calibration procedures, avoiding the use of calibration cylinders on site .
- Presence of an internal gas treatment unit.

The designed prototype contains all the elements necessary for the sampling and the conditioning of exhaust gases. The instrument contains a chiller that allows the cooling and dehumidification of the gases, and filtering systems for the elimination of particulate matters. The analyser is based on

electrochemical sensors, mounted on specific printed circuit board sensor modules that can be installed individually in the instrument. The sensor modules are pre-calibrated and can be installed/substituted on the need directly in site. The instrument also provides a protection system to prevent the sensors from being exposed to gas concentrations above the safe range (especially for CO sensors), which can be present in different working conditions of the combustors (e.g. during the starting phase). This last feature is particularly relevant: as previously discussed, if the electrochemical cells enter in contact with a mixture containing concentrations of the target gases much higher than the sensors full scale, they can be damaged, and in any case a recovery transient is triggered making the sensors unusable for long periods (up to several hours). To avoid this problem, the instrument is provided with two measurement chambers, one for high concentration measurements (sensors with large measurement ranges) and one for low gas concentration measurements (reduced measurement range sensors). The low gas concentration chamber is used only in case of gas concentrations lower than predetermined thresholds. The system automatically controls this protection system as well as the gas conditioning system [39].

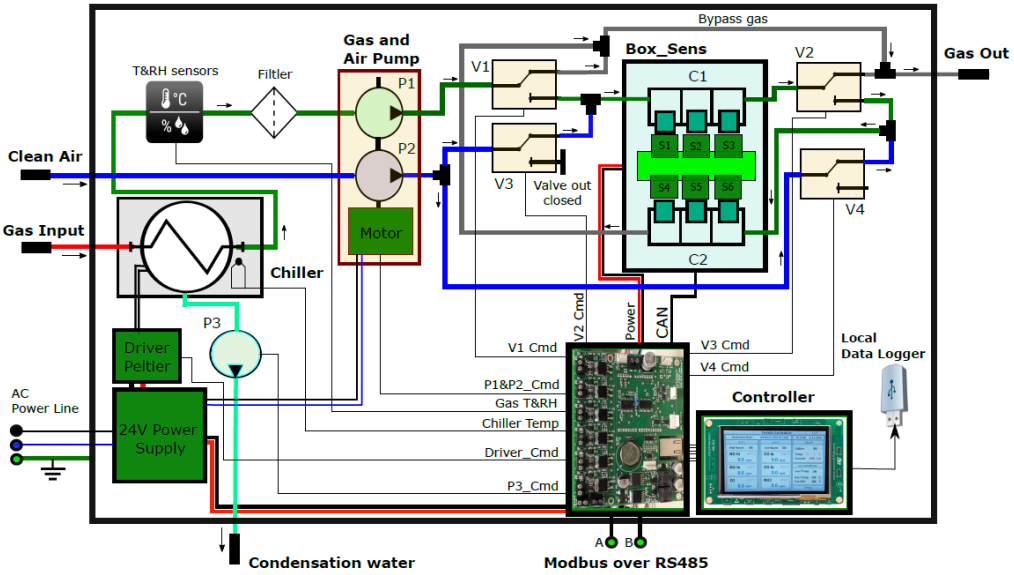

Figure 7.1 – Functional block diagram of the developed instrument.

The heart of the instrument is a controller that manages all its functionalities. The controller is accessible locally via a touch screen display, or remotely by a serial RS485 interface and a Modbus® protocol. In Figure 7.1, the functional block diagram of the developed instrument is shown.

In the following the main sections of the instrument will be described and discussed. In Figure 7.2, it is shown a picture of the internal structure of the instrument in which the main sections are highlighted.

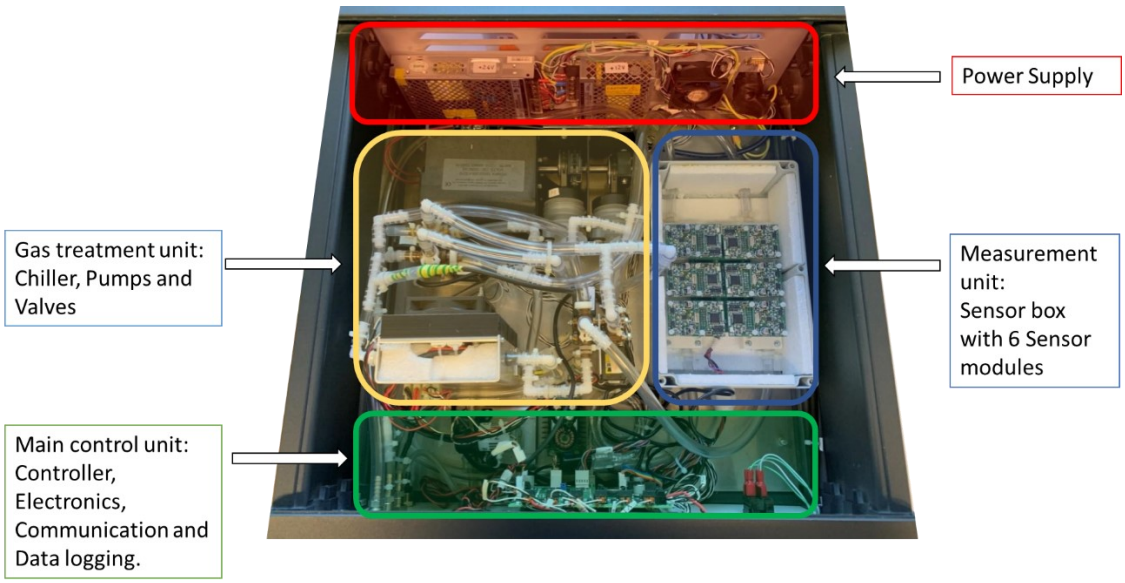

Figure 7.2 – A picture of the instrument internal structure with the main sections highlighted.

7.1 Gas treatment unit

The exhaust gases contain a relevant quantity of water (from 1 to 5% in volume) and they usually have a very high temperature. When the gases are cooled, the relative humidity reaches the saturation level and water starts to condense. For this reason, the pipeline used to sample gases from the chimney and to bring them to the analyser is usually thermally insulated or also heated. The presence of a liquid fraction in the exhaust gases can damage the sensors and/or alter the measurements, therefore the exhaust gases must be dehumidified before being analysed. The

dehumidification unit of the instrument, the so called "chiller", is a thermoelectric gas cooler, in which the exhaust gases are brought to 4 °C (this temperature is adjustable) to remove most of the water fraction. The chiller exploits two Peltier cells, a custom designed aluminium body positioned on the cold side and a heater exchanger and a fan on the hot side. The condense of water is collected by the bottom of the chiller body, in a specific cavity which is periodically emptied by a peristaltic pump. In Figure 7.3, the structure and the final design of the chiller are shown.

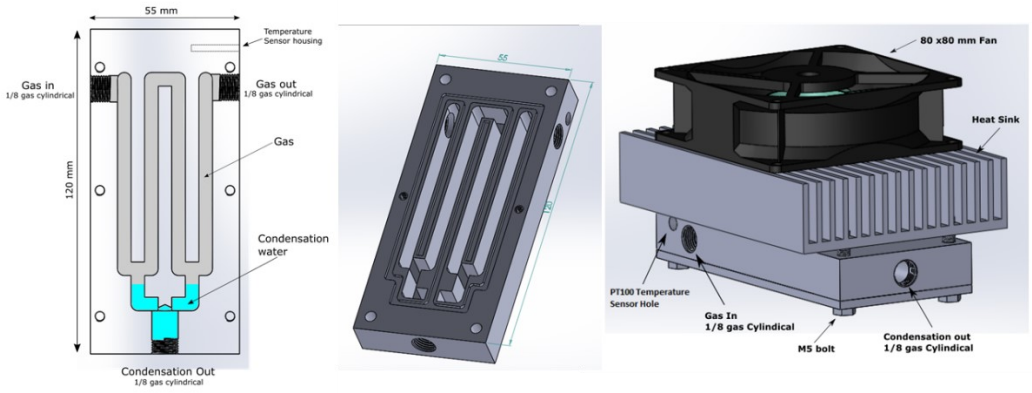

Figure 7.3 – Chiller structure, from left to right: The cross section, a 3d image of the inner part and the final configuration.

The chiller was tested in different conditions: in Figure 7.4 it is shown, as an example, one of the tests in which the chiller was fed by a 300 mL/minute, 100% RH, 70°C air flow. The output air flow was monitored in terms of temperature and humidity content after a 20 cm plastic pipe (that allowed gases to return to room temperature). As it can be seen, when the chiller is working, the relative humidity of the output air is < 40% whereas when it is turned off is > 90% allowing water, in contact with colder parts, to condense. The average power consumption of this device is around 30 W at room temperature (25°C). The heater exchanger was designed to allow an operation of the cooler up to a room temperature of 40 °C.

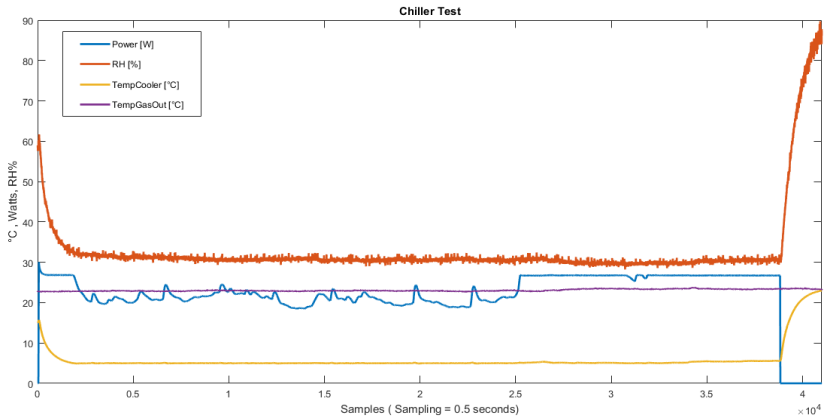

Figure 7.4 – Example of chiller test.

7.2 Measurement unit

As it can be seen from the diagram in Figure 7.1, a set of two volumetric pumps (one used to draw exhaust gases inside the instrument (green pipeline), and the other one used to pump 'clean' air (blue pipeline)) and of four electrically actuated valves is used to properly feed two measurement chambers. The two measurement chambers, each one hosting 3 sensors, are the hearth of the instrument. Each sensor is mounted on a dedicated electronics front-end module, based on a microcontroller, which manages the correct sensor biasing and performs the sensor data analog to digital conversion. The front-end modules, hosted on a motherboard, communicate via a CAN bus with the main controller unit. The instrument parts here introduced are described in detail in the following subsections.

7.2.1 Sensor modules

The sensor module block diagram is show in Figure 7.5. The microcontroller is the STM32F373, that is equipped with 3 16-bit sigma-delta analog to digital converters (ADC) and 3 12-bit digital to analog converters (DAC).

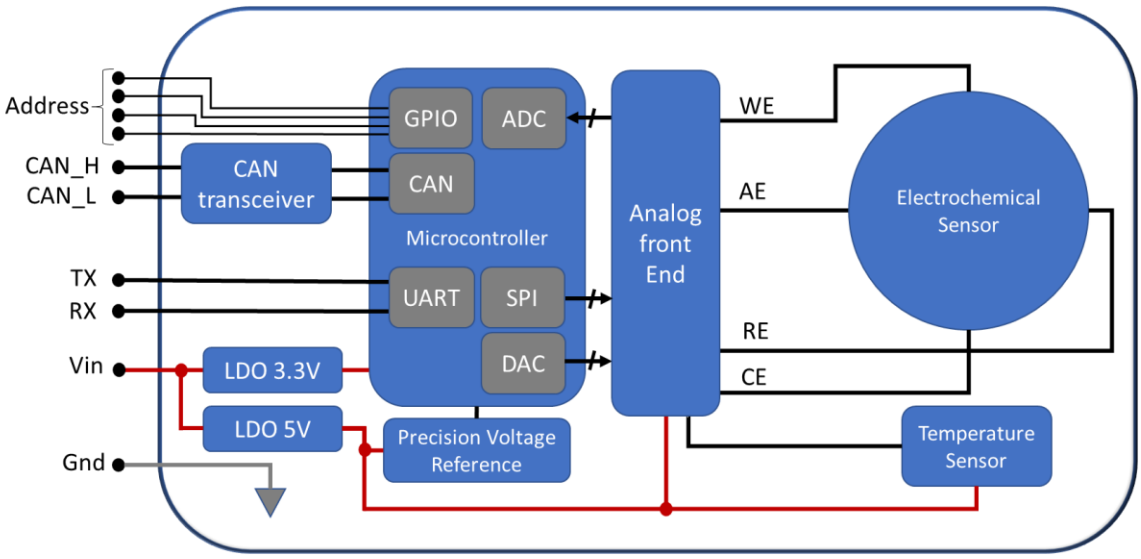

Figure 7.5 – Sensor module internal structure.

The sigma delta-ADCs are used to acquire the signals of the working electrode (WE), of the auxiliary electrode (AE) and of a temperature sensor mounted close to the electrochemical cell. The DACs are used for the sensor biasing. In Figure 7.6 the implemented sensor analog front end electronics is shown. The schematic for the electronic front end was already shown in Figure 6.2, but the actual implementation needs some additional comments. To allow for a single supply operation, a DAC output (Voltage generators DAC_1 in Figure 7.6) is used to set the ground potential (V_{Gnd}) to half the supply voltage (5V). DAC_2 output is instead used to set the bias voltage of the sensor (V_{bias}). The ADCs and the DACs share the same precision reference voltage (3V).

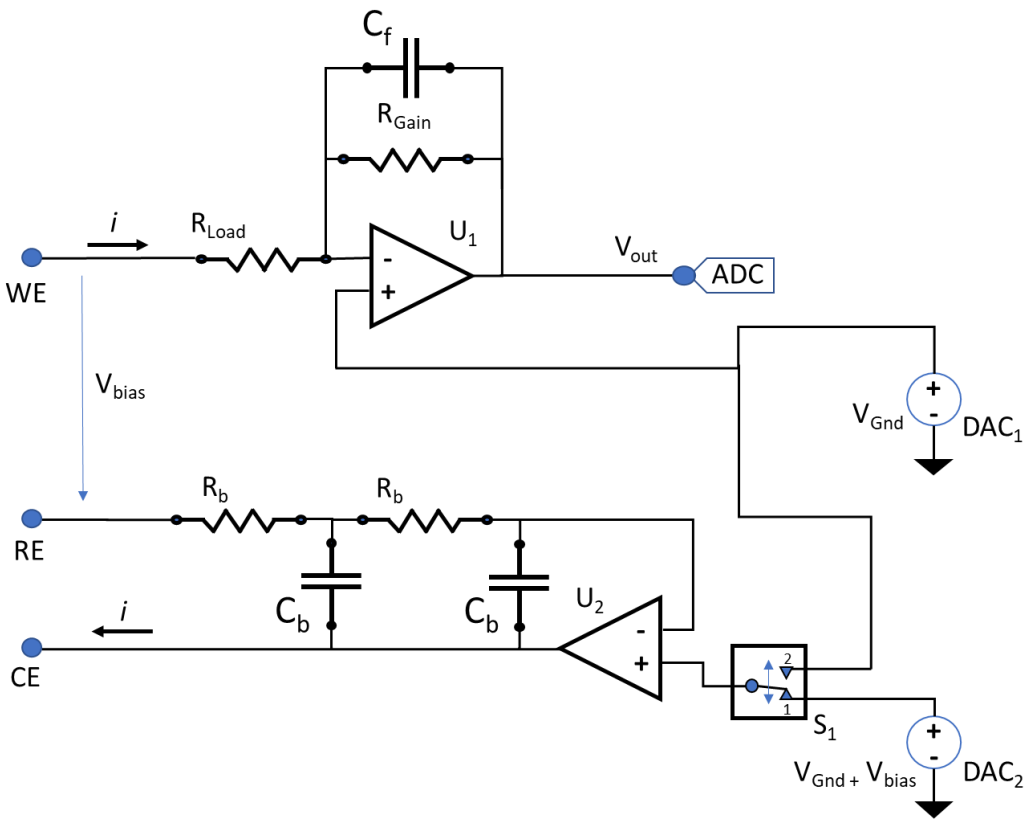

Figure 7.6 – Analog front end schematic.

The current to voltage converter connected to the WE, implemented using a standard topology, is based on the operational amplifier OPAx192, which was selected for its low input bias current (a few pA). The output voltage proportional to the sensor current can be written as:

$$V_{out} = \frac{R_{Gain}}{1 + j\omega\, C_f\, R_{Gain}} \cdot i \qquad (79)$$

The implemented electronic exploits for R_{Gain}, in place of a fixed resistor, a digital potentiometer controlled by an SPI bus, which allows to dynamically adjust the gain of the electronic front end on the bases of the sensor characteristics. In this way the sensor module can be used with different electrochemical sensors without hardware modifications. This stage introduces a low pass filtering effect used to limit the bandwidth of the signal, avoiding potential aliasing problems during the analog to digital conversion. The cut off frequency f_p is given by:

$$f_p = \frac{1}{2\pi\ C_f\ R_{Gain}} \tag{80}$$

The R_{Load} resistor is used to reduce the effect of voltage noise due to fluctuations of the WE electrode, which are amplified by this stage by a factor (A_{noise}):

$$A_{noise} = -\frac{R_{Gain}}{R_{Load}} \tag{81}$$

The R_{Load} resistor value is selected as a trade-off between noise reduction (large R_{Load}) and sensor response time (small R_{Load}), indeed, if R_{Load} increases, the equivalent time constant of the sensor increases. Moreover, the larger R_{Load}, for a given current *i* the larger are fluctuations of the WE biasing. The values of R_{Load} are in the range of [0 Ω,47 Ω].

R_b and C_b are used to implement a low pass filter that reduces the noise from the reference electrode increasing the stability of the bias loop, as it is discussed in what follows. The voltage difference between DAC_1 and DAC_2 (V_{bias}) corresponds, neglecting R_{Load}, to the voltage between RE and WE. As explained in section 6.2.4, the electrode interface may introduce a significant capacitance effect, therefore voltage fluctuations of V_{bias} may introduce significant fluctuations in the measured current: indeed, referring to Figure 6.4, and neglecting the effect of the electrolyte resistance R_E and of R_{Load}, V_{bias} is the voltage across C_w, and the current flowing in C_w is given by:

$$i_{Cw}(t) = C\frac{d\ V_{bias}(t)}{dt} \tag{82}$$

From equation (82), and considering that C_w is in the order of some tens of mF [38], it is evident that also small fluctuations of V_{bias} can generate current contributions comparable with the electrochemical sensor typical operating current (some μA). As a final comment, in case of zero-

biasing it is preferable to electrically connect (by the analog switch S_1) the non-inverting inputs of the operational amplifiers U1 and U2 (OPA2192), using only one DAC to set the ground voltage.

Two different low drop linear regulators (LDO) were used to supply the sensor module: a 5V regulator (LP2992-5.0) for the analog reference of the microcontroller and the front-end electronics, and a 3.3V regulator (LP2992-3.3) for the microcontroller and the CAN communication interface, both with a dedicated filtering based on low ESR electrolytic and ceramic capacitors.

The communication section of the module comprises an asynchronous serial (UART) interface and a CAN bus interface (MAX3051). The CAN bus interface was used to have all the modules connected via a single daisy-chain bus. Moreover, CAN bus guarantees a high immunity to noise and a reliable data delivery. Each sensor module is mounted on a motherboard that can host up to 6 modules, 3 for the first measurement chamber and 3 for the second one. The sensor modules can be programmed by the serial interface from a PC software tool (a specific communication protocol was implemented), to permanently store the characteristics of the sensor and the calibration parameters. The modules use this set of parameters to convert the acquired current into a gas concentration and properly set the bias voltage of the sensor. A picture of the sensor module is shown in Figure 7.7. The module exploits a 4-layers PCB with the internal layers dedicated to the ground plane and the analog supplies, respectively.

The modules use 4 pins to sense the state of 4 contacts on the motherboard (*Address pins* in Figure 7.5) to detect the position in which they are mounted (from 1 to 6) and assume the correspondent CAN bus address. At the start-up, the main control unit reads from each module, at the address corresponding to the position on the motherboard, the information relative to the characteristics of the sensor present in each module. Exploiting this strategy, the main controller can know the type and the position of the different sensors.

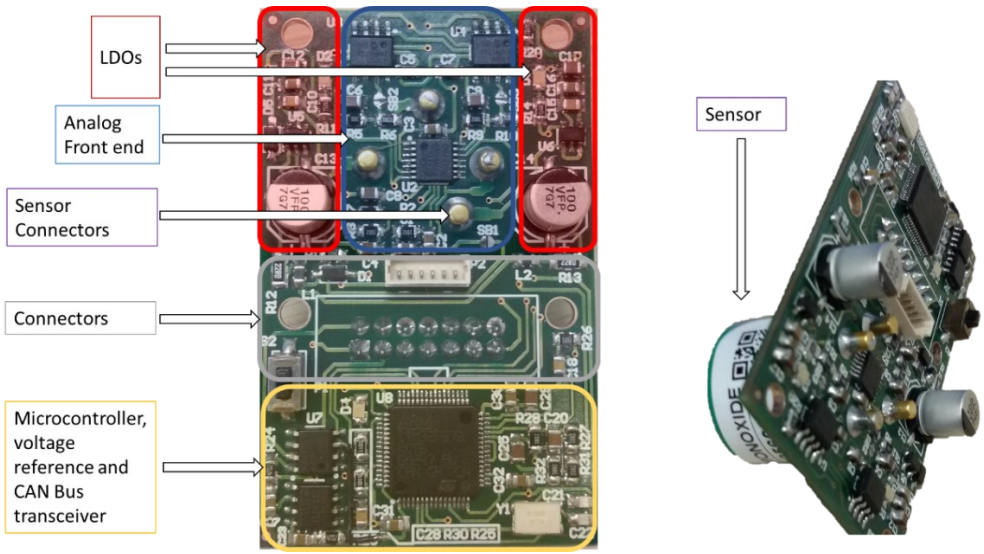

Figure 7.7 – A picture of the sensor module (45mm x 23mm).

7.2.2 Measurement chambers

As previously introduced, the sensors are hosted in two measurement chambers (Figure 7.8). A valve and pump system allows to set three different working conditions: *No Protection Status, Main Protection Status* and *Secondary Protection Status*, respectively. During normal operation (No Protection Status) the valves allow the gas flowing through chamber #1 and then through chamber #2. The external air flow is not used and goes directly to the exhaust output. In the *Main Protection Status*, air is injected in both the chambers whereas the exhaust gases do not cross the chambers and reach the exit directly. In the *Secondary Protection Status,* the valves divert the gas flow from chamber #2, where the air flow is injected to remove any trace of exhaust gases. In this condition, the exhaust gases only pass through chamber #1. In summary, the instrument is capable of injecting exhaust gases into both chambers, in chamber #1 only, or in none of them; when diverted, the flow of

exhaust gases is replaced by an air flow. The valve system is controlled by the main control unit, described in the next section.

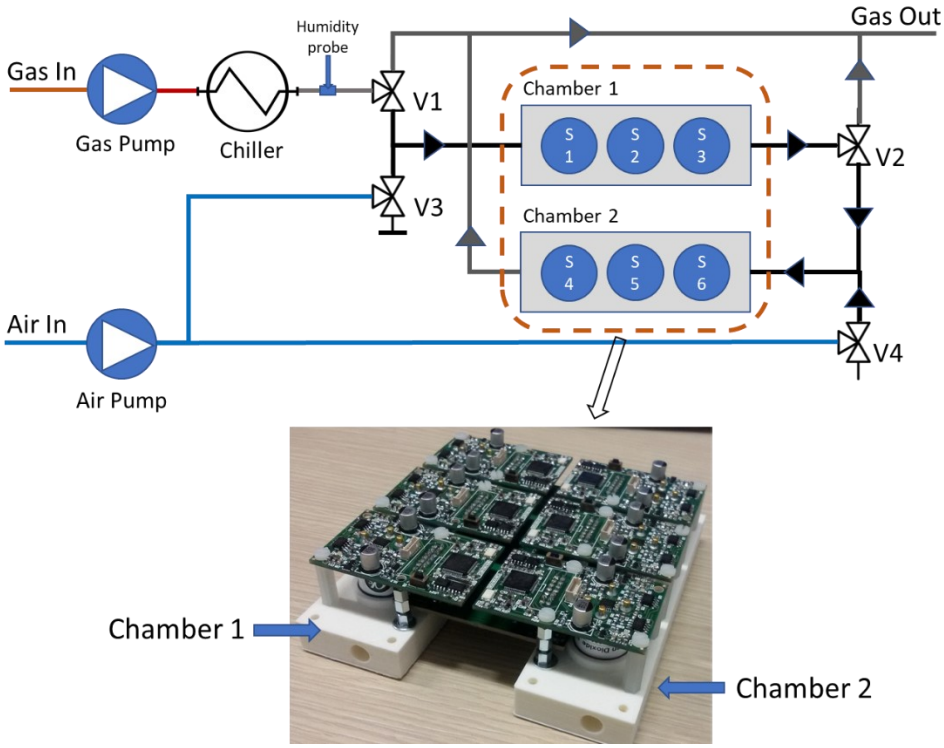

Figure 7.8 – Measurement chambers and piping diagram.

7.3 Main control unit

The main control unit is based on an evaluation board from ST Microelectronics (STM32F7-Discovery) that embeds a high-performance microcontroller and a touch screen display. A custom expansion board was developed to interface and control all the subsystems of the instrument, as well as to collect, save and display the data from the sensor modules (Figure 7.9). In detail, it controls the pumps, the state of the valves, the chiller temperature. The chiller temperature is set by a feedback loop based on a PI controller and a PT100 temperature sensor. The cooling power is modulated using a current driver that supplies the thermoelectric elements of the chiller. The

main controller communicates with the sensor modules by an RS-485 serial interface and a Modbus® protocol: the gas concentration data are shown on the local display (Figure 7.9), if required they can be saved in csv format on an usb key, and are used, together with the data from a humidity sensor placed after the chiller, to set one of the three working conditions (*No Protection, Main Protection and Secondary Protection Status*).

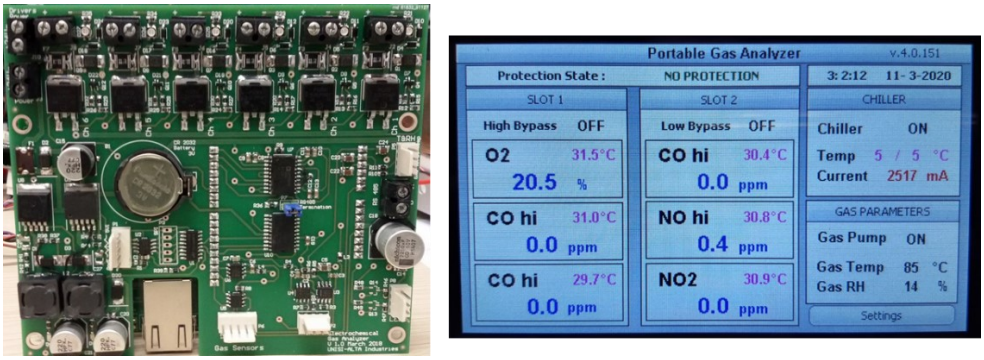

Figure 7.9 – A picture of the main controller unit board (left) and of the front panel touch screen interface (right).

With reference to this last point, as previously explained, each sensor module is identified on the CAN bus with a specific address that allows to identify in which measurement chamber the module is mounted. Reading the configuration parameters, the microcontroller knows also which is the target gas of each sensor module. Exploiting this information, it is possible to implement the protection of the sensors in chamber #2 (protected sensors) from poisoning. In detail, if two sensors for the same target gas, for example CO, are present in the two chambers, the sensor in chamber #1, with a wider measurement range and a lower accuracy than the sensor in chamber #2, is used to detect if the gas concentrations is above a predefined threshold (T1) and if it is therefore necessary to protect the sensor in chamber #2 (protected sensor). If threshold T1 is exceeded, the Secondary Protection Status is activated, and the exhaust gases do not reach chamber #2. This procedure is effective thanks to the delay with which the gas flow reaches chamber #2, due to the pipeline that interconnects the two chambers. The protection is removed when the gas concentration in chamber #1 drops below a second predefined threshold (T2<T1). The difference between the two threshold values is set on the basis of the sensor response time and the pipeline length. The threshold values are stored in the sensor modules and are read by the main controller

at the start-up. The benefit of these technique is to significantly reduce the recovery time of the sensors after a high target gas concentration event, which usually occurs, e.g., when the burner is started up.

The relative humidity of the cooled gases after the chiller is monitored to check if it is in the range 20% - 80%. If this condition is not satisfied, the *Main Protection Status* is activated diverting the gas flow from the two chambers. This operating mode is useful to avoid that the electrochemical sensors work in conditions of a too low humidity (many electrochemical reactions require water to take place), or to avoid the risk of water condensation in case of too high relative humidity (for example during the chiller start up or in the event of a cooling system failure). The RH value is continuously monitored by the instrument and shown in the front panel touch screen display.

Each protection status can be also manually forced from the Modbus® interface or by the touch screen panel.

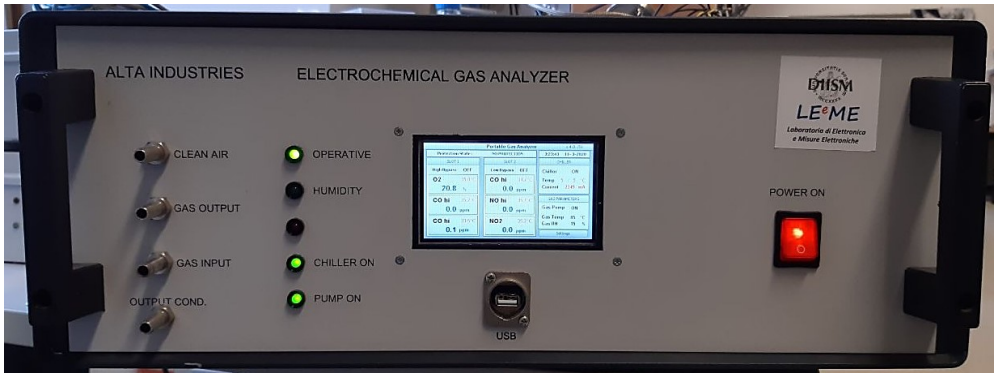

Figure 7.10 - Instrument front panel containing inlet and outlet terminals for gases (left), touch panel (centre), power switch (right) and usb port (bottom).

8 Gas analyser Tests

In this section the results of a test campaign performed with the developed gas analyser are reported. The tests have been performed both in laboratory environment and in a real application scenario. The aim was both to evaluate the correct behaviour of the instrument and to test the accuracy and the durability of electrochemical sensors for exhaust gas measurements. The sensors, mounted on the designed electronic modules, were individually calibrated using reference gas tanks and the characterization system described in [40], in which gas mixtures with controlled concentrations of different elements can be sent to the measurement chamber.

8.1 Sensor protection test

The main peculiarity of the instrument is the protection system to avoid electrochemical sensors poisoning due to high gas concentration exposition. The most critical sensors are those used to detect carbon monoxide, the concentration of which can span over a very large interval, especially immediately after the burner ignition. The most relevant issue is the high recovery time of the sensors: after the exposition to a very high gas concentration an electrochemical sensor, due to the diffusion membrane and the charge accumulation in the double capacitances, requires a very long time (from minutes up to hours depending on the reached concentration) to reduce its current. This effect makes the sensor unavailable for a long time, which is not acceptable for the considered application. Several tests were performed to verify the correct behaviour of the instrument from this standpoint. Hereafter only two examples are reported, one relative to a test performed at the test bench described in section 4 (Figure 8.1), and the second (Figure 8.2) relative to measurements carried on in a BH test rig (see section 8.2).

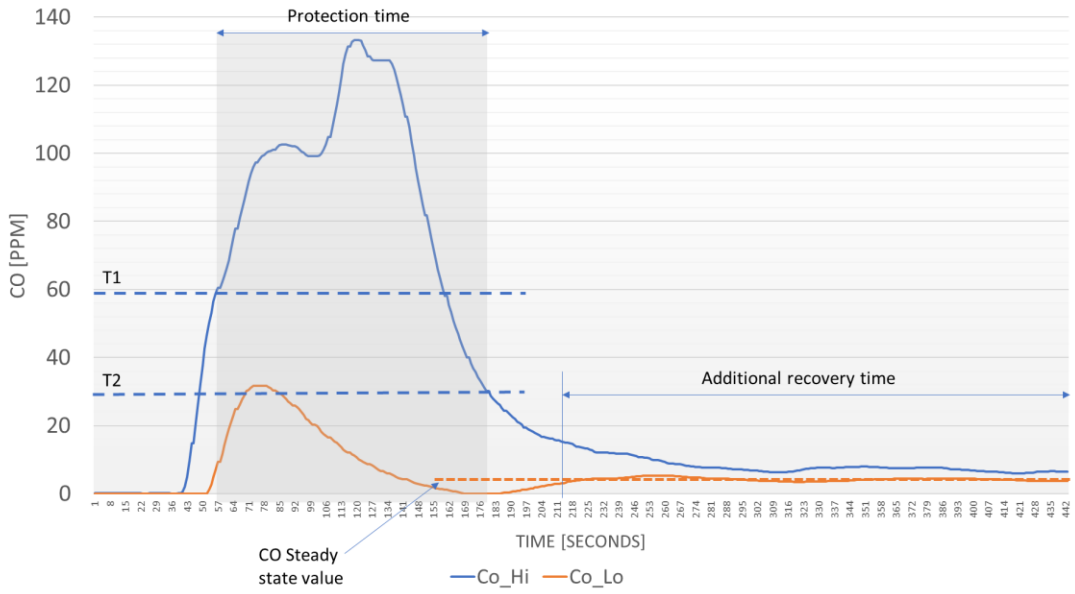

Figure 8.1 – Start-up carbon monoxide concentration transient measured by the protected sensor (Co_Lo) and by the protection sensor (Co_Hi). T1 and T2 are the threshold vales used to activate the proper working condition.

In Figure 8.2 an example of CO measurement during a real gas turbine start-up transient is shown. In this test the same Alphasense CO sensor was used for the Co_Hi (chamber #1) and the Co_Lo (chamber #2) sensors but, to avoid saturation at the high CO concentrations, the gain of the electronics front end for the CO_Hi sensor was reduced. This causes a noisier signal for the CO_Hi sensor (this problem can be overcome using different sensors in the two chambers, suitable for different measurement ranges). In Figure 8.2 the CO Mixed data signal represents the fusion of the two CO sensors output: when the protection is activated the CO concentration is derived from the CO_Hi sensor, otherwise it is given by the CO_Lo sensor.

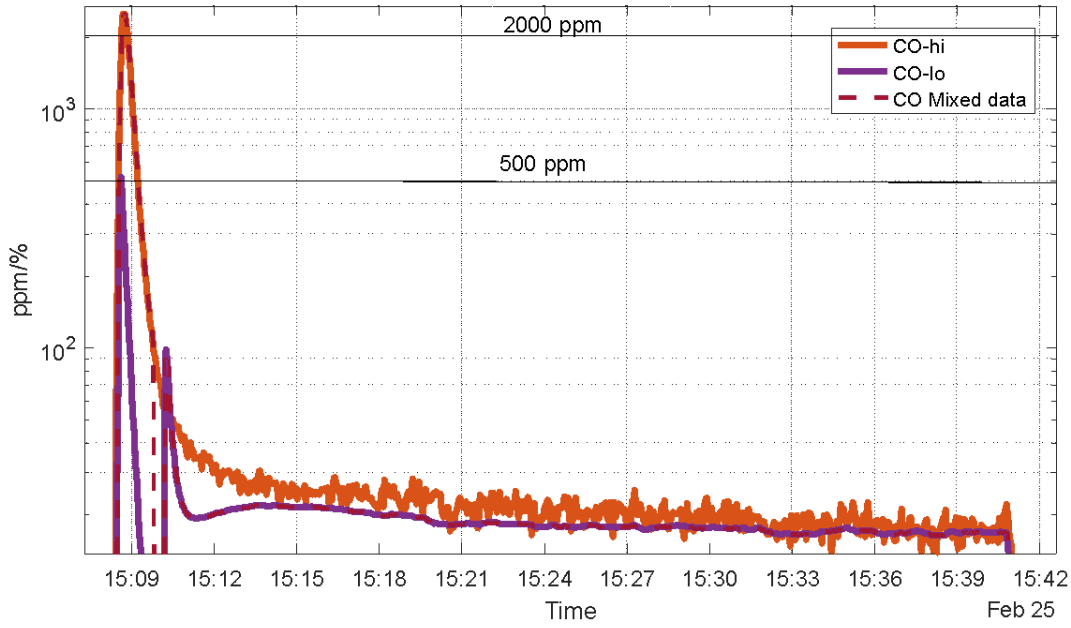

Figure 8.2 – Carbon monoxide measurement during a start-up transient of a gas turbine – BH test rig in Massa (MS)

Using the presented protection system, it is possible to keep the response time of the gas sensors, also after the exposition to extreme concentrations, not larger than 1 minute as required from the application constrains.

8.2 Commercial analyser comparative test

The analyser was tested for more than six months in a BH test plant in Massa (Italy), to analyse the exhaust gases of gas turbines. The facility, where the tests were carried out, is used to test brand new gas turbines before they are delivered to the customer.

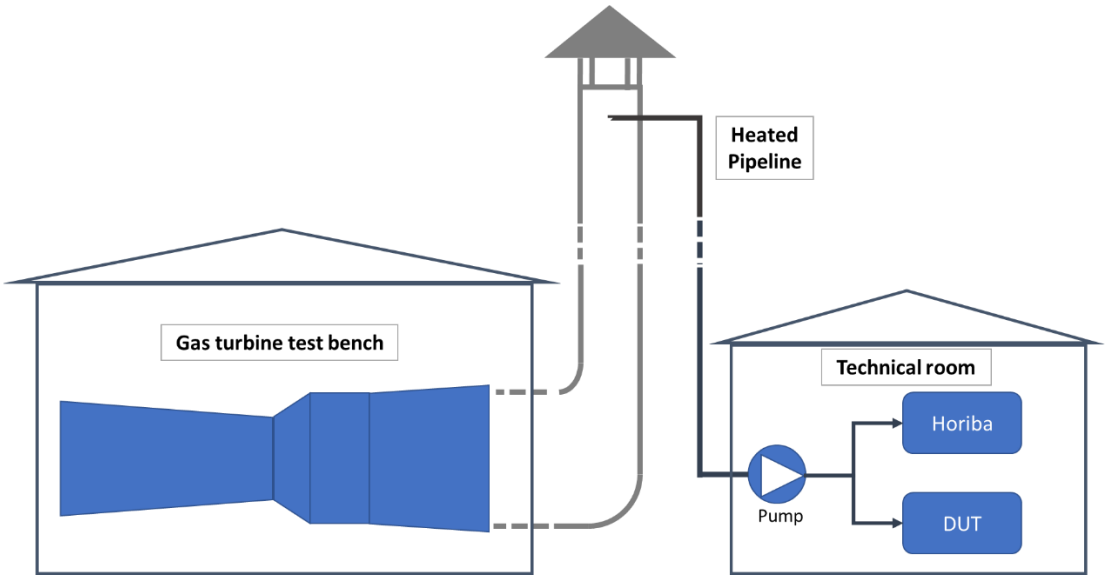

Figure 8.3 – Scheme of the test setup in the BH plant in Massa. DUT is the developed instrument, Horiba is a commercial gas analyser.

In Figure 8.3 a scheme of the test setup is shown: the analyser (Device Under Test, DUT) works in parallel with a commercial gas analyser commonly used to measure the exhaust gas composition (*Horiba PG-350)*. The *Horiba PG-350* analyser exploits infrared optical sensors for CO, chemiluminescence sensors for NOx and paramagnetic sensors for oxygen measurements, respectively. The *Horiba* instrument is one of the most accurate (and expensive) gas analysers on the market; its main specifications are shown in Table 6.

Target Gas (Range)	**Linearity**	**Repeatability**	**Drift**
CO (0-50 ppm)	2 ppm	0.25 ppm	0.5 ppm per Day
O_2 (0-25%)	0.5 %	0.125 %	0.5 % per Day
NO_x (0-50 ppm)	2 ppm	0.25 ppm	0.5 ppm per Day

Table 6 – Horiba PG-350 specifications.

The developed analyser was equipped with 6 electrochemical sensors from Alphasense as shown in Table 7, where the main characteristics declared by the producer are also reported.

Target Gas	**Sensor Model**	**Hosting chamber**	**Range (FS)**	**Resolution**	**Drift**	**Linearity**
Carbon Monoxide (*Co_Hi*)	CO-CX	Ch1	0-1500 ppm	1 ppm	6% per year	2 ppm at FS
Carbon Monoxide (*Co_Lo*)	CO-AX	Ch2	0-150 ppm	0.5 ppm	6% per year	2 ppm at FS
Carbon Monoxide (*Co_Lo*)[16]	CO-A4	Ch2	0-50 ppm	0.1 ppm	6% per year	1 ppm at FS
Oxygen	O2-A1	Ch1	0-25 %	0.1%	1% per 3 months	2 % at FS
Nitrogen Dioxide	NO2-A43F	Ch2	0-20 ppm	0.1 ppm	6% per year	5 ppm at FS
Nitric Oxide	NO-A1	Ch1	0-150 ppm	0.2 ppm	6% per year	2 ppm at FS

[16] Different CO sensors were tested to evaluate the performance and the calibration stability over time. The *Alphasense* CO-A4 is a 4-electrodes sensor for environmental measurements of carbon monoxide. It is characterized by a limited measurement range and by a very high accuracy, which makes it a good candidate for chamber #2. Unfortunately, hydrogen, which can be present in traces in the exhaust gases, is a strong interferent for this sensor (50% of CO sensitivity). Therefore, after these tests, the Alphasense CO-CX and CO-AX sensors, designed to have a limited cross-sensitivity to $H_{2,}$ were used.

Table 7 – Electrochemical sensor set used in the developed instrument.

The six-month measurement campaign gave satisfactory results, confirming that the developed instrument is, a valid, portable, economical, reliable and extremely flexible alternative to commercial instruments such as the Horiba, in applications where continuous monitoring of the exhaust gases is required but which do not require certification of the emission level.

The principal aspect to be evaluated was the performance of the instrument during high gas concentration transients and the calibration stability over time, keeping into account that the commercial analyser was calibrated before each test, whereas the DUT was calibrated only at the beginning of the test campaign (looking at Table 6, the most critical aspect of the commercial gas analyser is the relevant measurement drift, which forces to perform the instrument calibrations before each test).

In Figure 8.4 and Figure 8.5 the comparison of the developed instrument (DUT) with the Horiba PG-350 measurements during typical gas turbine tests is reported. The data reported in Figure 8.4 and Figure 8.5 are representative of the behaviour of the two analysers during the whole measurement campaign. It must be observed that different machine operating regimes cause large variations of the target gas concentrations. The maximum errors of the DUT sensors (considering the Horiba measurements as "real values") are consistent with the expected values, taking into account that the main difference between the Horiba sensors and the electrochemical sensors is the response time. In detail, considering the CO sensors, the electrochemical sensors are slower (the error increases during the fast concentration variations) with respect to the optical sensors, but they are sufficiently fast and accurate to evaluate the target gases concentrations in steady state working conditions, which are the most significant phases of the test. The opposite situation holds for oxygen sensors in terms of response time, but the conclusions are the same as for the CO sensors in terms of capability of detecting the target gas concentration, whereas a similar behaviour can be observed for the NOx sensors.

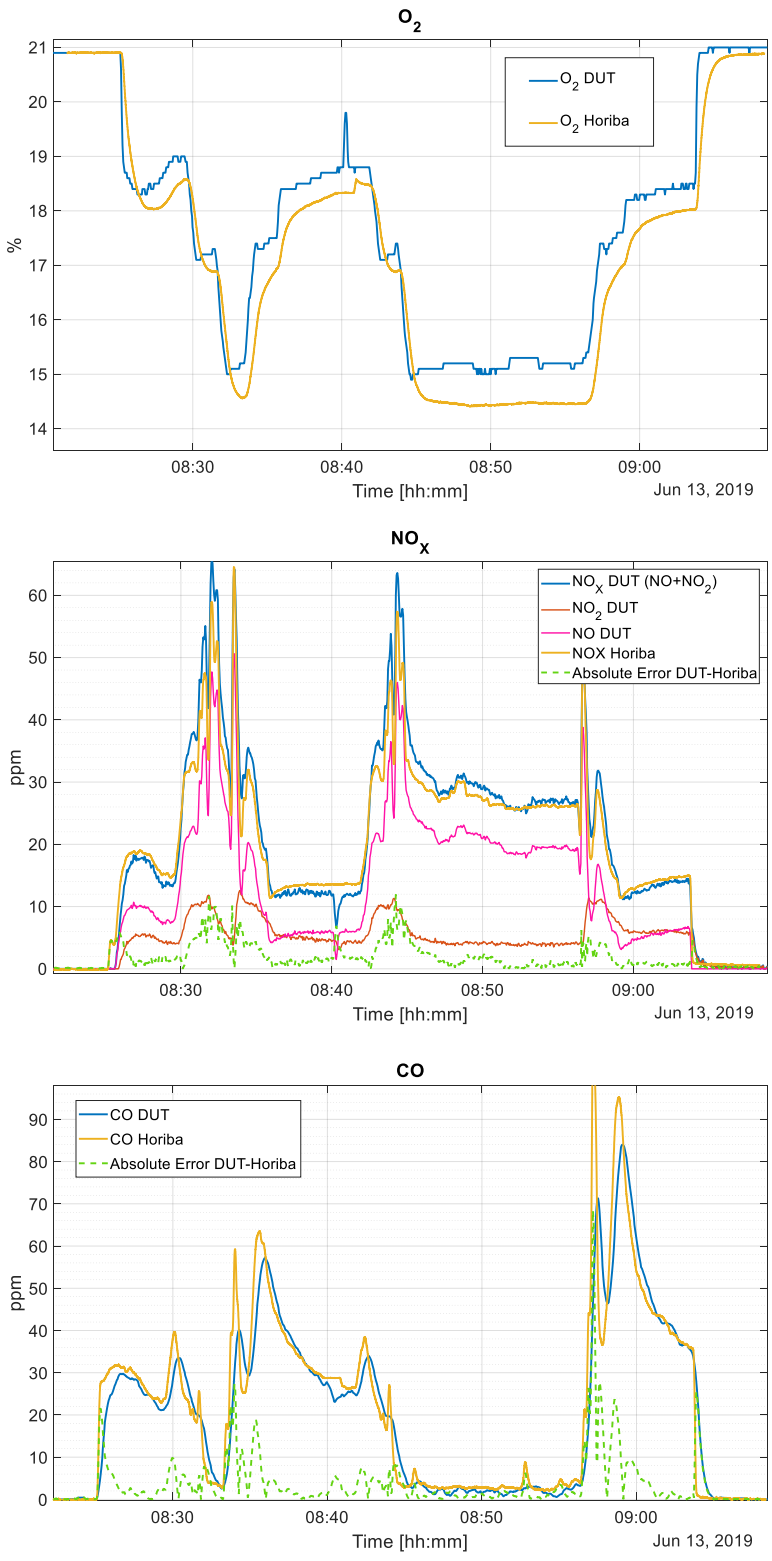

Figure 8.4 – DUT and Horiba measurement comparison during a gas turbine test. (June)

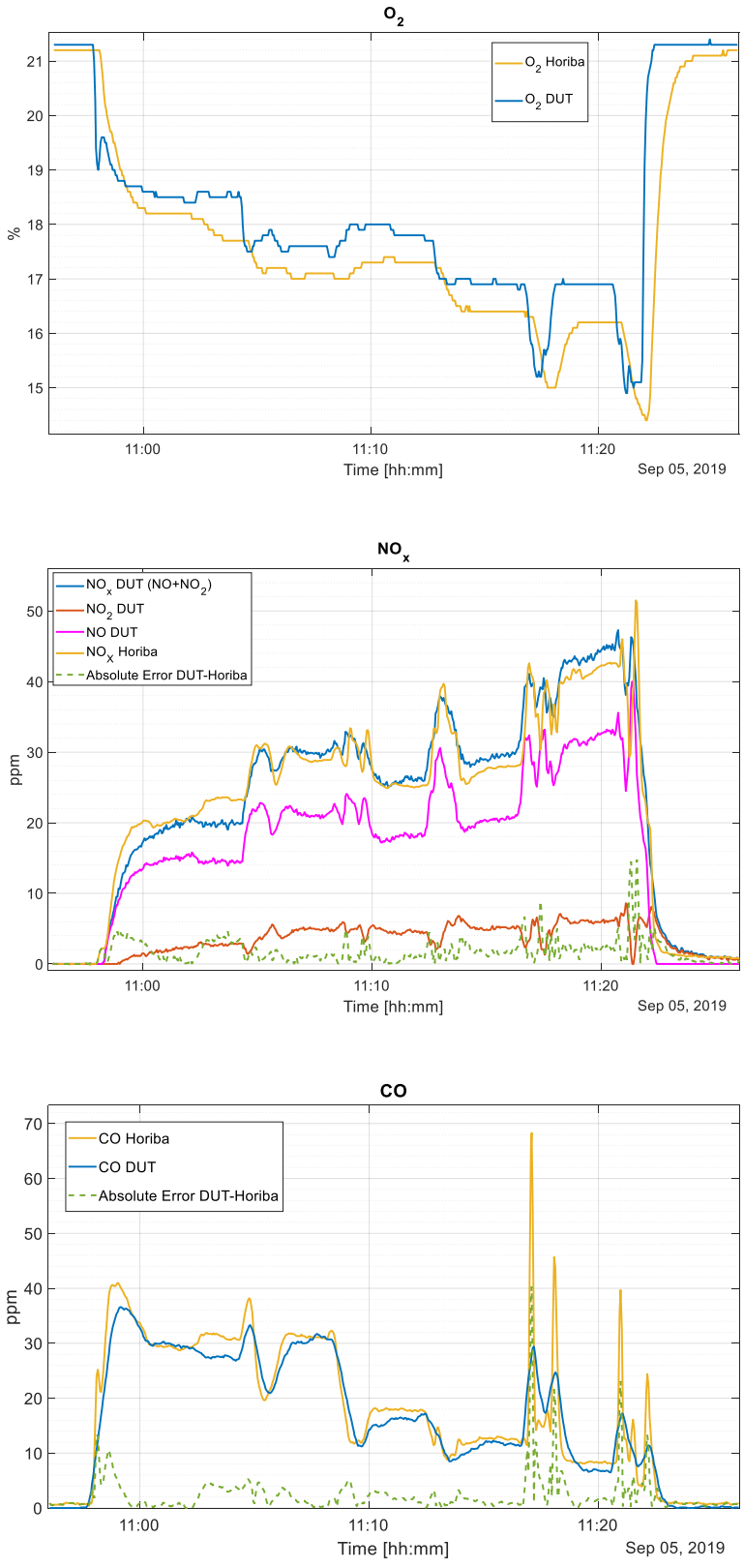

Figure 8.5 – DUT and Horiba measurement comparison during a gas turbine test. (September)

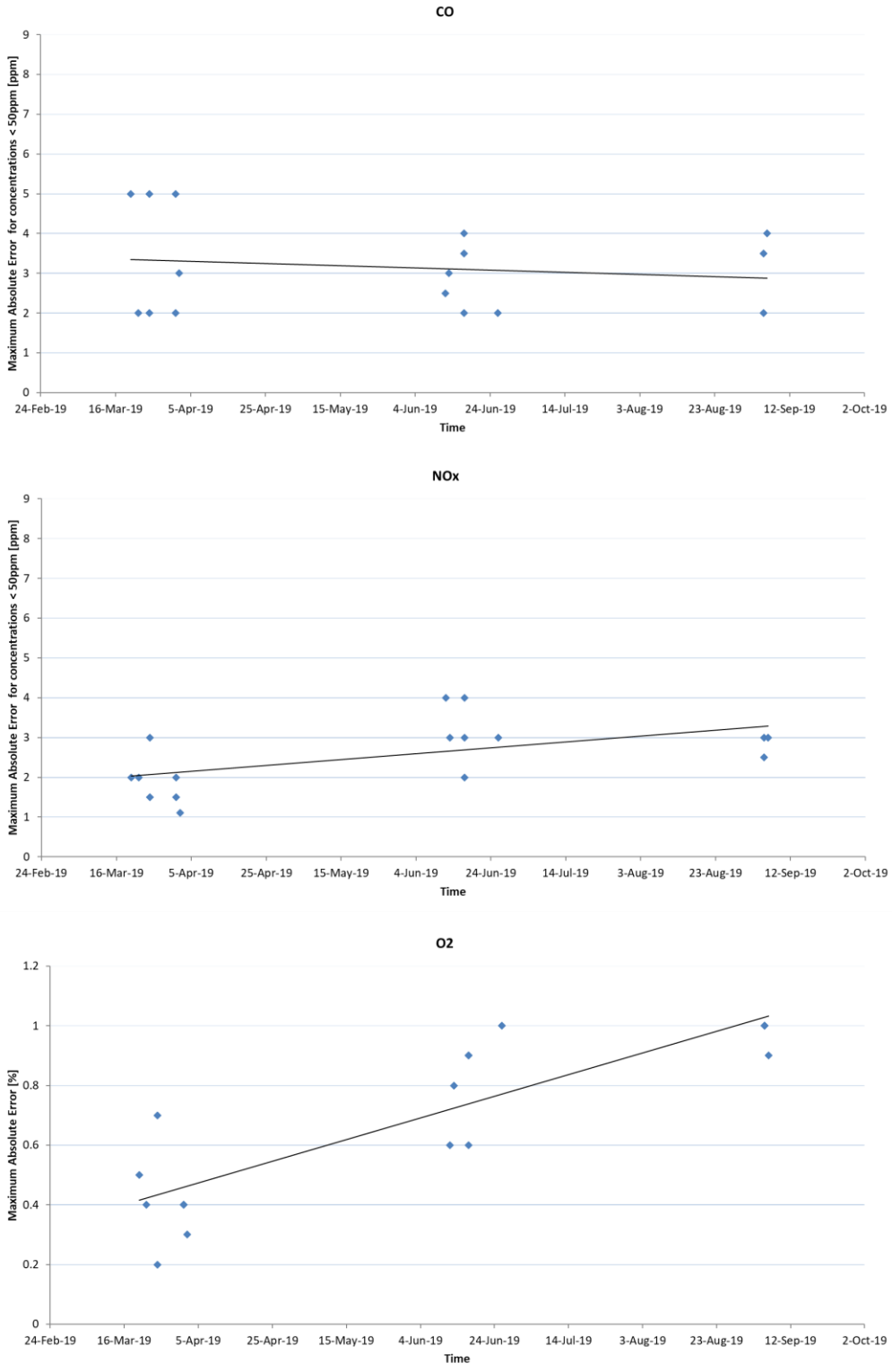

Figure 8.6 – Sensors drift over time.

In Figure 8.6 the maximum errors that affect the DUT measurements of the CO, NOx ($NO+NO_2$) and O_2 sensors are shown. For CO and NOx, concentrations lower than 50 ppm were considered, that is the range more relevant for combustion monitoring and where the accuracy of the Horiba is better. The time interval considered is six months. During this period, as already highlighted, the electrochemical sensors were not replaced or calibrated. The markers in the graphs represent the maximum errors evaluated during each performed test of a gas turbine. As it can be seen, the oxygen sensor exhibits the larger drift over time, whereas the CO and NOx sensor drifts are more limited. In any case, the sensor drift is much lower than Horiba declared drift. This test, as anticipated in the general discussion, confirms the main advantage of the electrochemical sensors with respect to the sensors exploited by the Horiba analyser, that is the possibility of not recalibrating the sensors often. Considering these results, a calibration check of the electrochemical sensors every 2 to 3 months should be sufficient for the application. The main disadvantages of electrochemical sensors, on the other hand, consist in general in the slower response time and measurement accuracy. An improvement of the measurement accuracy can be obtained controlling/monitoring the temperature of the sensors, since the environmental temperature variations cause slight sensitivity changes. As an example, in Figure 8.7 the O2-A1 sensor sensitivity dependence on the operating temperature is shown. Correction of this problem can also be done using the built-in temperature sensor on the sensor modules, but this would require a more complex calibration procedure.

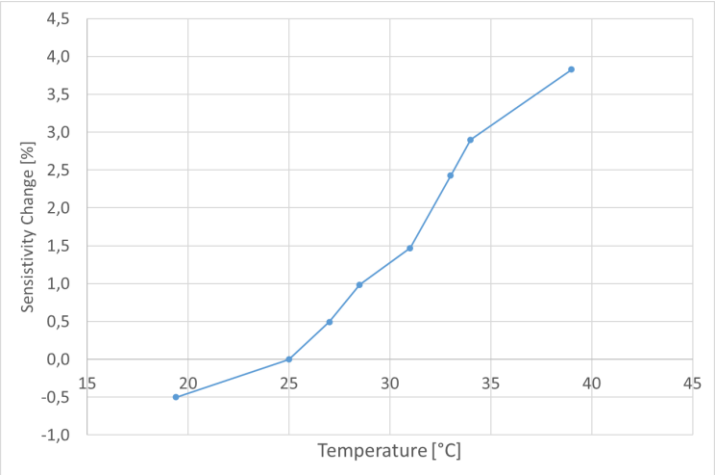

Figure 8.7 - Oxygen sensor sensitivity variation with temperature.

8.3 Gas analyser final considerations

A comparison of the developed analyser with the commercial reference instrument have been reported in the previous section. It is important to remark that the developed instrument prototype is not an alternative product to the commercial reference instrument, but it responds to different needs as reported in section 7. The main challenging part in the development of the analyser was the design of a system architecture that allows the use of low-cost sensors for the continuous monitoring of industrial exhaust gases, respecting the minimum specifications required by BH.

One of the main requirements from BH service engineers was concerning the calibration procedure. The commercial reference analyser requires references gas tanks to calibrate the instrument on the site after the transportation. This aspect introduces relevant additional costs and management issues since calibration tanks are difficult to be supplied and delivered. The designed instrument layout, thanks to the modular structure (each sensor can be individually calibrated in laboratory and delivered on the site) and the selection of electrochemical sensors (the calibration is long term held) solved this problem.

This application also required the design of custom components, such as the chiller, that was not commercially available. The setup and the tests on this instrument, even if it does not include a strong innovative component, was very complex and it required a big effort.

The problem of avoiding exposure to too high concentrations of target gases, which can cause sensor poisoning and long recovery times, has been solved at the system level by adopting the double cascade measurement chamber structure, which as far as we know is an original solution.

9 Conclusions

In this work, two different measurements systems for the combustion monitoring/control of gas turbine burners were developed, characterized, and tested. The measured quantities are the concentrations of the different compounds in the burner exhaust gases and the ion density in the burner combustion chamber. For the ion density sensor, a theoretical model was also developed, which was essential for the experimental data interpretation.

The exhaust gases composition measurement is a well established technique for checking whether the combustion process deviates from nominal behaviour. Exhaust gas analysers are usually very expensive devices and most of them are not transportable. Moreover, accurate gas analysers require frequent calibration exploiting reference gas tanks that, in particular the field of oil and gas, can create transport problems on the industrial site. The exhaust gas analyser developed in this works aims to find a trade-off between measurement accuracy, cost of the instrument, and calibration time-intervals. The selection of electrochemical gas sensors adopted in this work, in place of the kinds of sensors commonly used in the analysers on the market (optical, chemiluminescence based and paramagnetic based sensors) allows, with a lower but acceptable accuracy, to significantly reduce the cost of the instrument. Moreover, the instrument based on electrochemical sensors allows to significantly increase the calibration time intervals and, thanks to its modular structure, to exploit pre-calibrated sensors with the calibration data stored in the sensor front-end electronics. The main drawback in the use of electrochemical sensors lies in the risk of sensor poisoning, which implies long sensor recovery times, in case of exposition to high concentration of the target gases. In the developed instrument this risk is avoided exploiting a two measurement chamber structure and a set of pumps and valves, which allow to divert the exhaust gas flow in case of dangerous conditions from the most critical sensors.

The developed ion current measurement instrument exploits as ion sensor the spark plug always present in the burner. The ion current is proportional to the ion density generated by the flame, which is strictly related the air to fuel ratio of the combustible mixture and to the combustion product concentrations (DC component), and to the presence of flame instabilities (AC

component), which may damage the burner structure or cause flame extinguishing. The main advantage of ion current measurements is the fast response time, which could allow a real time feedback control of the burner. A further characteristic of this kind of measurement is the non-invasiveness of the sensors: in most cases the spark plugs present in the burner can be used.

In Figure 9.1, it is reported a possible integration of the ion current and the exhaust gas composition measurements systems with the closed-loop turbine-burner control system. As already discussed, the composition of the exhaust gases, and in particular their content of CO, is a reliable indicator of the combustion efficiency, but this information is available with a delay of at least tens of seconds due to the gas sampling and conditioning system, and due to the response time of the gas sensors.

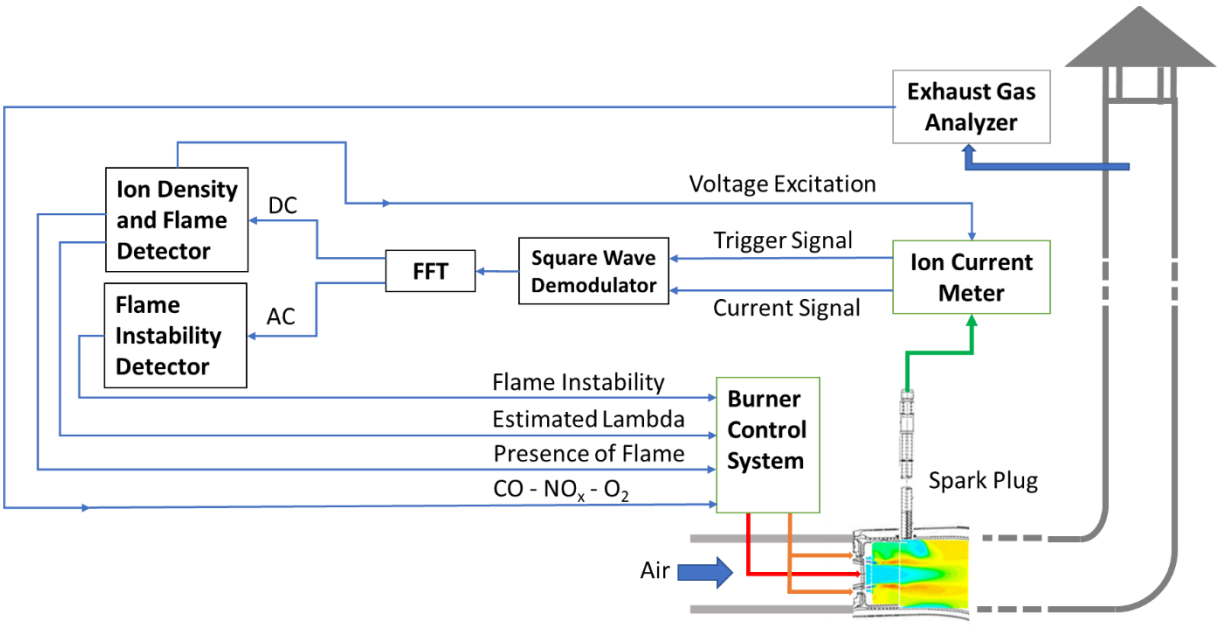

Figure 9.1 – Proposed model for the combustion control measurement integrations.

The ion current measurement is instead very fast, and it allows to monitor the ion density and the presence of flame instabilities in real time, giving timely information of relevant parameter as, e.g., the air to fuel ratio of the combustible mixture. With reference to Figure 9.1, the ion current measurements can be exploited by the burner control system to increase the combustion stability, whereas the measurement of the exhaust gas composition (slow) allows to correct the ion density

setpoint to minimize the presence of CO (index of poor combustion efficiency) and NOx (index of a too high flame temperature). The flame instabilities are more frequent when operating at high air to fuel ratios, a common situation for low NOx burners: a fast and reliable detection of this condition is fundamental to maintain the flame stable avoiding pressure peaks or flame extinctions.

Even if specifically focused on gas turbine burners, this thesis suggests the possibility to implement real-time closed loops controls in almost all the burners present on the market. In particular, the presented exhaust gas measurement instrument can be miniaturized to be installed in building boilers [41] or in whatever type of industrial plant [42] where a combustion process is involved, whereas the ion current measurement can be used also in less extreme applications with respect to those considered in this thesis, as already happens, e.g., for automotive engines.

The ion current measurement, even if it is supported by a solid theoretical background, requires a larger test campaign before becoming an applicable technology, but the preliminary results are very encouraging.

To conclude, a few considerations about the future developments. The two measurement instruments developed allow continuous monitoring, even for long periods, of both the concentration of ions in the combustion chamber and the concentration of the various compounds in the exhaust fumes, laying the foundations for the application of 'machine learning' algorithms for searching correlations among the measured quantities. In particular, the possibility of continuously examining large volumes of data by capturing and identifying subtle and dynamic patterns that would remain obscure with traditional analyses (for example, as highlighted in the context of the thesis, identifying the quantities and the conditions of influence for the generation of CO) constitutes today one of the most challenging and financially supported research fields for the 'Oil and Gas' field, able to pave the way towards the scenario hypothesized since the introduction of the thesis, i.e. the transition from monitoring to combustion control.

References

[1] F. Ahmad, D. S. u. R. Shah and M. S. Siddiqui, "Optimization of an Internal Combustion Engine`s Efficiency for Fuel Conservation & Green Environment," in *International Conference on Energy Systems and Policies (ICESP)*, Islamabad, 2014.

[2] G. Gruber, B. Schweighofer, G. Brasseur and R. Basso, "Ion current measurement for parameter estimation in small two stroke engines," *Proc. IEEE Int. Instrum. Meas. Technol. Conf. (I2MTC),* pp. 1-6, 2018.

[3] Y. LiuLiguang, L. YeZhijun and W. Deng, "Numerical simulation study on correlation between ion current signaland NOXemissions in controlled auto-ignition engine," *Applied Energy,* no. 156, pp. 776-782, 2015.

[4] N. Docquier and S. Candel, "Combustion control and sensors: A review," *Prog. Energy Combustion Sci,* vol. 28, no. 2, pp. 107-150, 2002.

[5] J. Shua, J. Fu, J. Liua, S. Wang, Y. Yin, B. Deng and S. M. Becker, "Influences of excess air coefficient on combustion and emission performance Influences of excess air coefficient on combustion and emission performance dynamics with reduced chemical kinetic model," *Energy Conversion and Management,* no. 187, pp. 283-296, 2019.

[6] W. Zhenhua, H. Junxing and A. Jason, "A review of electrostatic monitoring technology: The state of the art and future research directions," *Progress in Aerospace Sciences,* vol. 94, pp. 1-11, 2017.

[7] M. Asano, T. Kuma, M. Kajitani and M. Takeuchi, "Development of new ion current control combustion control system," in *Paper 98-0162, vol. SP-1356*, Detroit, 1998.

[8] Y. Ohashi, W. Fukui, F. Tanabe and A. Ueda, "The application of ionic current detection system for the combustion limit control," in *SAE 1998 International Congress and Exposition, Electronic Engine Controls: Sensors, Actuators, and Development Tools, Paper 98-0171*, Detroit, 1998.

[9] J. Auzins, H. Johansson and J. Nytomt, "Ion-gap sense in mis-fire detection, knock and engine control," in *SAE 1995 World Congress , Paper 950004*, Detroit, 1995.

[10] N. Rivara, P. Dickinson and A. T. Shenton, "A transient virtual-AFR sensor using the in-cylinder ion current signal.," *Mechanical Systems and Signal Processing,* vol. 23, no. 5, pp. 1672-1682., 2009.

[11] Z. Gao, X. Wu, C. Man, X. Meng and Z. Huang, "The relationship between ion current and temperature at the electrode gap," *Applied Thermal Engineering,* vol. 33, pp. 15-23, 2012.

[12] H. Kubach, A. Velji, U. Spicher and W. Fischer, "Ion current measurement in diesel engines," *SAE Technical Paper,* vol. 1, no. 2922, 2004.

[13] N. Henein, T. Badawy, N. Rai and W. Bryzik, "Ion current, combustion and emission characteristics in an automotive common rail diesel engine," *J. Eng. Gas Turbines Power,* vol. 042801 052802, p. 134, 2012.

[14] Badawy, T, N. Henein and W. Bryzik, "Closed loop control using ion current signal in a diesel engine," *SAE Technical Paper,* pp. 2011-01-2433, 2012.

[15] R. Rao and D. Honnery, "The prediction of torque in a diesel engine using ion currents and artificial neural networks," *Int. J. Engine Res,* vol. 15, no. 3, pp. 370-380, 2014.

[16] S. ZHENG, X. ZHANG and Z. SHEN, "Study on cycle-by-cycle variations of ion current integral and pressure in spark ignition engine," in *Electronic and Mechanical Engineering and Information Technology (EMEIT), 2011 International Conference on. IEEE, 2011. p. 3404-3407.*.

[17] N. Docquier, F. Lacas and S. Candel, "Operating point control of gas turbine combustor," in *AIAA 39th Aerospace Sciences Meeting, Paper 2001-0485,*, Reno, NV, 2001.

[18] G. Dong, Y. Chen, Z. Wu, L. Li and R. Dibble, "Study on the phase relation between ion current signal and combustion phase in an HCCI combustion engine," *Proc. Combustion Inst.,* vol. 35, no. 3, p. 3097–3105, 2015.

[19] S. Keshav, Y. G. Utkin, M. Nishihara, J. W. Rich, I. V. Adamovich and A. Bao, "Studies of chemi-ionization and chemiluminescence in supersonic flows of combustion products," *J. Thermophys. Heat Transf.,* vol. 22, no. 2, pp. 156-157, 2008.

[20] J. Krabicka, G. Lu and Y. Yan, "Profiling and characterization of flame radicals by combining spectroscopic imaging and neural network techniques," *IEEE Trans. Instrum. Meas,* vol. 60, no. 5, p. 1854–1860, 2011.

[21] R. Raymond, S. Andre and M. Fabian, "Local Air-Fuel Ratio Measurements Using the Spark Plug as an Ionization Sensor," vol. 106, no. 1224-1234, 1997.

[22] J. Ballester and T. Garcı´a-Armingol, "Diagnostic techniques for the monitoring and control of practical flames," *Progress in Energy and Combustion Science,* no. 36, p. 375–411, 2010.

[23] T. M. York and H.-B. Tang, Plasmas and Plasma Dynamics, Elsevier, 2015.

[24] T. Addabbo, A. Fort, M. Mugnaini, L. Parri, V. Vignoli, M. Allegorico, M. Ruggiero and S. Cioncolini, "Ion Sensor-Based Measurement Systems:Application to Combustion Monitoring in Gas Turbines," *IEEE Transactions on Instrumentation and Measurement,* vol. 69, no. 4, 2020.

[25] R. J. Kee, M. E. Coltrin, P. Glarborg and H. Zhu, Chemically Reacting Flow: Theory, Modeling, and Simulation, 2nd Edition, Wiley, 2017.

[26] L. Fangyan, X. Lijun, D. Minglong, Y. Lijun and C. Zhang, "Ion current sensing-based lean blowout detection for a pulse combustor," *Combustion and Flame,* vol. 176, pp. 263-271, 2017.

[27] C. Wollgarten, N. Zarzalis, F. Turrini and P. Antonio, "Experimental investigations of ion current in liquid-fuelled gas turbine combustors," *International Journal of Spray and Combustion Dynamics,* vol. 9, pp. 172-185, 2017.

[28] A. Melzer, Physics of Dusty Plasmas, Springer, 2019.

[29] M. S. Benilov, "The Child–Langmuir law and analytical theory of collisionless to collision-dominated," *PLASMA SOURCES SCIENCE AND TECHNOLOGY,* p. Plasma Sources Sci. Technol. 18 (2009) 014005 (14pp), 2018.

[30] T. Addabbo, A. Fort, M. Mugnaini, P. Parri, V. Vignoli, M. Allegorico, M. Ruggiero and S. Cioncolini, "Ion Sensor-Based Measurement Systems:Application to Combustion Monitoring in Gas Turbines," *IEEE TRANSACTIONS ON INSTRUMENTATION AND MEASUREMENT,* vol. 69, no. 4, 2020.

[31] D. Nicolas and S. Candel, "Combustion control and sensors: a review," *Progress in Energy and Combustion Science,* vol. 28, pp. 107-150, 2002.

[32] L. Yintong, Y. LiJunyu and D. WuJun, "Numerical simulation study on correlation between ion current signaland NOXemissions in controlled auto-ignition engine," *Applied Energy,* no. 156, pp. 776-782, 2015.

[33] R. Pavri and G. D. Moore, "Gas Turbine Emissions and Control," GE Energy Services, Atlanta, GA, 2001.

[34] CNR, "Misura delle concentrazioni di specie gassose e particolato in fumi di combustione e flussi reattivi".

[35] J. R. Stetter and J. Li, "Amperometric Gas Sensors, A Review," *Chemical Reviews,* no. 352-366, p. 108, 2007.

[36] M. v. Soestbergen, "Frumkin–Butler–Volmer Theory and Mass Transfer in Electrochemical Cells," *Russian Journal of Electrochemistry,* vol. 48, no. 6, pp. 570-579, 2012.

[37] W.-S. Wang, H.-Y. Huang, S.-C. Chen, K.-C. Ho, C.-Y. Lin, T.-C. Chou, C.-H. Hu, W.-F. Wang, C.-F. Wu and C.-H. Luo, "Real-Time Telemetry System for Amperometric and Potentiometric Electrochemical Sensors," *Sensors (Basel, Switzerland),* vol. 11, pp. 8593-610, 2011.

[38] Alphasense, "Modelling Amperometric Electrochemical Gas Sensors," AAN 111-02.

[39] T. Addabbo, F. Bardi, A. Fort., M. Mugnaini, L.Parri and V. Vignoli, "Multi-sensors exhaust gas emission monitoring system for industrial applications," in *ApplePies 2017: Applications in Electronics Pervading Industry, Environment and Society pp 49-56*, Rome, 2018.

[40] T. Addabbo, F. Bertocci, A. Fort, M. Mugnaini, V. Vignoli, L. Shahin and S. Rocchi, "Versatile measurement system for the characterization of gas sensing materials," in *Instrumentation and Measurement Technology Conference (I2MTC)*, 2013.

[41] A. Fort, E. Landi, M. Mugnaini, L. Parri, A. Pozzebon and V. Vignoli, "A LoRaWAN Carbon Monoxide Measurement System With Low-Power Sensor Triggering for the Monitoring of Domestic and Industrial Boilers," *IEEE Transactions on Instrumentation and Measurement,* vol. 70, no. 5500609, pp. 1-9, 2021.

[42] T. Addabbo, A. Fort, M. Mugnaini, L. Parri, S. Parrino, A. Pozzebon and V. Vignoli, "A low power IoT architecture for the monitoring of chemical emissions," *ACTA-IMEKO,* vol. 8, no. 2, pp. 53-61, 2019.